THE DEGRADATION OF GLIAL SCAR AND ENHANCEMENT OF CHRONIC INTRACORTICAL RECORDING ELECTRODE PERFORMANCE THROUGH THE LOCAL DELIVERY OF DEXAMETHASONE AND CHONDROITINASE

by

Nicolas Alexander Alba

B. S., University of Florida, 2002

M. S., University of Florida, 2005

Submitted to the Graduate Faculty of the

Swanson School of Engineering in partial fulfillment

of the requirements for the degree of

Doctor of Philosophy

University of Pittsburgh

2013

UNIVERSITY OF PITTSBURGH

SWANSON SCHOOL OF ENGINEERING

This dissertation was presented

by

Nicolas Alexander Alba

It was defended on

April 3rd, 2013

and approved by

X. Tracy Cui, PhD, Associate Professor, Department of Bioengineering

Steven R. Little, PhD, Associate Professor, Department of Chemical and Petroleum Engineering

Willi M. Halfter, PhD, Associate Professor, Department of Neurobiology

Carl F. Lagenaur, PhD, Associate Professor, Department of Neurobiology

Douglas J. Weber, PhD, Associate Professor, Department of Bioengineering

Dissertation Director: X. Tracy Cui, PhD, Associate Professor, Department of Bioengineering

THE DEGRADATION OF GLIAL SCAR AND ENHANCEMENT OF CHRONIC INTRACORTICAL RECORDING ELECTRODE PERFORMANCE THROUGH THE LOCAL DELIVERY OF DEXAMETHASONE AND CHONDROITINASE

Nicolas Alexander Alba, PhD

University of Pittsburgh, 2013

The ability of conducting polymers such as poly(3,4-ethylenedioxythiophene) (PEDOT) to store a drug as a dopant and release it following electrical stimulus make them an intriguing coating possibility for intracortical electrodes, along with their ability to reduce electrode impedance. The mechanism allows for the release of an assortment of useful agents, including anti-inflammatory drugs and neuromodulatory chemicals. We evaluated the release capabilities of a multi-walled carbon nanotube (MWCNT)-doped PEDOT coating incorporating the anti-inflammatory steroid dexamethasone *in vitro* using sputtered-gold macroelectrodes, and then applied the coating to half of the electrodes within 16-shank platinum/iridium floating microelectrode arrays for chronic *in vivo* evaluation in rat visual cortex. Impedance measurement, neurophysiological recording, and cyclic voltammetric release stimulus (-0.9 V to 0.6 V, 1 V/s, 20 cycles) was performed daily to all channels. On the 11th day, histology was performed to quantitatively characterize inflammatory tissue response using OX42 (microglia) and GFAP (astroglia). Equivalent circuit analysis was performed to assist the interpretation of impedance data. Our results indicated that the MWCNT/PEDOT-coated gold macroelectrodes released double the amount of dexamethasone using passive release followed by CV stimulation (10 sets of 20 cycles) compared to passive release alone. Coatings applied to Pt/Ir

microelectrodes reduced 1 kHz impedance in PBS by approximately 38%. Coated probes *in vivo* exhibited a significant decrease in 1 kHz impedance for the initial three days of implantation followed by an increase, between days 4 and 7, to values equivalent to those exhibited by uncoated probes. Neurophysiological recording performance of coated and uncoated probes remained equivalent for the duration of the experiment, in terms of signal-to-noise ratio and noise amplitude. Histology revealed no significant difference in tissue inflammatory response to coated and uncoated electrodes. Explant imaging revealed the presence of a membranous film enveloping coated electrodes, and equivalent circuit analysis suggested that the day 4-7 increase in 1 kHz impedance of coated electrodes was due to a decrease in effective surface area of the coatings as well as the core electrodes. Additional work was also performed developing a model for the *in vivo* microinjection of the enzyme Chondroitinase ABC into tissue surrounding implanted microelectrodes.

TABLE OF CONTENTS

LIST OF FIGURES

PREFACE

Many people have provided me with substantial guidance, assistance, and resources during the course of my research, and without their support this dissertation would not have been possible. Chief among them is my graduate advisor Dr. Tracy Cui, to whom I would like to express my sincere and profound gratitude. Tracy has provided constant and generous support and guidance throughout my graduate development in bioengineering, and her advice and critical feedback have played a large role in shaping the researcher I am today. Her contributions and those of the rest of the NTE laboratory, and in particular Dr. TK Kozai, Kasey Catt, and Jeff Du, were an enormous part of what made this work a success, and I am grateful to have had them as colleagues and friends.

I would also like to thank my dissertation committee for their guidance and contributions, each of which having played a critical role in the completion of this dissertation. Dr. Doug Weber and the RNEL laboratory graciously provided the use of their surgical facilities and equipment, as well as valuable advice at all stages of the work. Drs. Carl Lagenaur and Willi Halfter contributed their expertise as well as many critical immunological reagents. Dr. Steven Little provided valuable advice and guidance. I would like to thank each member as well as Dr. Cui for their time and patience as well as their excellent feedback and critiques.

I would like to thank Dr. Justin Sanchez, who first ushered me into the field of brain/machine interface and provided me with my first experiences in a research laboratory. The faculty and members of the Center for the Neural Basis of Cognition have provided extensive support for me and my work, for which I am very grateful. The UPMC Center for Biological Imaging provided much technical assistance and expertise, as did Xia Li, Erika Rost, and Danielle Carns. Dr. Xiliang Luo performed much of the pioneering work into the coating methodologies employed within this dissertation, and I would like to thank him for his guidance and assistance.

I could not have done any of this without the support and encouragement of my friends and family, and I owe you all an enormous debt. To my parents, you have given me so much and asked for so little in return. Your support and love have been my foundation throughout my life and career, and I have not expressed my appreciation nearly often enough. Thank you.

1.0 INTRODUCTION

Cortical neural prostheses (CNPs) are devices which interface directly with the neocortex of the central nervous system in such a way that signal in the form of neural activity may be recorded and interpreted by a computerized algorithm. These devices function through the implantation of penetrating microelectrodes into cortical tissue, providing them with the ability to detect the activity of individual neurons[1]. Such technology holds enormous scientific and clinical potential as it allows for a degree of interaction with fundamental cognitive mechanisms *in vivo* that is unmatched by other recording or imaging methods. A particularly successful application of CNPs has been in the development of thought-controlled assistive devices, which extract motor intent information from the cortex and translate this intent into commands[1–6]. However, the applicability of cortical neural prosthetics within clinical devices is limited by their current effective post-implantation lifetime, defined by a combination of neuron death[7–9], progressive performance degradation[5,10–13], and device malfunction or breakage[14,15]. While select studies have yielded adequate recording performance for well over a year after implantation[16–20], on average these devices perform unreliably in the long term[5,21], limiting their translation to clinical and commercial devices where performance would be expected to persist over decades. The studies summarized in this dissertation demonstrate the use of recently-developed techniques to better understand the physiological factors of cortical neural prosthesis failure and promote the development of novel strategies to improve the reliability of these devices in clinical use.

1.1 NEURAL PROSTHETICS

Cortical neural prostheses are a component of a larger category of implants known as neural prosthetics, which include both recording and stimulating devices intended to interact with a wide variety of neural targets with the purpose of substituting sensory, motor, or cognitive modality that has been damaged due to disease or injury[1]. At this time, the neural prostheses that have shown the most clinical and commercial success have been those that provide electrical stimulation to target tissue, such as deep brain stimulation (DBS) for the treatment of Parkinson's disease[22], or the stimulation of cochlear neurons to partially restore lost hearing[23]. In addition to Parkinson's disease, DBS has seen successful application in the treatment of a wide variety of pathologies, including chronic pain, epilepsy, dystonia, and essential tremor, with over 80,000 device recipients since 1997 according to Medtronic, Inc[24]. Cochlear implants have seen even more widespread adoption, with 219,000 recipients worldwide as of 2010 according to the National Institute of Health[25]. A more recently developed neural prosthetic is the retinal implant, which is typically inserted against the inner surface of the retina and provides controlled stimulation to ganglion cells using a flat multi-electrode array. These devices have seen extensive successful clinical testing, with the first commercial example, the ARGUS II (Second Sight Medical Products, Inc.), being approved by the US FDA for sale in February 2013.

Neural prosthetics intended to record cortical activity come in a variety of embodiments that each feature differing degrees of size, resolution, and surgical invasiveness. The least invasive are those prostheses which employ electroencephalography (EEG), or a network of large electrodes applied directly to the scalp surface that record cortical activity through the skin and skull (Fig. 1.1a). While these devices do not typically possess anywhere near the spatial or temporal resolution of more invasive approaches, their safety and ease of use make them an attractive option for some applications, such as systems that allow patients to communicate by mentally spelling words on a screen[26] or controlling a cursor in 2D or 3D space[27–30]. Electrocorticography (ECoG) is a significantly more invasive technique that involves the chronic implantation of a flexible array of electrodes under the skull and above the brain surface (Fig. 1.1b). ECoG techniques have been developed allowing patients to spell words on a screen[31,32] and voluntarily control seizures[31], and may be used to decode upper limb movements[33].

The focus of this dissertation is on penetrating microelectrodes (Fig. 1.1c), which while being the most surgically invasive of the chronic interface varieties also possess the greatest spatial and temporal resolution, being capable of recording and characterizing the activity of individual neurons within cortex or spinal cord[1,5,16,34]. Perhaps the most prominent clinical goal of such devices is the development of motor control systems for limb prostheses or communication interfaces[3–6,35], through the decoding of recorded cortical activity into representations of desired movement. Such technology has the potential to benefit individuals suffering from movement or communication deficits caused by spinal trauma-induced paralysis (over 1.2m in the US in 2009[36]) and a variety of conditions including stroke, cerebral palsy, amyotrophic lateral sclerosis, multiple sclerosis, and limb amputation[1–3,5,6]. However, for such a device to be considered acceptable for clinical use, it must retain the ability to reliably and reproducibly record large populations of neurons for several decades, and ideally the duration of a human lifetime[3,12,17,21]. Existing CNPs are incapable of providing this level of reliability, with unacceptable degrees of variability in yield of recorded neurons being observed between subjects and individual electrodes[5,10,11,13,37–39]. This chronic variability in recording performance is thought to be in a large part due to the tissue inflammatory response that inevitably occurs around each implanted probe due to implantation trauma and foreign body tissue response[5,7,13,39–

[42]. Due to these challenges, the usage of CNPs has been restricted to research settings, and they have only rarely seen application within human patients.

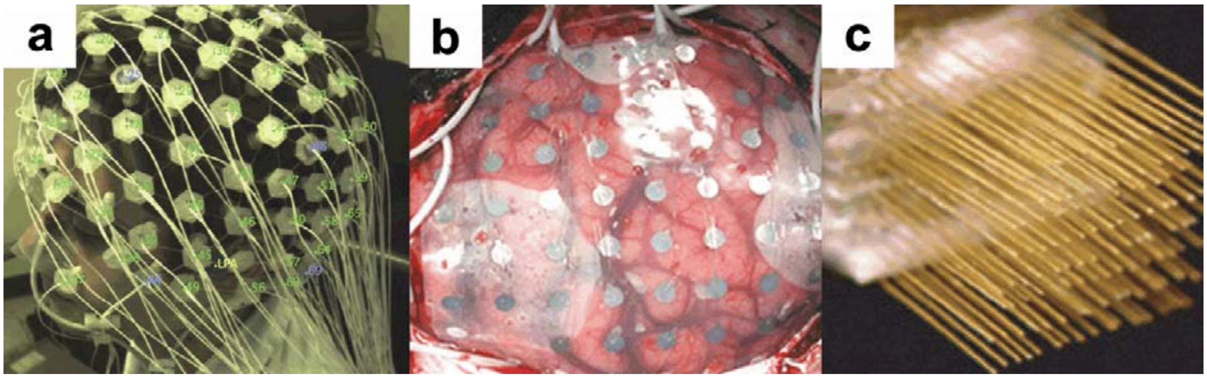

Figure 1.1: Examples of neural interface devices. a) EEG head-net (From Russell et al.[43] © Elsevier. Reprinted with permission). b) ECoG electrodes on brain surface (From Schalk et al.[44] ©2011 IEEE. Reprinted with permission). c) Intracortical microwire array. (From Nicolelis et al.[16] ©2003 National Academy of Sciences, USA. Reprinted with permission).

1.1.1 Historical Overview

The ability to chronically record the activity of neurons within the brain of a living animal requires the consideration of a number of key issues, including the extremely small size of the neurons in question as well as the constant motion of the tissue[45]. Prior to 1950, existing techniques could not be used as they required fine control and direct contact with the neurons being recorded. However, in 1958, Strumwasser published a method that allowed recording to be performed using electrodes in the vicinity of but not physically touching targeted neurons, which he used to perform long-term recording from the brains of anesthetized hibernating ground squirrels using 80 µm insulated stainless steel microelectrodes[46]. This method allowed him to record the activity of individual neurons for periods of over a week, while previous methods limited single neuron recording time to only a few hours[46].

The first chronic intracortical recording implants consisted of arrays of fine insulated stainless steel, tungsten, or platinum/iridium wires either cut or etched to reveal a recording surface at the tip[47–49]. Insulators used for these initial electrodes typically consisted of crudely-applied enamel, lacquer, or solder-glass. These initial fabrication methods commonly resulted in a large degree of variability between electrode tips, though these problems were later addressed by improved fabrication techniques and insulation methods[50–52]. Electrodes of this type were initially implanted individually, and were found to be capable of recording from single neurons[53,54]. This type of implant (Fig. 1.2a) has often been considered the de facto gold standard for chronic recording due to its low cost, ease of fabrication, and long history of use.

In 1970, Wise et al. took advantage of integrated-circuit fabrication techniques to introduce a completely different type of electrode incorporating a gold microwire embedded within a photoengraved silicon substrate[55]. These electrodes provide an interesting alternative to microwires, as the ease and flexibility of the photoengraving process allows for the production of a wide variety of embodiments and geometries, including the ability to localize multiple independent recording surfaces on the same shank at different depths[15,45,56,57]. This technology formed the basis of a commonly used intracortical electrode variety often known as the "Michigan" probe due to the institution of its development[58] (Fig. 1.2b).

A third type of commonly used intracortical recording implant is the silicon microelectrode array (Fig. 1.2c), first described by Jones et al. in 1992[59], and then optimized and characterized in subsequent studies[39,60–62]. This type of array is practically similar to the microwire array, only in place of parallel wires it is produced by machining a solid block of silicon into a square cluster of vertical columns, which are then etched into sharp probes. These sharp silicon probes are then coated with layered platinum and titanium/tungsten and then insulated using polyimide, which is removed at the tip to produce the recording surface. These devices were produced with the goal of maximizing the density of electrodes per unit area in as precise and reproducible a manner as possible, and also provide a large degree of customizability with regard to electrode spacing, geometry, and electrical characteristics.

Work performed in this dissertation employed an advanced variety of microwire array known as the *floating* microwire array[63], or FMA (Fig. 1.2d). This type of array features a flexible cable connector, which provides the array with an additional degree of mobility when implanted into cortex and allows it to drift with brain motion, unlike less sophisticated varieties which are adhered directly to the skull. The concept for this design originated with Gualtierotti and Bailey in 1968[63,64], who proposed a "neutral buoyancy" electrode with a flexible lead wire.

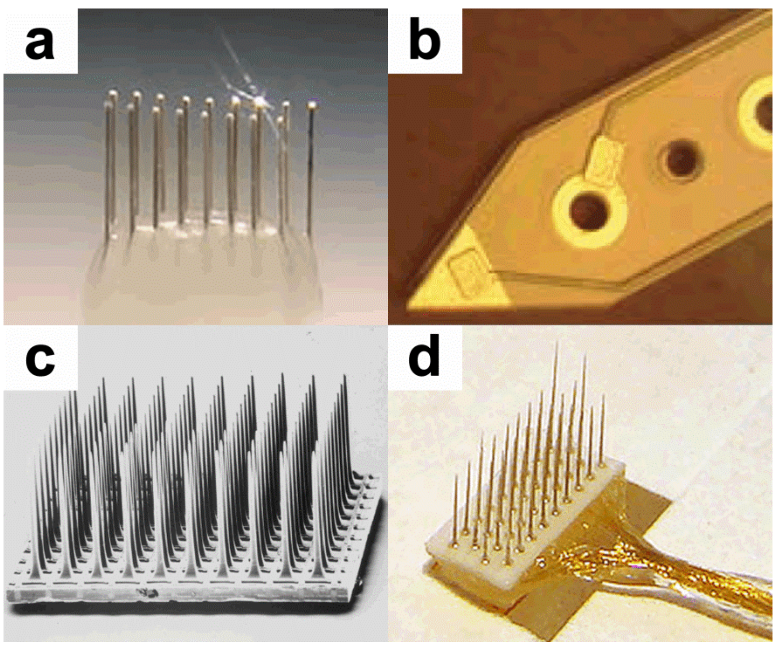

Figure 1.2: Examples of intracortical electrodes. a) Microwire array. b) Planar silicon array, from Kipke et al[12]. c) Silicon multielectrode array, from Rousche and Normann[39]. d) Floating microelectrode array. (a and d © Microprobes for Life Science, Inc. Used with permission. b © Journal of Neuroscience. Reprinted with permission, conveyed through Copyright Clearance Center, Inc. c © Elsevier, Reprinted with permission).

1.1.2 Basic Electrode Theory

An in-depth discussion on the electrochemical behavior of the electrode/electrolyte interface has been published by Merrill et al.[65], and is summarized within this section:

In order to function, electrodes implanted with the intention of stimulating tissue or recording neural activity must transduce the electric current within the lead wire into an ionic current within the surrounding electrolyte (in this case, the extracellular fluid) and vice versa[45]. This transduction of current at the metal/electrolyte interface is fundamentally accomplished through two parallel and competing mechanisms: faradaic current, and capacitive current[65] (Fig. 1.3). Faradaic current occurs whenever an element of charge directly crosses the electrode/electrolyte interface, typically by way of a chemical reaction. These chemical reactions can take many forms, including but not limited to: the disassociation of metal atoms into positively-charged metal cations, the hydrolysis of water into oxygen or hydrogen gas, and the generation of new chemical compounds at the interface such as metal oxide[65].

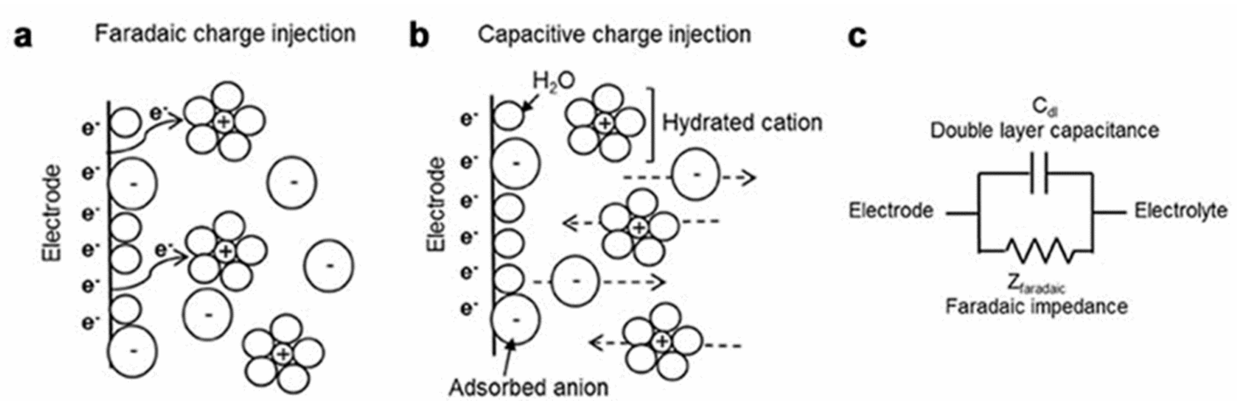

Figure 1.3: Mechanisms of faradaic and capacitive current. a) Faradaic charge injection. b) Capacitive charge injection. c) Equivalent circuit model of the interface, demonstrating parallel capacitive and faradaic current paths (All figures © Bareket-Keren and Hanein[66], Reprinted under CC).

For many types of electrodes, such as silver/silver chloride reference electrodes (where the formation and dissolution of silver chloride occurs readily and reversibly), faradaic current is intended to dominate the transduction process and will not cause any significant damage or chemical change to the electrode surface. However, for other types of electrodes and in certain stimulus conditions, extensive faradaic current will result in electrode corrosion, metal loss, tissue damage, or harmful gas evolution[65]. A number of example cathodic reactions include:

$Cu^{2+} + 2e^- \leftrightarrow Cu$ (metal deposition) (1.1)

$Fe^{3+} + e^- \leftrightarrow Fe^{2+}$ (electron transfer) (1.2)

$2H_2O + 2e^- \rightarrow H_2\uparrow + 2OH^-$ (reduction of water) (1.3)

$IrO + 2H^+ + 2e^- \leftrightarrow Ir + H_2O$ (oxide reduction) (1.4)

$Pt + H^+ + e^- \leftrightarrow Pt\text{-}H$ (hydrogen plating ‘pseudocapacitance’) (1.5)

$AgCl \leftrightarrow Ag^+ + Cl^-$ (dissolution of silver chloride) (1.6)

Example anodic reactions include:

$Fe \rightarrow Fe^{2+} + 2e^-$ (metal anodic dissolution) (1.7)

$2Ag + 2OH^- \leftrightarrow Ag_2O + H_2O + 2e^-$ (oxide formation) (1.8)

$2Cl^- \rightarrow Cl_2\uparrow + 2e^-$ (gas evolution) (1.9)

$2H_2O \rightarrow O_2\uparrow + 4H^+ + 4e^-$ (oxidation of water) (1.10)

$Pt + 4Cl^- \rightarrow [PtCl_4]^{2-} + 2e^-$ (platinum corrosion) (1.11)

Note that these reduction and oxidation reactions will only occur when it is thermodynamically and kinetically favorable for them to do so, and often require specific pH conditions, interfacial potentials, and reactant concentrations for them to proceed at an appreciable rate. Also, note that many of these reactions are potentially *reversible*, as reactive species may remain bound or close to the interface surface, though the reverse reactions may be only favorable outside of the normal operating conditions of the electrode. Representative *irreversible* reactions are also provided, such as the hydrolysis reactions which produce evolved gas. These reactions are considered particularly undesirable within the context of intracortical electrodes, as they can result in undesired local pH changes, gas bubbles, or harmful chemical species[65].

Capacitive current is generated from electrostatic repulsive and attractive forces acting between ions and electric charges building up on either surface of the electrode/electrolyte interface, resulting in a redistribution of charged species within the electrolyte. This redistribution of charge results in a phenomenon referred to as the *electrical double layer* (Fig. 1.4), or the stacking of negative and positive charged species at the interface[65]. These charged species are further separated by layers of polar molecules such as water which preferentially orient themselves at the interface surface, as well as by adsorbed species such as halide anions. In the absence of faradaic current mechanisms the interface may be electrically modeled as a simple capacitor, typically referred to as the double layer capacitor C_{DL}, and has a degree of frequency response defined by the time constant of this capacitor, which represents the saturation

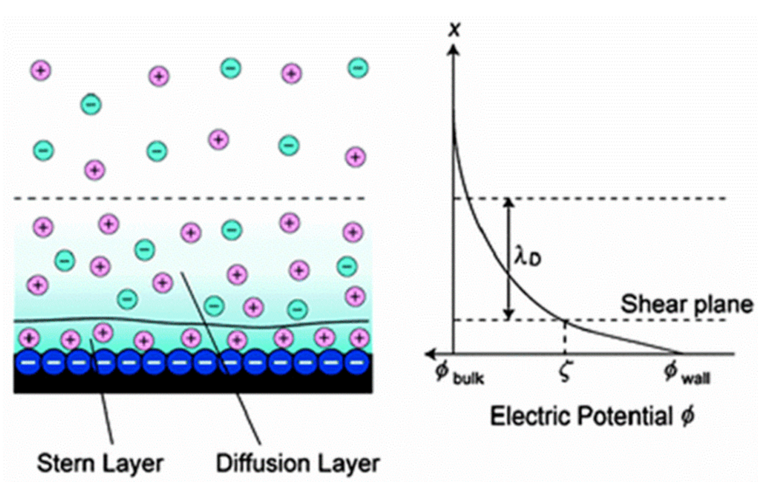

Figure 1.4: The electrical double layer. Schematic and associated potential profile normal to the electrode surface (Figure by Daiguji[67], © 2004 American Chemical Society. Reprinted with permission).

of charged species at the interface surface. As capacitive current is generated purely through the reorganization of charge carriers within the electrode and electrolyte and does not involve any chemical change to the interface, the transduction process will not harm or degrade the electrode surface. However, this mechanism is subject to limitations, as it can only conduct up to a limited charge density and is also dependent on the rate of potential change[65].

Current moving from the electrode to the electrolyte or vice versa is subjected to a change in electrical potential at the electrode/electrolyte interface, within a very narrow interphase region[65]. This change in potential produces an electric field at the interface, measured in V/m. At equilibrium conditions and in the absence of current, this interfacial potential is known as a *half-cell potential*, and is a representation of the thermodynamic driving force for principal species at the electrode interface to undergo oxidation or reduction; typically, the dissolution of the electrode metal into electrolyte through oxidation at the anode, or the deposition of metal by way of the reduction of ionic species at the cathode. At standard state (1 atm, 25° C, 1 mol dm^{-3} solute concentration), this potential is known as the standard electrode potential, though the effective half-cell potential of an interface at non-standard conditions can be calculated from the standard electrode potential using the Nernst equation[65]:

$$E_{eq} = E^{\Theta} + \left(\frac{RT}{nF}\right) \ln \left\{\frac{[\mathrm{O}]}{[\mathrm{R}]}\right\} \tag{1.12}$$

where E_{eq} is the equilibrium half-cell potential, E^{Θ} is the standard electrode potential, R is the gas constant, T is the absolute temperature, F is Faraday's constant, and [O] and [R] are electrolyte concentrations of oxidized and reduced species, respectively. If current is driven across the interface, the interface potential will be forced away from the equilibrium potential, with the difference being known as the *overpotential*. An electrode with an interface potential forced away from its equilibrium potential is generally referred to as being *polarized*.[65]

Theoretical electrode interfaces are commonly modeled as being either purely capacitive, often called *perfectly polarizing*, or purely faradaic, known as *non-polarizing*. In reality, electrode interfaces present some degree of both capacitive and faradaic character. The degrees of capacitive current and faradaic current transduced across an interface upon connection with a voltage source are dependent on several factors, including charge density, the magnitude of the potential applied and the rate of change of that potential, and the kinetics and mass transport limitations of the reduction/oxidation reactions available at the interface. These factors dictate the resistance to current flow of each mechanism, which in turn determines the proportion of current flow through either capacitive or faradaic pathways. In the case of most intracortical electrodes featuring blocking metals such as platinum and slow faradaic kinetics, current will be principally transduced through capacitance up to some limiting charge density, at which point faradaic mechanisms will transduce the excess. At large potential magnitudes, this faradaic mechanism will often be either the reduction or oxidation of water, due to the lack of mass transport restriction owing to the abundance of water in the electrode environment. As the hydrolysis of water can be very damaging to surrounding tissue, its avoidance is a major aspect of stimulation safety, with stimulation paradigms designed to remain within the "water window", or the range of potentials wherein the hydrolysis of water is thermodynamically unfavorable (typically between -0.6 V to 0.6 V)[65,68].

As the magnitudes of interfacial potential and current expected to be encountered during the normal operation of neural recording electrodes and stimulation electrodes are quite different from each other, the design concerns of each electrode are distinctive[68]. Neural recording electrodes, designed to detect and record the action potentials of nearby neurons, are typically only exposed to overpotentials well under 1 mV and thus remain very close to equilibrium[68].

These electrodes are typically fabricated with the goal of achieving a specific impedance range in order to maximize signal-to-noise ratio (SNR) of recording, with higher impedance electrodes being expected to exhibit lower signal-to-noise ratios[68,69]. Recording electrode impedance is typically modulated through changes to surface area or through coatings such as oxide activation or conducting polymers. In contrast, electrodes designed for neural stimulation are expected to endure much larger current densities at elevated potentials. Thus, an important element of stimulation electrode and stimulus paradigm design is the minimization of harmful faradaic reactions, in particular the hydrolysis of water and the corrosion of metal[65,68]. As stimulation is additionally being applied to neural recording electrodes as well for a growing number of applications, including the drug release mechanism studied in this dissertation, these same safety considerations must be applied.

1.2 REACTIVE TISSUE RESPONSE

Upon implantation of an intracortical recording electrode into the brain of a living subject, a complex multi-faceted inflammatory tissue response is initiated as a consequence[70]. This response evolved as a protective mechanism, allowing the host body to detect and isolate foreign objects and resume homeostasis after injury. However, as a key element of this response is the *encapsulation* of the foreign body with reactive glia and extracellular material, it is thought that the process may play a principal role in the large inconsistency of recording performance observed among chronically implanted neural probes[5,9–11,13,21,37–40,42,68,71–73].

This chronic performance inconsistency is typically characterized as a gradual and highly variable reduction in the number of units observed by each channel over time (a ‘unit’ being common terminology for a set of recorded waveforms sorted together with a certain degree of confidence and thought to represent the firing activity of a single local neuron) (Fig.1.5). The loss of unit activity is coupled with a general reduction in recording quality measures, such as the increase of impedance and decrease of SNR of remaining units[19,21,38,74,75]. These effects are thought to correlate with a number of key tissue inflammatory response mechanisms[7–9,21,38,41,70,73,76], making the attenuation or elimination of these mechanisms a primary goal in electrode development and research.

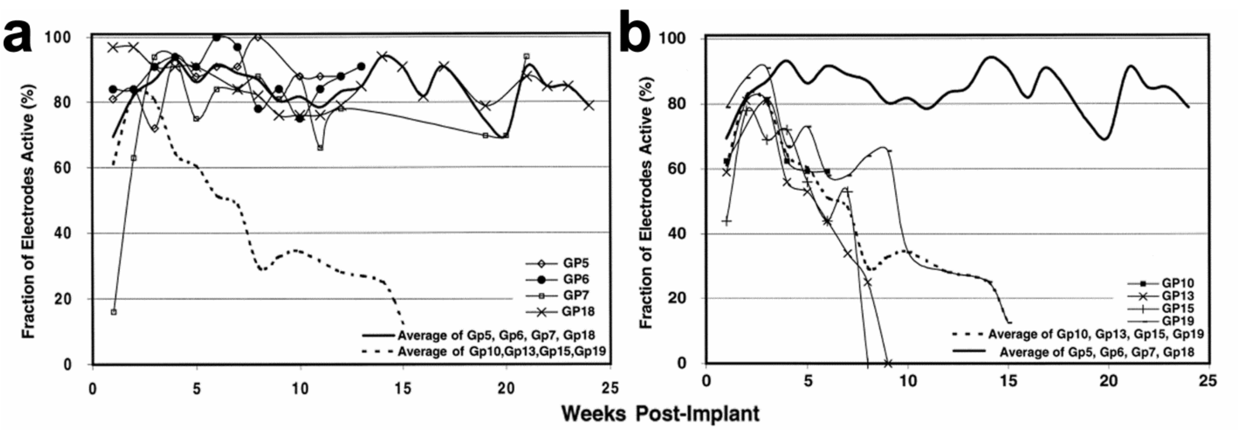

Figure 1.5: Chronic variability and loss of recorded unit activity from implanted neural probes. a) Examples of animals that demonstrated consistent chronic recording performance. b) Examples of animals that demonstrated poor chronic performance. (Figures from Williams et al.[10] © Elsevier. Reprinted with permission).

1.2.1 Overview

Healthy uninjured adult cortical tissue is populated by a variety of cell types, principally various types of neurons and an assortment of glia including astroglia, oligodendrocytes, and microglia (numerical densities being approximately 120,000 neurons/mm^3, 38,000 astroglia/mm^3, 17,000 oligos/mm^3, and 4,000 microglia/mm^3 in adult macaque visual cortex[77]). Astroglia and microglia typically exist in a restive, ramified state in bulk healthy cortex, with astroglia serving a large number of essential roles including blood flow regulation, neuron metabolic support, maintenance of ionic balance, transmitter regulation, and active participation in synaptic function and plasticity[78–80]. Microglia are monocyte-lineage cells that serve a monitoring role, constantly probing cortical tissue for damaged neurons, plaques, and pathological agents using an extensive arborization of processes[73,81–86]. Both cell types are extremely sensitive to disturbances in central nervous system (CNS) homeostasis and readily respond to all forms of tissue insult or disease. The cortex is additionally populated by a number of other cell types including oligodendrocyte precursor cells, stem cells, pericytes, and mast cells[87,88].

When initiated by the insertion of a foreign body such as an intracortical electrode, the tissue inflammatory response within cortex is thought to occur in two distinct yet interrelated phases (Fig. 1.6): the *acute* phase and the *chronic* phase. The acute phase, which persists from the moment of implantation to roughly one to two weeks post-implantation, is characterized by the activation of nearby microglia, astroglia, and other immune cells, coupled with the rapid necrotic or apoptotic death of local neurons, forming a “kill zone”[7,13,89]. This kill zone has been observed to vary in size between 10 and 100 µm from the probe surface, and appears to be dependent on the degree of initial trauma and intensity of the subsequent inflammatory response[7,13,38]. As detectable spikes are typically generated by neuron cell bodies within 50 µm and no more than 130 µm[13,89,90] from the recording surface, this acute neuronal death can theoretically detract from recording performance[13,75]. However, in practice, the acute death of neurons following implantation was not observed to significantly impede recording[7,89]. Regardless, the acute response is thought to be mediated by the initial implantation trauma, vasculature damage, tissue edema, and the adsorption of protein on the implant surface[72,73,91].

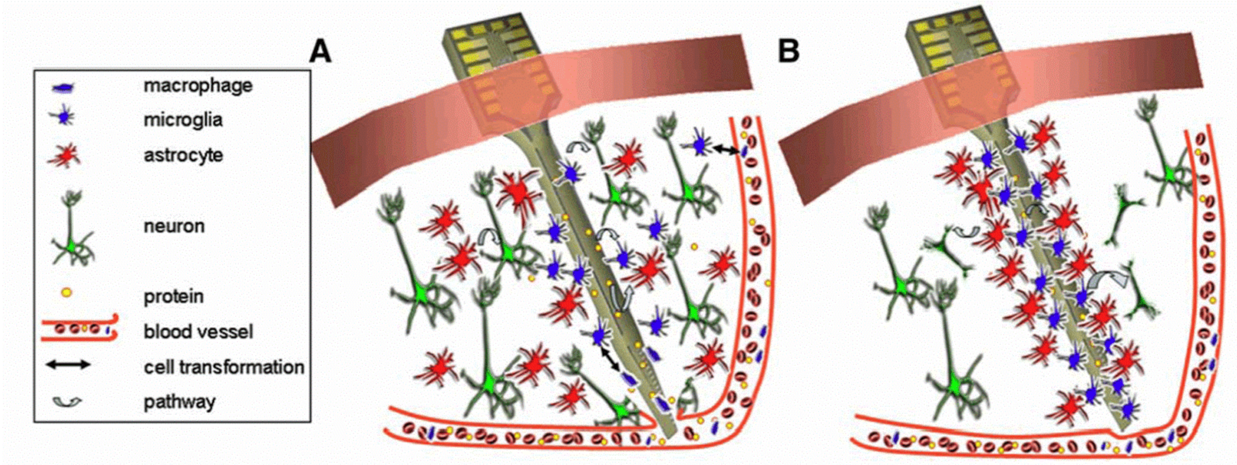

Figure 1.6: Illustration of the phases of reactive cell response. The *acute* phase (A) characterizes tissue response within the initial 1-2 weeks post-implantation, while the *chronic* phase (B) characterizes tissue response at later time points. Note chronic accumulation and compaction of astroglia at the probe interface into an encapsulating glial sheath, as well as reduced neuron density within probe vicinity (Illustration from Schwartz et al.[5] © Elsevier. Reprinted with permission).

The *chronic* phase begins roughly two weeks post-implantation and persists for the duration of implant presence, and is typically characterized by foreign body response leading to the formation and stabilization of a dense astroglial sheath around the tissue/implant interface between two to three weeks post-implantation[7,13,40,41,76,92] (Fig. 1.7), the extent of which has been correlated with increased 1 kHz impedance magnitude[41]. This impedance increase may be a consequence of the increased tortuosity of the encapsulating astroglia, which acts as a barrier to the diffusion of ions through the extracellular space[93]. The chronic phase is also characterized by the progressive degeneration and death of neurons local to the implant[7–9,38].

Further complicating the situation is the fact that the brain is immunologically privileged and shielded from the general immune system by the blood-brain barrier (BBB), which in healthy brain restricts the entry of circulating immunoglobin and lymphocytes in addition to bacteria, serum protein, and many drugs. As a consequence, brain tissue features its own distinctive immune mechanisms that in many ways mirror the inflammatory responses elsewhere in the body, though with different cellular players. Intracortical implants may act as a chronic insult to this barrier through the rupture of nearby vasculature or the migration of meningeal cells or microbes from non-protected areas into cortex by way of the implant shaft[38,72,73,94–96].

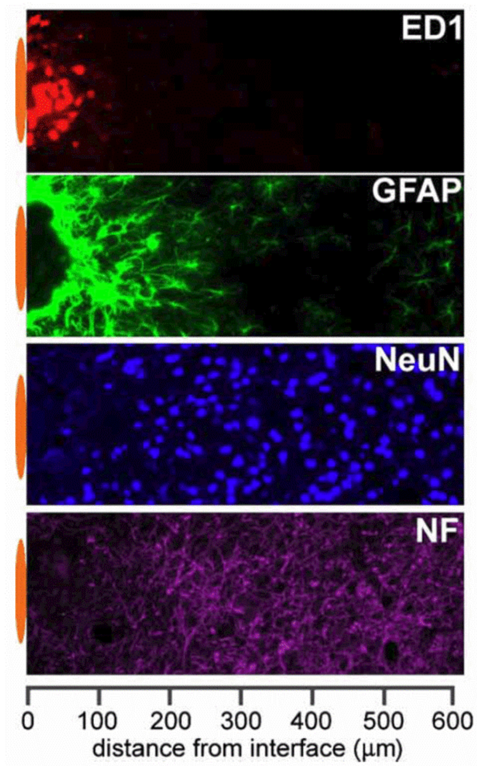

Figure 1.7: Typical astroglial sheath at 4 weeks post-implantation. Note inner core of activated microglia (ED1) surrounded by a dense lamellar astroglial layer (GFAP). Also note reduced density of neuron cell bodies (NeuN) and axons (NF) within 200 μm of probe surface. (Image from Biran et al.[7] © Elsevier. Reprinted with permission).

1.2.2 Implantation Trauma and Provisional Matrix Formation

At the moment of electrode implantation into cortical tissue, a number of key events occur which initiate and modulate the acute inflammatory response, as well as many aspects of the chronic response. Typically, electrodes or electrode arrays are surgically inserted through the pia and into cortex through a craniotomy following the sectioning and retraction of dura. The amount of trauma inflicted during this insertion is dependent on many variables, including insertion speed, location, and probe shape and size[72,91,97–100]. As the probe is driven into tissue it inflicts a host of traumatic events including the lysing of cells and cell processes, the rupture of vasculature both local and up to 300 μm distant from the probe tip[72,91], the long-lasting disturbance of local BBB[101], the tearing of extracellular matrix, and the dragging of meningeal tissue from the pial surface into the cortex[94,96]. However, despite the extensive and multimodal nature of this injury, cortical lesions have been observed to heal to a state nearly homogenous with surrounding healthy tissue after 1-2 months following clean microprobe stabs[7,13,102] with substantially reduced neuronal loss[7–9] if the probe is immediately removed following insertion (Fig. 1.8).

Rupture of local vasculature during probe insertion releases a bloom of plasma exudate into cortical tissue, bypassing the blood-brain barrier[72,73,91]. Among the circulating elements contained within this exudate are erythrocytes and leukocytes, clotting factors, immunoglobin, complement proteins, and an assortment of inflammatory factors and blood proteins[5,13,40,73,92,103]. Many of these cells and factors immediately begin interacting with CNS tissue and the probe surface, and a layer of protein instantly adheres to the probe surface forming a *provisional matrix* in a process commonly known as bio-fouling[38]. This provisional matrix, principally composed of albumin, fibrinogen, complement, fibronectin, vitronectin, and immunoglobin, represents the initiation of the thrombus/blood clot at the interface and is rich with active mitogens, chemoattractants, cytokines, growth factors, and other bioactive agents[103,104]. The provisional matrix in many ways directs the acute inflammatory response and healing process, contributing structural, cellular, and biochemical components, modulating microglial activation, and promoting the recruitment, proliferation, and activation of multiple other cell types[38,73]. The matrix also serves as the principle point of contact by which local cells detect and adhere to the implant surface.[103]

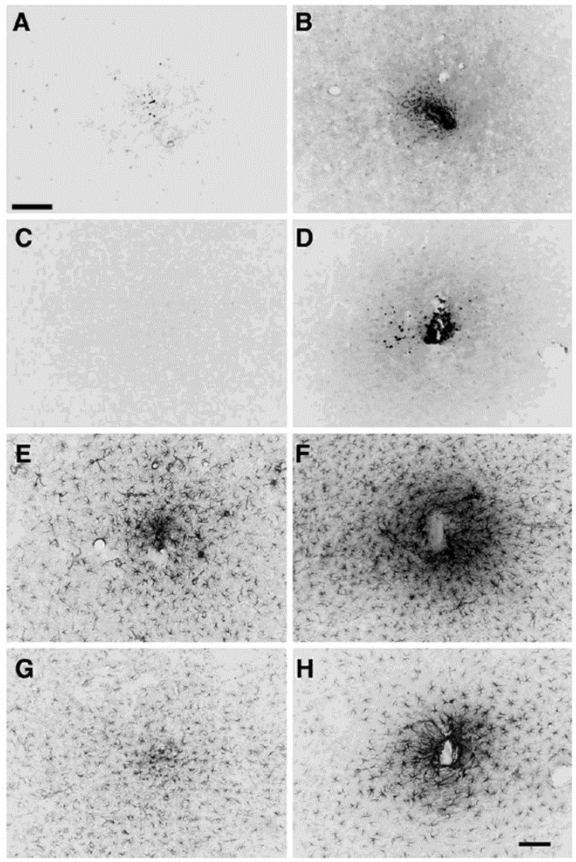

Figure 1.8: Response to stab and implant. Tissue response to stab (ACEG) and chronic electrode implant (BDFH) in rat cortex at 2 (ABEF) and 4 (CDGH) weeks. ABCD are microglia (ED1) and EFGH are astroglia (GFAP). SB = 100 µm (Images from Biran et al.[7] © Elsevier. Reprinted with permission).

1.2.3 Consequences of Vascular Rupture

Despite the rapid clotting of ruptured vasculature post-implantation, the initial introduction of exudate into the lesion area has a number of long-lasting consequences. Mechanically, a principal effect of vascular damage and BBB leakage is the generation of vasogenic brain edema and resulting cytotoxic swelling due to fluid buildup and pressure[13,72]. This edema has been observed to persist for over a week post-implantation and generates a number of abnormal tissue consequences[72]. Ruptured vessels can also lead to loss of perfusion and ischemia downstream of the insult[72,105]. Additionally, vascular rupture not only initiates the inflammatory pathways but also a number of other protein cascades including the extrinsic and intrinsic coagulation systems, the complement system, the fibrinolytic system, the kinin-generating system, and platelet activation[103], which may each play a role in the dynamic adsorption and desorption of protein at the interface. In addition to these various cascades, a number of circulating blood components are known to interact directly with neurons and glia; a prominent example being albumin, the most abundant plasma protein, which has been shown to reversibly increase calcium activity in glia and to also adversely affect neurons and astrocytes[72].

After clotting, a substantial number of residual extravasated erythrocytes remain in the cortical tissue and degenerate through hemolysis, releasing heme into the lesion environment[92]. This heme is subsequently degraded by the heme oxidase enzymes into iron, carbon monoxide, and biliverdin, which is then further converted into bilirubin by biliverdin reductase. This mechanism can cause harm to the local neuron population through both iron-induced oxidative stress as well as the neurotoxic properties of bilirubin. This process is known to play a significant role in tissue outcome following hemorrhagic stroke and traumatic brain injury[88,106] and erythrocyte breakdown products have been observed surrounding probes after six weeks post-implantation[92], though it should also be noted that cortical micro-hemorrhage alone was found to be incapable of causing neural or dendritic degeneration when inflicted by a femtosecond laser pulse[107]. Instead, it may be interpreted that the process is contributing additional stress to the inflammatory environment.

1.2.4 Acute Inflammatory Response

The hallmark of the acute inflammatory response following probe implantation is the activation of an assortment of inflammatory cell types both through the infiltration of leukocytes and through the activation of native glia[73,108]. Elsewhere in the body, the acute response to trauma is dominated by the activity of polymorphonuclear leukocytes[103]: principally neutrophils and to a lesser extent eosinophils and basophils. However, the access of these cells to an injury site in CNS is severely restricted following clotting, due to blood-brain barrier exclusion. Despite this barrier, neutrophils are observed in hematoma and surrounding cortical tissue at the earliest time points following intracerebral hemorrhage[88,109] can damage tissue directly through the release of reactive oxygen species and pro-inflammatory proteases, as well as modulate BBB permeability and potentially aggravate neuron death[88]. Once extravasated into the brain, neutrophils will typically die by apoptosis within two days, though their death can cause further tissue damage as their contents stimulate nearby microglia to secrete toxic factors[88]. Microglia have been observed to phagocytize neutrophils within CNS before autolysis as a defense mechanism, staving off further damage[110].

Microglia serve as the principal actors in the CNS acute inflammatory response and are the first non-neuronal cell type to exhibit a response to implantation trauma, having been observed using two-photon microscopy to react immediately upon probe implantation through the extension of processes toward the probe surface[73]. Within 24 hours, the microglia activate to an amoeboid locomotive state and undergo a number of morphological and functional transformations, including the enlargement of the cell body, thickening of processes, and the upregulation of a number of pro-inflammatory proteins. The microglia become proliferative, migratory, and phagocytotic[73,108,111], rapidly surrounding the implanted probe and consolidating themselves into a thin cellular sheath over the following week[13,40,112]. The role of the activated microglia is multi-fold, and includes the elimination of hematoma and tissue debris as well as the degradation of foreign bodies[13,83,86]. Large foreign bodies are encapsulated through a process called *frustrated phagocytosis* whereupon multiple microglia fuse into multi-nucleated "giant cells" which then envelop the foreign surface[13]. In addition, activated microglia express and release a variety of other potentially toxic factors including cytokines (in particular IL-1α, IL-1β, and TNF-α), chemokines, chondroitin sulfate proteoglycans, reactive oxygen species, proteases, prostaglandins, cyclooxygenase-2, and heme oxidase[88,109,111], and are thought to broadly orchestrate the entire inflammatory response.

Circulating monocytes that infiltrate at the lesion site rapidly activate, whereupon they become essentially indistinguishable from microglia and effectively bolster their population[88]. Activated microglia also recruit additional circulating monocytes to the lesion site through the release of Monocyte Chemoattractant Protein-1 (MCP-1). Peak microglial activity is typically observed at 1-2 weeks post-implantation, though residual activity persists for a much greater period of time[9,13,71]. Of note is that while all activated microglia share morphological characteristics, a number of different phenotypes have been characterized which perform distinctive roles in the inflammatory response. The principal activated microglia phenotypes are M1, the "classical" subtype most responsible for pro-inflammatory cytokine release, and M2, an "alternatively activated" subtype responsible for response regulation and debris cleanup, which releases large amounts of the anti-inflammatory cytokines IL-10 and TGF-β[113]. It is thought that these phenotypes work in concert to regulate the inflammatory response, making them an attractive target for therapeutic approaches (such as the selective inhibition of M1 phenotype polarization by minocycline[114].

A number of other cell types are thought to play roles in the acute inflammatory response, though their contributions have been less well studied. Mast cells, for example, are immune cells similar to basophils that are native to many tissues including CNS, and are capable of degranulating and releasing histamine and heparin, increasing edema and BBB permeability while slowing coagulation. These cells are typically primed with IgE to respond to a particular antigen, and are often dependent on the activity of T cells[115]. Despite this, the blocking of cerebral mast cells has been reported to reduce edema and hematoma volume following intracerebral hemorrhage with markedly improved outcomes, leading many to believe that the mast cell may play a more profound role in CNS inflammation than previously thought[88]. Perivascular macrophages are another CNS-resident inflammation sensitive cell, and are monocyte-lineage non-ramified macrophage-like cells that occupy space between the neural parenchyma and the vascular endothelial cells. They are implicated with hematopoietic cell infiltration into CNS when activated, as well as MHC expression and TNF-α, IL-1β, and iNOS production. In later stages after injury (2-3 weeks), they have been observed to leave their perivascular position and migrate into neural tissue where they differentiate into ramified microglia-like cells that retain strong MHC immunoreactivity[108].

Other cell types known to infiltrate the CNS during cerebral hemorrhage events include lymphocytes such as T cells, which are known to play complex roles in inflammatory regulation and autoimmunity[108,116–122]. T cell-mediated autoimmunity is known to play a prominent role in several types of neurodegenerative pathology as well as hemorrhagic stroke and traumatic brain injury, though the healthy brain is typically well protected from this mechanism both by the BBB as well as neurons themselves, which suppress MHC expression in neighboring glia through interaction with the microglial CD200 receptor[123]. However, this suppression is strongly dependent on neuron health and electrical activity, and CNS tissue inflicted with neuron damage or silencing has been observed to lose this protection as microglia resume MHC expression and antigen-presenting capability[123]. While this mechanism has been shown to play a role in large-scale CNS hemorrhage, its relevance to microprobe implantation has not been well studied.

1.2.5 Chronic Inflammatory Response

While local astroglia initially activate at a very early time point post-implantation (often within 24 hours of lesion[108], commonly quantified by observing glial fibrillary acid protein (GFAP) expression), their distribution during the acute inflammatory period is sparse, with activation graded by distance from the lesion and the intensity of the initial trauma and acute response, up to around 500 μm from the implant surface. These astroglia are thought to be principally activated and directed by microglia-released cytokines, which tightly control the transformation of astroglia from protoplasmic to fibrillary form. Despite their early activation, astroglia exhibit a delayed response characterized by a slow migration to the implantation site, where they replace ensheathing microglia and enwrap local injured neurons with thin, flat processes[40,108]. This migration typically begins at 1-2 weeks post-implantation, characterized by an extension of astroglial processes toward the implant site. By three weeks, astrocytes will form an encapsulating sheath around the implant and nearby injured neurons, displacing microglia. The sheath grows increasingly compact and dense over time, though it is typically considered morphologically stable by the three week time point[7,8,40,71]. As it densifies, the interdigitating processes will adhere to each other, forming a multilayered stack of astrocytic lamellae surrounded by a network of extracellular matrix composed of tenascin, collagen IV, and chondroitin sulfate proteoglycans[108]. The development and maturation of the glial sheath is known to be directed by a number of pro- and anti-inflammatory factors[87,88,108]. A more detailed description of the roles of astroglial scar in neuroinhibition and degeneration will be discussed within chapter 2 of this dissertation.

The chronic inflammatory response period is also characterized by the progressive loss of recordable units, as described within the overview above. For many years, this performance loss was thought to be a consequence of astroglial sheath development; however, more recent studies have observed that the initial signs of unit loss do not synchronize with the peak time point of astrogliosis, instead lagging roughly one month behind it[8,9]. This unit loss is currently thought to be due to the progressive degeneration and death of neurons local (within ~100μm) to the probe surface, which initially worsens by week 8 post-implantation and persists for the duration of probe implantation, based on existing long term recording studies[5,11,13,16,21,37–39,42]. Neural degeneration and the resulting unit loss both exhibit a large degree of inconsistency and variability between probes and across time points, as well as non-uniformity around the same probe[124], though a correlation has been observed between neural degeneration and inflammation intensity[8]. It was also observed that different mechanisms of degeneration may play roles at different time points, with neuron and dendritic loss occurring by week 8 post-implantation, and axonal pathology by way of hyperphosphorylation of protein tau occurring after 16 weeks[8]. Demyelination (Fig 1.9) was also observed to occur in axons over 100 μm from the implant surface[71,124], though the effect did not appear to be uniformly distributed around the probe.

This neuronal degeneration is thought to result from a complex series of interrelated and cross-modulating neurotoxic factors and environmental stressors which combine to disturb the delicate homeostatic and signaling balance required for neuron survival[8,9] and drive local microglia, astroglia, and other cell types to convert from anti-inflammatory regulatory to pro-inflammatory reactive states. While acute neuronal loss is likely due to a combination of factors which result from implantation trauma and acute inflammatory response, including direct cell lysis, edema, oxidative stress, bilirubin toxicity, ischemia, acidosis, reactive microglial attack, CSPG-mediated inhibition, and pro-inflammatory cytokine and chemokine influence. Chronic degeneration on the other hand is likely due to self-perpetuating neurotoxic cytokine cascades coupled with mechanical stress due to probe micromotion and mechanical mismatch, vascular pulsation and damage, and other unknown factors. This progressive neurodegeneration was observed to continue at far chronic (16 week) time points, despite minimal microglial activation, stable and compact astroglial sheath, and little observable BBB leakage[9].

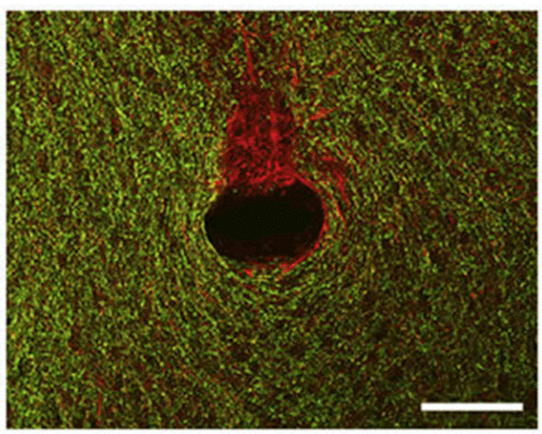

Figure 1.9: Demyelination observed around an implanted electrode in rat cortex at 12 weeks. Yellow is Myelin-Oligodendrocyte Specific Protein (MOSP), and red is neurofilament. SB = 100 μm. (Image from Winslow et al.[124] © Elsevier. Reprinted with permission).

1.3 DISSERTATION ORGANIZATION

This dissertation studies two approaches to studying and modulating the inflammatory response to implantable intracortical neural interfaces and advances the concept and theory behind controllable drug-release coatings and glial sheath modification. Chapter 3 includes a research study that is in preparation for submission to a peer-reviewed journal, and chapter 4 includes work that will serve as the foundation for a second study.

In chapter 2, we discuss the development of an *in vivo* model for the evaluation of the impact of the microinjection of the bacterial enzyme chondroitinase ABC (ChABC) on the astroglial sheath around implanted probes. Chondroitinase therapy is an experimental treatment involving the enzymatic digestion of chondroitin sulfate proteoglycans (CSPGs) from a CNS injury location, and has been applied with varying degrees of success to both spinal and brain injury models[125,126]. CSPGs are known to possess strong neural inhibitory signaling capabilities, and are thought to be a principal component of the barrier to neural regeneration across glial scar. The benefits that ChABC therapy may offer to the chronically-implanted intracortical electrode model have not yet been studied. This work describes the development of an intracortical ChABC microinjection model, and the study of the effects of ChABC microinjection to the glial scar that had evolved around the implanted indwelling injection cannula itself. The results demonstrate the successful digestion of CSPG around the injection cannula, as well as its effect on local serum protein content. Results also suggest that cellular morphology and activation within the sheath did not appear substantially affected. Our observations concurred with those published elsewhere[127] that CSPG expression peaks at 1 week post-implantation and rapidly diminishes thereafter, as we observed no discriminable CSPG signal at 18 days post-implantation.

In chapter 3, we study the neurophysiological recording capabilities, impedance characteristics, and drug releasing capabilities of a multiwalled-carbon nanotube (MWCNT)-doped PEDOT coating loaded with the anti-inflammatory corticosteroid dexamethasone. As discussed earlier, PEDOT has recently grown in popularity as an enhancement to chronic recording and stimulating microelectrodes due to its impedance-reducing capabilities and excellent electrochemical stability and charge storage capacity. PEDOT may also be employed as a controllable drug-releasing apparatus through the incorporation of a drug molecule as a counter-ion dopant. This drug-releasing capability has not been well evaluated *in vivo*. We studied the drug-release capacity of a PEDOT coating further modified with a MWCNT co-dopant intended to increase polymer surface area and drug yield. Following characterization and coating optimization, we coated the recording surfaces of platinum-iridium floating microelectrode arrays (FMAs) and chronically implanted them into rat visual cortex for an 11 day period. Drug release stimulation, neurophysiological recording, and impedance measurement were performed daily. Results demonstrated that the drug release stimulus was effective and did not result in atypical inflammatory response, changes to local neural activity, or substantial immediate changes to 1 kHz impedance. Coated probes demonstrated neurophysiological recording capability equivalent to that of uncoated probes. 1 kHz impedance of coated probes was observed to remain depressed for the initial 3 days post-implantation, but was then seen to increase rapidly and with distinctive phase characteristics to a point where it became statistically indistinguishable from uncoated probes by day 7 post-implantation.

In chapter 4, we discuss the development of an equivalent circuit model to better evaluate and interpret this *in vivo* impedance data. As the interface incorporates elements of both the conducting polymer coating as well as the evolving inflammatory tissue response, it presents a complex set of interrelated interfacial components that change dynamically with time. As most commonly-used simple models were found to be incapable of consistently fitting the recorded *in vivo* data, we adapted a more sophisticated transmission-line diffusion model to provide better representations of the various physical correlates. Fitting results suggest that uncoated and coated chronic impedance behavior was driven by two very different mechanisms, with uncoated electrode impedance more a function of subtle changes to metal surface features and high-frequency diffusion barrier development, while coated electrodes demonstrated large decreases of conducting polymer and electrode capacitance, likely a consequence of reduced effective surface area due to tissue encapsulation.

Chapter 5 summarizes the conclusions of the previous chapters and presents them in terms of their impact to the field of neural engineering. Additionally, it discusses new directions for research and opportunities for the application of techniques developed in this work.

2.0 THE DEGRADATION OF GLIAL SCAR THROUGH THE LOCAL DELIVERY OF CHONDROITINASE ABC

2.1 INTRODUCTION

As discussed in chapter 1 of this dissertation, perhaps the most detrimental aspect of the inflammatory response to the reliable long-term function of chronic intracortical recording electrodes is the progressive silencing, degeneration, and death of local neurons[7–9,38]. The mechanisms that lead to this neuronal loss are complex and interrelated, and are likely the product of a variety of environmental, biological, chemical, and mechanical stressors, many of which are unknown or not well understood. These stressors combine to disrupt the homeostatic balance necessary for neuron health and activity, leading to the degeneration and death of neurons or their migration away from the implant site. Informed electrode design and implantation techniques will likely be required to compensate for a majority of these stressors to maintain a healthy, active population of local neurons and achieve long-lasting and consistent recording performance[72]. This need can be seen reflected in a number of recent electrode concepts, such as ultrafine probes[38] which strive to minimize mechanical strain, vascular damage, and surface area to present as unobtrusive an implant as possible.

A principal inhibitory barrier to neural healing and regeneration in CNS at the implant/tissue interface is the astroglial sheath. While astroglial scarring has been known to be an antagonist to axonal regeneration and healing within spinal cord for over sixty years, it was originally thought to be a purely mechanical blockade[87,128]. Later observations revealed that a spinal lesion is capable of repelling regenerating axons even in the absence of dense glial scar, suggesting that more complicated biochemical factors may be at play[87,129]. It is now known that the astroglial sheath presents a rich neuro-inhibitory environment composed of both secreted soluble factors as well as extra-cellular matrix (ECM) signaling components[87], and serves an important role as a restrictive barrier between healthy and damaged tissue, isolating the lesion and limiting the volume of inflammation[130]. However, despite these protective properties, hypertrophic astrocytes within the sheath also restrict the ability of neurons to regenerate and regain some degree of connectivity across the scarred lesion. Important to note is that the astroglial scar is by no means the only barrier to neuronal regeneration within the healing lesion, as a host of other components are known to provide considerable inhibitory signaling as well, including damaged oligodendrocytes and myelin debris[131]. Hypertrophic astrocytes within the glial scar inhibit neuronal ingrowth through a variety of mechanisms, including the upregulation of factors including tenascin, ephrin-B2, semaphorin 3, slit proteins, and an assortment of chondroitin sulfate proteoglycans (CSPGs)[87]. Of these candidates, the CSPGs have perhaps the most demonstrated ability to inhibit axonal regeneration[125,132–136].

CSPGs are a family of ECM proteins that play a diverse assortment of roles within the body, particularly in cartilage and scar tissue where they contribute structural integrity and compression resistance. Structurally, CSPGs consist of a core protein to which is covalently attached one or more chondroitin sulfate glycosaminoglycan (CS-GAG) sugar chains[125,137]. Each CS-GAG is composed of a linear unbranched chain of alternating monosaccharide units, D-glucuronic acid and *N*-acetyl-D-galactoseamine, and is bound to the core protein by way of a Xyl-Gal-Gal-GlcA tetrasaccharide linking region to a serine residue[137]. The CS-GAGs are classified in terms of their sulfation, with the four known types (chondroitin sulfate A, C, D, and

E) being differentiated by the presence or lack of sulfate molecules at the 4 and 6 carbons of Gal*N*Ac and the 2 carbon of GlcA[138] (Fig. 2.1). Additionally, a large variety of CSPGs have been classified in terms of core protein composition and CS-GAG length. The most common and relevant to CNS: aggrecan, brevican, versican, and neurocan (together collectively known as the *lecticans*) are large, bulky, aggregating proteoglycans that strongly interact with other ECM and membrane proteins through their highly charged sulfate groups. The lecticans are secreted by most glia and, despite existing at miniscule concentrations in healthy brain, nonetheless play a critical role as the major component of the *perineuronal net*, or the ECM network that surrounds neurons and stabilizes synapses[139]. They are also known to play a crucial part in development where they serve as "master regulators" of neuron migration, axon guidance, and neurite outgrowth[140]. Following CNS injury, the secretion of lecticans is greatly upregulated by reactive astroglia and microglia in the glial scar[87] though at differential time points, with brevican, versican, and neurocan being expressed very early, peaking at one to two weeks and returning to baseline levels by four to eight weeks post-injury, while phosphacan was not observed to be expressed until four weeks post-injury, peaking at roughly two months[141].

An important tool in studying the function of CSPG in CNS has been chondroitinase (Fig. 2.2), a bacterial enzyme that acts by cleaving the linkage between disaccharide units within the CS-GAG side chains, effectively stripping them from the CSPG core protein. Chondroitinase exists in a number of different forms, each specific to the sulfation state of the CS-GAGs it is capable of cleaving. The most universal, chondroitinase ABC (ChABC), is able to cleave CS-A, CS-C, as well as dermatan sulfate. By using chondroitinase to selectively degrade CSPGs, the mechanisms of their inhibitory influence on neurons and axon growth cones have been further elucidated and found to be multi-modal. Microinjection of ChABC into lesioned spinal cord was

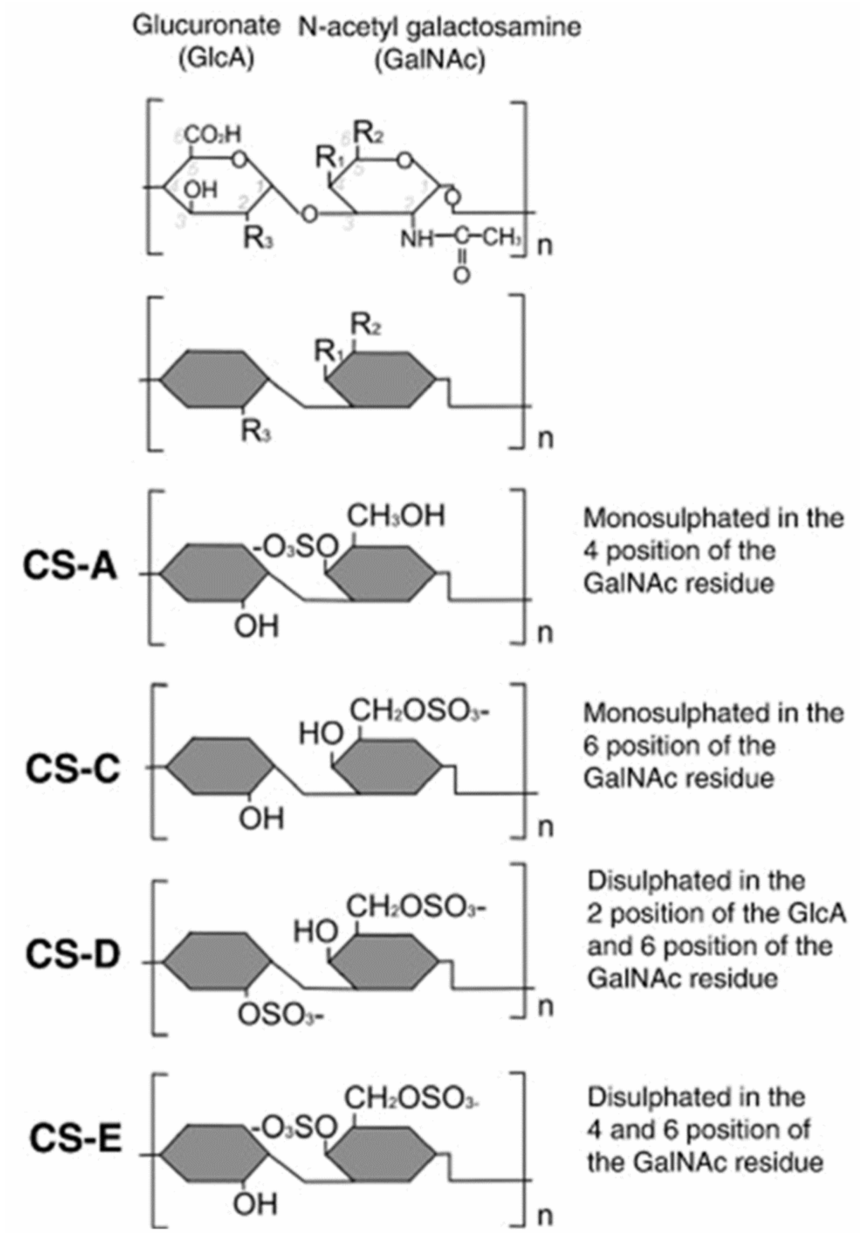

Figure 2.1: Structure of constituent CS-GAG disaccharide. Illustration demonstrates placement of sulfate groups for known chondroitin sulfate variants (Diagram by Galtrey and Fawcett 2007[142], © Elsevier. Reprinted with permission).

shown to cleave CS-GAGs from CSPG *in vivo*, and produced enhanced axonal regeneration[125,134,135]. Similar microinjections in healthy cerebellum[143], hippocampus[144], cuneate nucleus[145], and spinal cord[146] produced enhanced neurite sprouting and local plasticity. Paradoxically, earlier work *in vitro* observed that while both intact CNS-derived CSPGs and stripped CSPG core proteins were able to dose-dependently inhibit outgrowth from cultured neuronal PC12D cells, unbound CS-GAGs had no discernible effect even at high concentrations[147], suggesting that much of the neuromodulatory ability of CSPG may depend on the concerted contributions of several CSPG and ECM components. For example, it was found that while explanted rat glial scar tissue treated with ChABC demonstrated increased neurite outgrowth, this enhancement was partially reversed when the ChABC-treated explant was subsequently exposed to anti-laminin antibody[133].

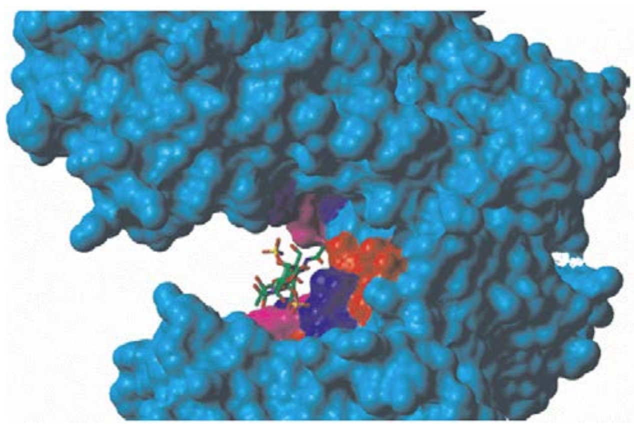

Figure 2.2: Rendering of the bacterial enzyme chondroitinase ABC. Demonstrates binding with dermatan sulfate (Figure from Prabhakar[148], © 2005 Biochemical Society. Reprinted with permission).

Later work revealed a number of direct receptor-mediated inhibitory pathways between CSPGs and neurons, including epidermal growth factor receptor (EGFR)-mediated increase in calcium levels in affected cells[149], interactions with protein tyrosine phosphatase sigma (PTPσ) receptors[125], and the activation of Rho-kinase, which results in growth cone collapse[150]. Studies targeting these pathways have reported success in negating the inhibitory properties of CSPG[149,151]. These inhibitory mechanisms also appear dependent on the sulfation state of the CS-GAG constituents of CSPG, and it was shown that the down-regulation of sulfotransferase resulted in greatly reduced neural inhibition[137]. Additionally, ChABC treatment is thought to provide additional benefits through the creation of disaccharide digestion products, which are known to promote neurite outgrowth and neuroprotection in local neurons and microglia[152].

Due to these benefits and few apparent negative consequences, ChABC treatment has become a popular direction in spinal and brain regeneration research[125]. Typical studies have taken one of two approaches: either the direct administration of ChABC to the lesion site, sometimes in conjunction with a bridge or graft[125,134–136,153–159], or the administration of ChABC to an uninjured nucleus upstream from a lesion, with the goal of digesting perineuronal nets and "unlocking" neurons to promote enhanced plasticity[145,146]. The former approach was first explored by Lemons et al. in 1999[154], who first demonstrated the enhanced production of CSPGs following spinal contusion, as well as the digestion of those CSPGs *in vivo* by way of a local ChABC injection. In 2001, Moon et al. demonstrated the regeneration of CNS axons following ChABC injection to a nigrostriatal lesion[155]. Bradbury et al. demonstrated partial functional recovery following ChABC treatment to a spinal lesion in 2002[134]. Subsequently, an assortment of studies has been performed demonstrating degrees of functional recovery following ChABC treatment to a variety of CNS lesion locations[125]. However, a number of limitations have also been observed. While ChABC treatment has been effective in promoting recovery following slicing injuries, its benefit following more clinically relevant pinching and contusional injuries has been limited, in both spinal cord[158] and brain[126]. Garcia-Alias et al. observed that while axons were regenerated following ChABC treatment administered seven days following spinal injury, functional recovery was reduced compared to animals where ChABC was administered immediately following injury[160]. There has additionally been some question regarding the susceptibility of ChABC to thermal degradation. While Tester et al.[159] observed a significant reduction in ChABC activity *in vitro* within three days at 37° C, Lin et al.[156] demonstrated continued ChABC digestion in CNS *in vivo* 10 days after a single injection.

While ChABC treatment has been extensively employed in spinal and brain lesions, its applicability to chronically implanted devices has not been well studied. As discussed in chapter 1 of this dissertation, while the inflammatory tissue responses to an acute lesion and to an implanted probe share many common elements, they have many differences as well. While both situations exhibit similar patterns and time courses of CSPG expression (peaking at 1 week and gradually returning to baseline by 3-4 weeks), chronic astroglial and microglial activation is significantly more pronounced around the chronic implant, suggesting a richer pro-inflammatory environment. The purpose of this study was to develop an effective model for ChABC injection into CNS by way of a chronically implanted cannula. The effect of ChABC digestion was then observed within the tissue response to the cannula itself. We later coupled the cannulae with recording electrodes physically adhered to the cannulae surfaces to study chronic impedance changes following ChABC treatment, in preparation for the next phase of study where cannulae would be implanted in parallel with a multielectrode array. While this next phase has not yet been initiated, this chapter serves to chronicle the successes and challenges faced during the development of the injection model.

2.2 EXPERIMENTAL

This study was carried out as a series of developmental and optimization steps with the goal of developing an effective model of ChABC microinjection for use in subsequent studies as a component of a microelectrode array. Common methods utilized throughout the study are detailed within this section, while a narrative of model development is provided in section 2.3.

2.2.1 Surgical Implantation

Infusion cannulae, including the model employed in this study, typically feature a *guide* cannula which is implanted into tissue and a separate *injector cannula* which is slid inside the guide cannula to perform the actual infusion at the time of injection. During implantation and until the time point of injection, an *obdurator* (typically a solid rod of plastic or steel of outer diameter matching the inner diameter of the guide cannula) is placed inside the guide to close it, preventing tissue ingrowth and infiltration of contamination.

Throughout this study, guide cannulae were implanted either unilaterally or bilaterally into the parietal cortices of male Sprague Dawley rats under the guidelines of the University of Pittsburgh IACUC: Each animal was anesthetized under 3% isoflurane, weighed, and mounted onto a stereotaxic frame (Narishige USA, Inc., East Meadow NY). The top surface of the skull was exposed and a 2 mm diameter circular craniotomy centered at 1 mm post Bregma and 3.5 mm lateral to midline was made using a high speed hand drill and fine rongeurs. Saline was applied continuously onto the skull to suppress heat from the high speed drilling. Four skull screws were mounted in a uniform arrangement around the craniotomies. Following dural puncture, stereotaxic insertion of each guide cannula (with obdurator inserted, EtO sterilized) was accomplished using a small clamp mounted to a hand-driven microdrive. Each cannula was manually lowered at a consistent pace into cortex until the upper surface of the skull was 1 mm distant from the lower surface of the cannula head socket, resulting in a tissue depth of ~2 mm. With the cannula held firmly in place, the craniotomy was sealed using UV-cured dental cement (Pentron Clinical, Orange CA), liberally applied onto the cannula head socket and around nearby skull screws. Once both cannulae were in place, a robust head cap was molded in place using dental cement (Cerebond, Plastics One, Inc., Roanoke VA). A protective flexible plastic cap was adhered to the hardened cement using hot glue to provide additional protection to the guide cannula ports. Animal temperature was maintained throughout the procedure using a warm water pad (HTP 1500, Adroit Medical Systems, Loudon TN) and homeostasis was maintained using regular injections of sterile Ringer's solution. 0.3mg/kg buprenorphine was administered twice daily for three days as a post-operative analgesic. Animals were provided with soft water-based diet gel immediately after surgery, and food and water were provided *ad libidem* for the remainder of the experiment. All animal care and procedures were performed under the approval of the University of Pittsburgh Institutional Animal Care and Use Committee and in accordance with regulations specified by the division of laboratory animal resources.

2.2.2 Cannula Selection and Fabrication

Initial work was performed to select and test an appropriate microinjection cannula. We initially selected a model available from Plastics One featuring a polyether ether ketone (PEEK) cannula tube with an externally-threaded head socket (Fig. 2.3a); however it was found that the screw-on obdurator cap did not leave enough clearance underneath to allow for the application of a sufficient amount of dental cement, and the trial animal was able to fracture the head cap. An alternate version of this cannula was procured which featured a flange on the lower surface of the head socket, but during a trial implantation was found to be too awkward to position properly. Thus, the Plastics One model was abandoned.

In its place, we adopted polyurethane guide cannulae (OD: 550 µm, ID: 360 µm) produced by CMA Microdialysis AB (distributed in the USA by Harvard Apparatus, Hollison MA), sold as a component of a microdialysis probe (Fig. 2.3b). These cannulae feature a "cup" type head socket as opposed to the external threading of the previous model, which allows cement to be applied liberally around the cannula without risk if interference with cannula function, allowing for a simpler surgical procedure and a more robust head cap. Initial attempts were made to fashion an injector cannula by carefully cutting the dialysis tip off of a probe, but this yielded unacceptable resistance to fluid flow. Instead, an injector was hand-made using 28 gauge SS hypodermic tubing which was cut to a convenient length and deburred. The injector was bonded to flexible PTFE tubing using epoxy, and injector length was set using small plastic spacers.

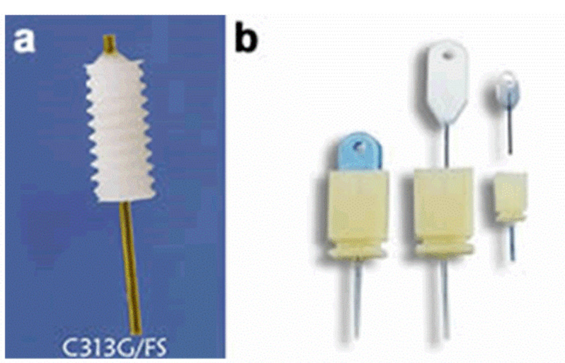

Figure 2.3: Example commercial guide cannulae. a) Plastics One model (© Plastics One Inc., used with permission). b) CMA models, demonstrating "cup" head socket and insertible obdurators. Small murine model on right was employed in this study (© CMA Microdialysis AB, used with permission).

2.2.3 Microinjection

Microinjection procedures were typically performed either 10 or 18 days post-implantation, to capture either the period of peak CSPG expression, or the period of peak astroglial sheath development. During the injection procedure, the animal was sedated using 3% isoflurane, and placed onto a microwaveable warming pad. The protective plastic cap was carefully removed, exposing cannulae ports. The obdurator of the guide cannula through which injection was performed was removed and placed into a 70% ethanol bath for cleaning. The injector was ethanol sterilized and connected to a 10 μL glass syringe (Hamilton Co., Reno NV), and tubing was pre-charged with either sterile saline or mineral oil (for enzyme or antibody injection). 4 μL of treatment solution was drawn into the injector tip, and the injector was slid into the guide cannula port until the tip of the injector was flush with the end of the guide. The Hamilton syringe was mounted onto an electronically-controlled syringe pump (Fisher Scientific, Waltham MA), and injection was performed at a rate of 6 μL/hour for 20 minutes. Similar injection rates and volumes have been employed in other cortical microinjection studies[161–163]. After the injection was completed, the injector was removed and the obdurator replaced. Animals scheduled for immediate histology were allowed to rest for an additional 40 minutes to allow for enzyme diffusion and activity before perfusion. Generally, in bilateral cannula-implanted animals, one side was used for experimental injection and the other side for control (bacteriostatic 0.9% sodium chloride, Hospira, Inc., Lake Forest IL).

Chondroitinase ABC used for injection was purchased in lyophilized powder form (Sigma-Aldrich, St. Louis MO) and was dialyzed and diluted to a working concentration of 100 U/mL before being aliquoted and frozen. Bioactivity of each batch was evaluated using sectioned chicken embryo.

2.2.4 Dye-labeled Antibody Infusion Test

To determine the approximate volume and pattern of enzyme penetration within tissue following microinjection, a test was performed by way of the substitution of Alexa488-labeled antibody (2 mg/mL goat anti-rabbit, Invitrogen). Eighteen days after cannula implantation, microinjection of 2 µL of labeled antibody solution was performed as described above, except that following the 40-minute post-injection period the animal was immediately euthanized and the brain was removed without fixative perfusion. After removal, the brain was immersed into 4% paraformaldehyde for five minutes and flash-frozen by immersion in liquid nitrogen-cooled isopentane. The brain was blocked, cut into 20 µm sections, and imaged using a fluorescence microscope to observe the extent of antibody penetration.

2.2.5 Hybrid Cannula/Electrode Study

A preliminary study was performed to evaluate the impedance changes exhibited by electrodes following chondroitinase ABC treatment. Simple electrode/cannula implants were hand-fabricated by adhering two tungsten microwire electrodes (Microprobes for Life Science, Gaithersburg MD) to opposite sides of CMA cannulae using UV-activated cement (Fig. 2.4). The initial array was fabricated with electrodes flush against the sides of the cannula to attempt to maximize the exposure to enzyme, but later arrays were fabricated with electrodes spaced roughly 1mm lateral from the cannula tip. Electrode impedance was assessed in PBS using a potentiostat (Fas1 Femtostat, Gamry Instruments, Warminster PA) before EtO sterilization. Implantation was performed as in 2.2.1 above, only with a larger craniotomy to accommodate the electrodes. Periodic impedance measurement was performed before and after injections.

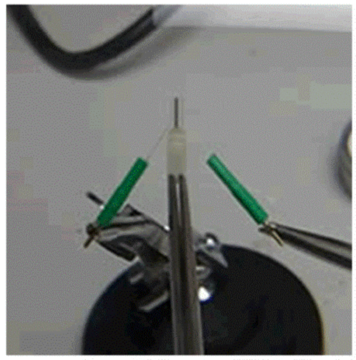

Figure 2.4: A hybrid cannula/electrode implant. Features 1 mm wire spacing from cannula.

2.2.6 Histology

At select days post-implantation, animals were sacrificed and perfused according to University of Pittsburgh IACUC approved methods. Each animal was deeply anesthetized using 65 mg/kg ketamine, 7 mg/kg xylazine cocktail. Once the proper plane of anesthesia was observed, animals were transcardially perfused using a warm PBS flush followed by ice cold 4% paraformaldehyde. Animals were decapitated and heads were post-fixed in a 4% paraformaldehyde bath at 20°C overnight. Following post-fix, the skull was dissected and cannulae carefully removed to avoid incidental tissue damage. Whole brains were then removed and soaked in a 15% sucrose bath at 20°C overnight followed by a 30% sucrose bath until brains were fully impregnated. Brains were then blocked and carefully frozen using a 20% sucrose/OCT blocking media blend and dry ice. Tissue was typically sagittally sectioned parallel to the axis of the cannulae using a 14 μm section thickness.

Tissue sections were hydrated using PBS and exposed to a 0.5 mM $CuSO_4$ solution for 10 minutes to reduce hemosiderin-dependent autofluorescence[164]. Following exposure, sections were washed with PBS (3x5min) and incubated in a blocking solution (10% goat serum, 3%

triton X-100) for 1 hour at ambient temperature. Following blocking, sections were incubated in a primary antibody solution consisting of 5% goat serum, 1.5% triton X-100, and antibodies against microglia (1:200 mouse anti-IBA1 and anti-ED1, Abcam, Cambridge MA), astroglia (1:500 rabbit anti-GFAP, Dako, Glostrup, Denmark), neurons (1:500 rabbit anti-NeuN and anti-NF200, Invitrogen, Grand Island NY), immunoglobin (1:500 anti-IgG and anti-IgM, courtesy of Dr. Carl Lagenaur), and chondroitin sulfate GAG (hybridoma-derived CS56 antibody, courtesy of Dr. Willi Halfter) for 18 hours at 4°C. The next day, sections were washed with PBS (3x5min) and incubated in a secondary solution consisting of 5% goat serum, 1.5% triton X-100, and antibodies (1:1000 goat anti-mouse Alexa 488, Invitrogen, and 1:1000 goat anti-rabbit Alexa 594, Invitrogen) for two hours at ambient temperature. Sections were then rinsed with PBS for 5 minutes, exposed to 1:1000 Hoechst 33342 (Invitrogen) for 10 minutes, and washed in PBS (3x5 minutes) before being coverslipped with Fluoromount-G (Southern Biotech, Birmingham AL). Sections were promptly imaged using fluorescence microscopy (Axioskop 2 MAT, Carl Zeiss, Inc., Oberkochen, Germany, equipped with an X-Cite 120 fluorescence illumination system, EXFO, Inc., Mississauga, Ontario).

2.3 RESULTS AND DISCUSSION

This study was undertaken to establish a “proof of concept” of the microinjection of ChABC into cortex through a chronically implanted cannula, to evaluate its effects and to resolve technical challenges before integration with more sophisticated recording systems. As such, it was performed as a series of trial implantations, each attempting to resolve principal challenges encountered in the previous trial through modifications to implant geometry, surgical or microinjection technique, histology methods, and critical time points. This section will summarize a number of the more critical challenges as well as the resolutions applied, and will report on the performance of the final model protocol.

2.3.1 Microinjection Technique

Once an acceptable cannula design had been selected (as described in section 2.2.2), a study was performed to evaluate the extent of drug penetration into tissue following microinjection. Due to the size and nature of the cannula, it cannot be easily simplified to a point source for diffusion modeling due to the presence of significant backflow up the shank of the cannula. This backflow or "leak-back" of infusate up the cannula surface is due to a number of factors including local tissue damage, elastic deformation, and pressure gradients, and has been studied in detail[165–168] as it is typically an undesirable feature of injection. However, as this study is specifically targeting the scar tissue around the cannula surface itself for treatment, infusate backflow is desired.

Injector cannulae are typically designed to extend a certain distance into tissue from the end of the guide cannula when inserted, infusing a bolus of fluid well below the guide cannula while also generating a fresh lesion in tissue. For the purposes of this study, the injector cannulae were fabricated significantly shorter, roughly 0.5mm short of the guide cannula tip, conceptually leading to significantly less strain and injury to tissue on injector insertion. To visualize the penetration profile of protein-laden infusate into tissue, a dye-labeled antibody infusion study was performed, as described in 2.2.4. IgG possesses only slightly higher MW than chondroitinase ABC (~150 kDa and ~120 kDa, respectively). Resulting images are shown in figure 2.5. Note lateral penetration of dye as well as prominent backflow pattern up cannula surface. Measurements indicate antibody penetration to roughly 1 mm from cannula at tip depth.

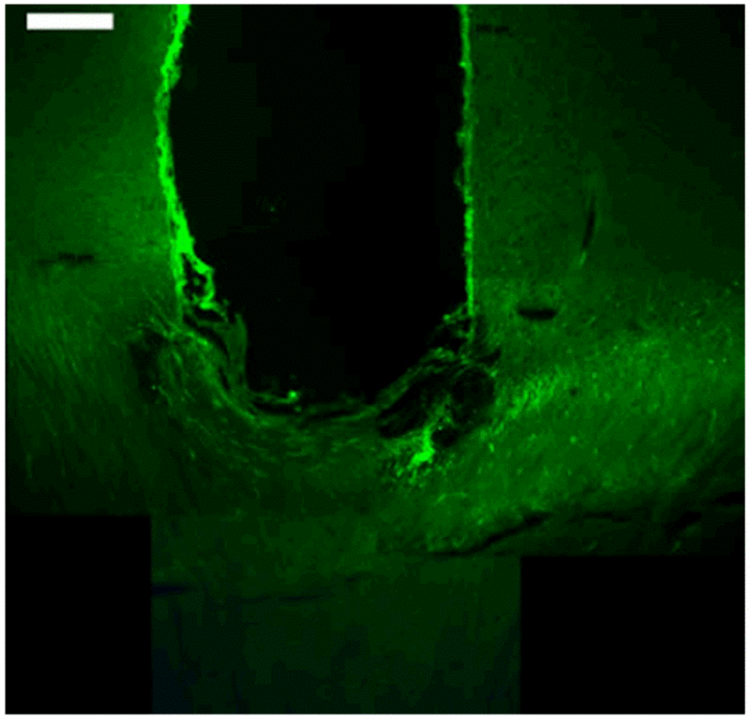

Figure 2.5: Dye penetration following microinjection. Composite image demonstrating the penetration of Alexa488-labeled IgG into cortical tissue following infusion of 2 µL sample. SB = 200 µm.

2.3.2 Histology Methods

Polymer guide cannulae were employed due to the possibility of sectioning being performed with cannulae in place within brain. However, early trials revealed that cannulae were only very loosely bound in tissue and would often slip out of the lesion during dissection or sectioning, making the method too inconsistent to employ for the remainder of the study. Early observations of tissue with intact cannulae revealed that the lesion conformed closely to the cannula surface.

Initial histology was performed using horizontal sections from the upper surface of the brain perpendicular to the cannula axis. While this method provided a large number of sections for labeling, it did not allow for the visualization of immunoreactivity expression gradients down the length of the cannula. Thus, sagittal sectioning was adopted, which allowed for the entirety of the cannula to be observed within a single section (Fig. 2.6). As tissue at the cannula tips often demonstrated a large degree of irregularity due to the stresses of obdurator removal, a length of cannula wall within 1 mm of the cannula tip was selected for use in comparisons.

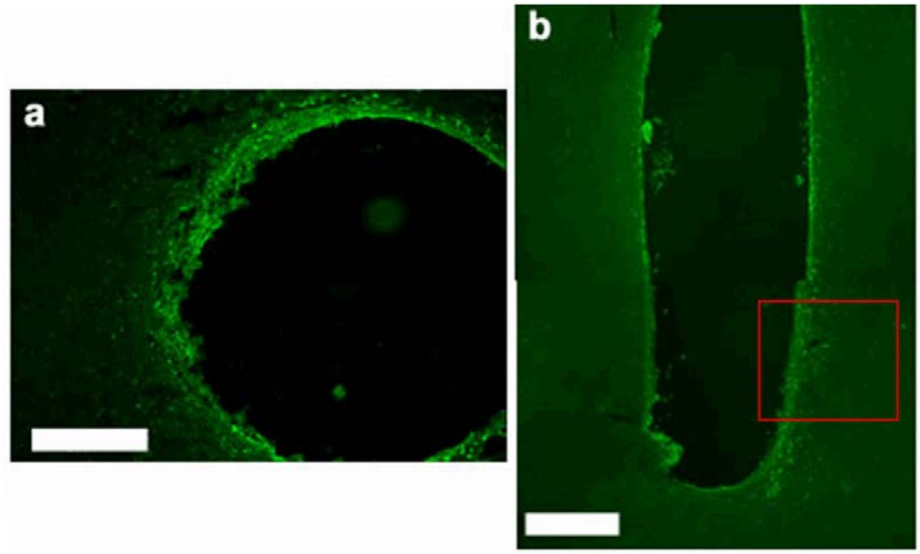

Figure 2.6: Horizontal vs. Sagittal. a) Example horizontal section (GFAP). b) Example composite sagittal section (ED1). Red box indicates typical area used for immunoreactivity comparison. SBs = 200 µm.

2.3.3 Immunoreactivity Interference of Serum Immunoglobin

Early ChABC injection and histology trials revealed an interesting phenomenon, in that secondary antibodies were able to bind to tissue features without primary antibody exposure. Moreover, this binding appeared to be attenuated by tissue ChABC exposure, and was specific to anti-mouse Ig (Fig. 2.7a&b). Binding occurred throughout the tissue, though it appeared to be concentrated within local cells (likely astroglia based on morphology) (Fig. 2.7c). As our anti-chondroitin sulfate GAG primary antibody (CS56) and several other immunolabels were derived from mouse hybridoma, this phenomenon had the potential to significantly confound observations. Based on specificity of secondary antibodies involved, it was assumed that the mechanism of interference was the binding of anti-mouse Ig secondary antibody to rat serum Ig that had infiltrated the lesion site through blood brain barrier leakage since implantation. Sensitivity of this immunoreactivity to ChABC treatment was assumed to be due to this serum Ig being released from ECM following enzymatic digestion, which was later observed using anti-rat Ig labeling. To compensate for this issue, we acquired highly cross-adsorbed secondary antibodies.

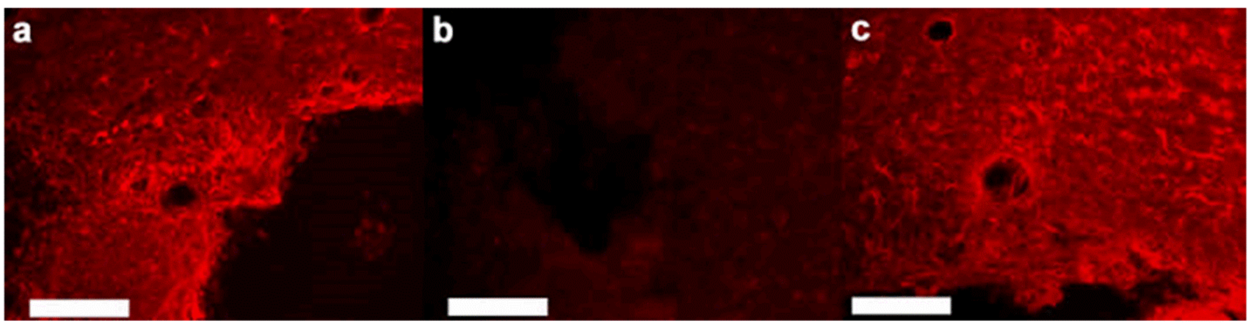

Figure 2.7: Interference of released serum protein on CS labeling. a) Immunoreactivity of alexa594-labeled anti-mouse IgG secondary antibody with tissue in absence of primary antibody. b) Comparative immunoreactivity of alexa594-labeled anti-rabbit IgM to the same tissue. c) Example image demonstrating preferred binding within stellate structures at interface (likely astroglia). SB = 200 µm.

These antibodies appeared to substantially reduce but not completely eliminate the binding, effectively limiting the sensitivity of the labels. While chondroitin sulfate expression was sufficient at 10 days post-implant to overwhelm the serum Ig binding, at 18 days post-implant it was not expressed strongly enough to allow for confident comparisons. To label chondroitin sulfate more specifically, it may be necessary to move to a lectin-based label such as *wisteria floribunda* agglutinin, though this was not performed during the course of this study.

2.3.4 Chondroitin Sulfate Digestion after ChABC Infusion

Once the microinjection model was optimized to a satisfactory degree, we performed immunohistological imaging to characterize the inflammatory response at the cannula interface, and demonstrated the ability of the ChABC infusion to digest CS-GAG within the reactive tissue. Activated astroglial and microglial marker expression within the inflammatory tissue at 10 and 18 days post-implantation appeared similar to typical responses observed around smaller probes, with a tight core of activated microglia at the tissue/cannula interface, and a more diffuse field of activated astroglia that was observed to condense at the interface at the later time point (Fig. 2.8). No visually apparent change was observed in microglial or astroglial marker expression 1 hour or 1 week after ChABC treatment. As discussed in 2.2.3 above, CS-GAG marker expression was prominent within the inflammatory region at 10 days but was not discernible at 18 days, which conforms to the known time course of lectican expression[141].

ChABC infusion resulted in an immediate reduction in 10-day CS-GAG marker expression in inflammatory tissue around the cannula consistent with enzymatic digestion (Fig. 2.9a). It was also observed to result in an immediate reduction in both rat IgG (Fig. 2.9b) and IgM (Fig. 2.9c) local to the cannula, presumably due to release of trapped serum Ig within the ECM.

2.3.5 Hybrid Electrode-Cannula Implant Performance

As mentioned in section 2.2.5, two initial electrode-cannula hybrid devices were fabricated and implanted bilaterally into rat parietal cortex. These devices were fashioned such the electrodes were flush against the side of the central cannula in order to ensure exposure to infused solution. However, upon comparing subsequent impedance measurements over the ongoing days post-implantation, three of the four electrodes did not exhibit the characteristic increase in 1 kHz impedance typically observed around implanted electrodes and remained nearly flat for the entirety of the initial 24 day pre-injection period, as well as through the course of injections.

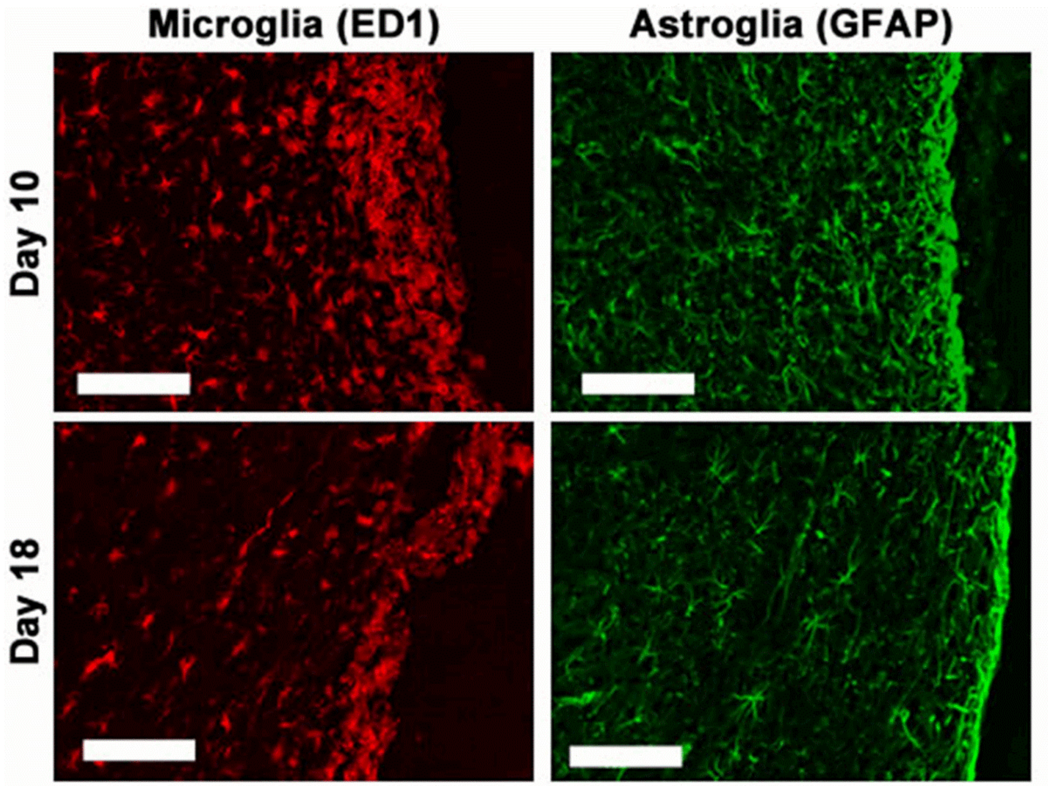

Figure 2.8: Glial sheath formation. Expression of activated microglial (ED1) and astroglial (GFAP) markers along the cannula/tissue interface at two time points. Note consolidation of both cell types into a compressed layer at the cannula surface. SB = 100 µm.

Upon experiment completion and probe explantation, it was observed that the electrode that had exhibited normal impedance behavior had actually separated from the surface of the cannula during implantation by roughly 1 mm. Based on this, it was speculated that the current path of the other three electrodes had shunted up the outer surface of the cannula and thus bypassed the tissue response entirely, resulting in low, steady-state impedance characteristics.

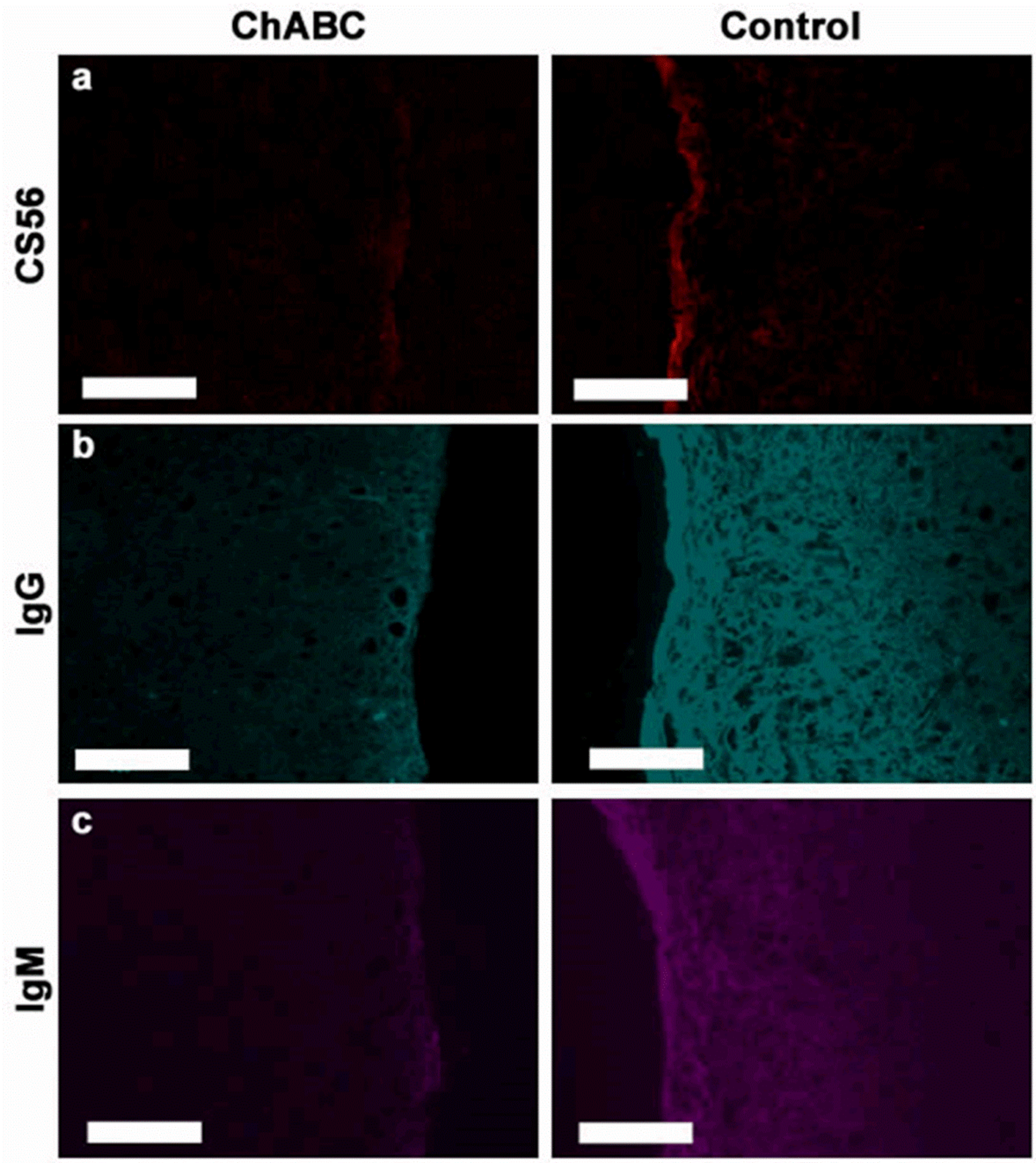

Figure 2.9: Digestion and serum protein. Effect of 2 µL (6 µL/hr) 100 U/mL ChABC versus saline control infusion on a) CS-GAG (CS56), b) IgG, and c) IgM after one hour post-infusion. Cannulae implanted for 10 days pre-infusion. Enzyme injection visibly reduced expression of all three markers. SB = 100 µm.

In light of these observations, a second pair of electrode-cannula implants was prepared with electrodes spaced 1 mm from each cannula. Probes were implanted and allowed to develop a response for 22 days, with periodic impedance measurement. On the 22th day, both cannulae received a saline control infusion. Following this, impedance was measured daily for four days at which point a ChABC infusion was applied to both cannulae.

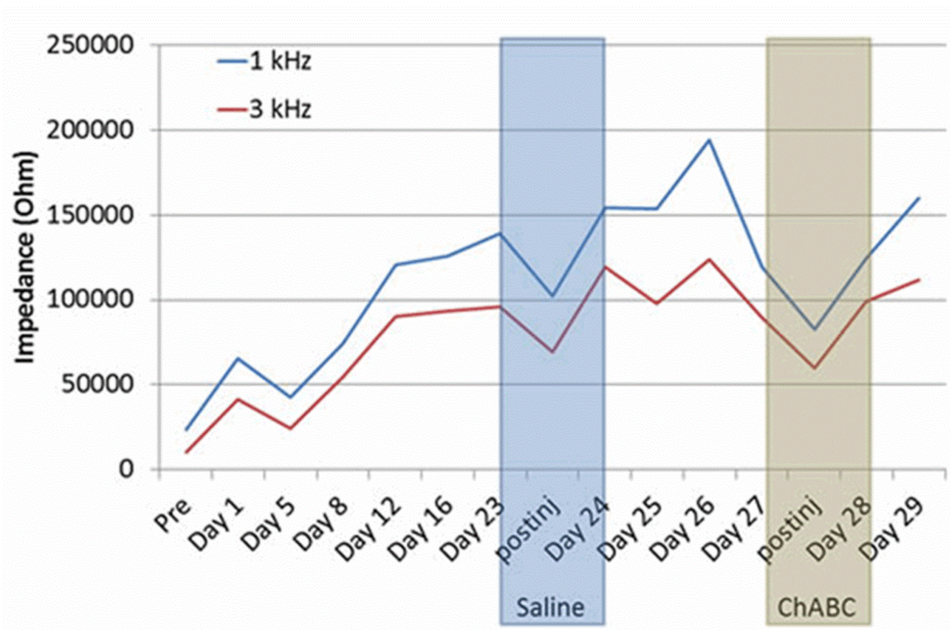

Figure 2.10: Impedance measurement of a cannula-electrode hybrid probe. “Pre” represents pre-implantation impedance in PBS, “day 1” is the probe impedance the day of implantation, and “postinj” is impedance measured 1 hour following injection on days 23 and 27.

A record of impedance measurements at 1 and 3 kHz for a representative electrode is shown in figure 2.10. It was hypothesized that CS-GAG may contribute to electrode impedance by acting as a barrier to ionic diffusion within the ECM of the glial scar, and that digesting it with ChABC would thus eliminate its contribution. However, it was observed that impedance of the electrode reduced immediately after *both* saline control and ChABC infusion, and returned to previous levels within one day. As 1 kHz impedance was extremely variable throughout the trial, as apparent within the record, a large number of additional repetitions would be required to evaluate changes with statistical confidence. However, this single trial suggests that ChABC treatment may not lead to a chronic effect on electrode impedance. The immediate drop in impedance following both infusions is speculated to be due to a momentary swelling of tissue with infusate.

While these probes had the potential to provide interesting dynamic impedance information, the technical difficulties involved in their fabrication and use made them impractical for anything beyond a pilot study. Electrode spacing could not be carefully controlled with the fabrication tools available, and the cement bond was prone to mechanical failure. Additionally, only two electrodes could be placed around each cannula, greatly limiting study efficiency. A superior option would be to incorporate an injection cannula into a commercially-available multi-electrode array, which would allow for measurement and recording from a plethora of precisely-positioned electrodes with each treatment.

2.4 CONCLUSION

During the course of this study we were able to develop and demonstrate a model for the infusion of chondroitinase ABC into cortex. A number of design and application challenges were encountered and circumvented through modifications to hardware and techniques. The model should be easily adaptable to a more sophisticated electrode array/injector system that will allow for a more profound analysis of the effects of CS-GAG digestion on inflammatory tissue response, electrode impedance, and neurophysiological recording performance.

2.5 ACKNOWLEDGMENTS

This research was funded by the National Science Foundation CNBC IGERT grant DGE-0549352 and the National Institute of Health R01NS062019. Much appreciation is given to Dr. Willi Halfter and Dr. Carl Lagenaur for their assistance and immunohistological reagents.

3.0 IN VIVO ELECTRICAL STIMULATION OF A DEXAMETHASONE-RELEASING PEDOT/MWCNT NEURAL ELECTRODE COATING

3.1 INTRODUCTION

Neural prostheses have seen effective use in a variety of applications, including auditory prostheses, visual prostheses, and brain-computer interface[1–3,5,6,68]. Several examples employ arrays of penetrating microelectrodes that are implanted into cortex to record neural activity with single cell resolution[1,5,12,15,16,37,39,58]. When chronically implanted, these electrodes typically suffer a large degree of variability and deterioration of recording performance metrics such as single-unit yield and signal-to-noise ratio over months to years[21]. Such unreliable recording performance has become a principal obstacle against the more widespread clinical translation of intracortical electrodes. The large degree of variability and degradation are thought to be a product of several factors both abiotic and biotic[13,21]. Principal among these factors is the degree of tissue inflammation elicited by electrode implantation and chronic presence. Several interrelated inflammation mechanisms including the development of an encapsulating glial scar and the degeneration and death of local neurons have been theorized to play important roles in this recording quality deterioration[7–9,13,38,40,71–73,92,169].

In light of these observations, novel intracortical electrode design has largely focused on improving probe electrical characteristics[170], reducing tissue reactivity through changes to electrode geometry[38,171–173], flexibility[174–177], and surface properties[124], employing biomaterial strategies to promote tissue stability[38,178–183], and incorporating drug release systems to introduce anti-inflammatory agents[127]. While drug release systems intended for intracortical electrode integration have typically been limited to microfluidics or slow-release gels and coatings, systems utilizing conducting polymers have been explored due to their on-demand release capabilities[184,185].

Drug delivery from conducting polymers generally involves the incorporation of the drug into the conducting polymer as a dopant that is then released using an applied electrical stimulus[186]. The basis of this capability is the ability of the conductive polymer to "switch" from a charged oxidized state to a neutral reduced state upon application of a current pulse with voltage sufficient to cross the reduction potential of the material. Small charged species introduced as a counter-ion to the oxidized conducting polymer are released once the coating is converted to its neutral state, whereupon they diffuse into the surrounding environment. This mechanism may be used to release a wide variety of species, including anionic, cationic[187,188], and neutral[189]. The selection of dopant has also been shown to have an effect on other electrode properties such as biocompatibility and *in vitro* neuron survival[190].

While drug release through conducting polymer stimulation has been extensively studied *in vitro* (as reviewed by Svirskis 2010[186]), the translation of this technology *in vivo* has been limited. The bulk of research has focused on the conducting polymer polypyrrole (PPy), due to its well characterized synthesis, morphology, and release performance. However, there are a number of detrimental aspects of Ppy that limit its applicability to chronic *in vivo* applications[191]. These include a significant degree of α-β' coupling which leads to structural disorder, limited electrochemical response, and over-oxidation susceptibility[192], as well as a vulnerability to biological reducing agents such as glutathione and dithiothreitol[193]. An alternative is poly(3,4-

ethylenedioxythiophene) (PEDOT), which has been shown to possess significantly improved electrochemical stability[191,194,195] and electrolyte compatibility[196]. PEDOT has been successfully integrated onto chronic intracortical recording electrodes in a number of studies[191,197–208].

The application of PEDOT onto microelectrode recording surfaces has been shown to provide a number of intriguing electrochemical benefits in a manner that is simple, cost effective, and applicable to most existing electrode designs[191,197]. PEDOT has been shown to significantly reduce probe impedance without substantially increasing site geometric surface area, and can be applied using electrochemical synthesis directly onto the recording site surface[191,197–200]. PEDOT has also been shown to allow for highly reversible charge injection, and significantly increases charge storage capacity compared to uncoated surfaces[202,204,206,209–211]. Additionally, PEDOT coatings have demonstrated good electrical stability after both repeated stimulation pulsation[195,209,211,212] and chronic warm PBS bath immersion[213]. These properties have proven translatable to *in vivo* application, and studies featuring the chronic implantation of PEDOT-coated probes show that the coated probes exhibited lower impedance and improved recording characteristics when compared to uncoated controls[200,201,203,204]. The PEDOT coatings have also been shown to elicit tissue reaction comparable to bare platinum following short term (two week) implantation[207].

Despite its promise, the use of PEDOT for drug release applications has been limited compared to PPy. Abidian et al.[185] employed a different release strategy using the mechanical actuation of PEDOT nanotubes to “squeeze out” trapped drug within the tubes. Alternatively, release quantity may be increased through the synthesis of a porous or sponge-like film morphology, such as that demonstrated by our group using Ppy[214,215]. Our work takes a different approach, through the use of a multi-walled carbon nanotube (MWCNT) co-dopant[216,217] to maximize exposed polymer surface area. Benefits of this approach include the mechanical reinforcement of polymer by the carbon nanotubes (CNTs)[208] as well as the ability of the CNTs to act as a nano-reservoir of drug[218]. CNTs have been successfully integrated onto neural electrodes both alone through direct electro-deposition[219] or as a dopant within a polymer composite[205,208,220]. Our group has previously shown that doping PPy films with MWCNT allows for significantly greater drug release than from PPy alone[218]. The study presented here expands on that previous work by improving chemical and electrochemical stability through the replacement of PPy with PEDOT.

The purpose of the work presented within this chapter is to demonstrate *in vivo* the feasibility of an electro-polymerized PEDOT drug delivery system featuring a MWCNT co-dopant and to perform a short-term performance comparison of this system against implanted uncoated Pt/Ir electrodes. Our model drug for release was dexamethasone sodium phosphate, selected due to its well-characterized utility in attenuating acute-phase inflammation[127,221] as well as its anionic character, allowing it to serve as a dopant without the need for intermediate carrier molecules. Dexamethasone possesses a well-characterized ability to attenuate acute-phase CNS inflammation[127,221] and has previously been explored as a candidate molecule for conducting polymer release *in vitro* in studies that demonstrated the controllability, consistency, and yield of the release method[184,185,218]. Our work employed several methods including complex impedance spectroscopy, equivalent circuit analysis, cyclic voltammetry, neurophysiological recording, and tissue histology to demonstrate both the safety and functionality of the drug release system as well as the ability of the coated probes to record neural activity effectively.

3.2 EXPERIMENTAL

3.2.1 Carbon Nanotube Preparation

Multi-walled carbon nanotubes were purchased (OD 20-30 nm, ID 5-10 nm, length 10-30 µm, purity >95%, Cheap Tubes Inc., Brattleboro VT) and functionalized using a previously published method[218]. In summary, 200 mg of nanotubes were sonicated for two hours at ambient temperature in an acid bath consisting of 100 mL 1:3 ratio of concentrated HNO_3 and H_2SO_4 (Sigma-Aldrich Co., St. Louis MO). The solution was then gently stirred at ambient temperature for 12 hours. Treated nanotubes were collected by decantation following ultracentrifugation (16,000 RPM at 15°C for 40 minutes) and sonicated for 10 minutes in diH_2O (Milli-Q, Millipore Co., Billerica MA). Centrifugation and decantation were repeated until the pH of the supernatant was 6.0. The remaining solvent was evaporated off in an oven at 60°C.

3.2.2 In Vitro Drug Release Characterization

Gold macroelectrodes were fabricated using a custom-designed template featuring a 0.456 cm^2 electrode area. 0.51 mm thick polystyrene sheets (McMaster Carr Inc., Cleveland OH) were trimmed into 0.01 m^2 rectangular tabs and cleaned by soaking in 7.9 M nitric acid (Sigma-Aldrich) for 30 minutes at ambient temperature before being rinsed with diH_2O and dried with nitrogen gas. Custom adhesive masks were prefabricated featuring holes for circular electrode surfaces and linear contact segments, and were adhered to the polystyrene before a 40 nm gold layer was applied using a sputter coater (108auto, Cressington Scientific, Watford, UK).

Films were electropolymerized onto the gold macroelectrodes for drug release testing as follows: prepared acid-functionalized MWCNTs were dispersed and dexamethasone 21-

phosphate disodium salt (Sigma-Aldrich) was dissolved into diH_20 at a concentration of 1 mg/mL and 20 mg/mL respectively, and sonicated for one hour to facilitate drug loading and uniform dispersion of the nanotubes. Post-sonication, 6 μL of 3,4-ethylenedioxythiophene (Sigma-Aldrich) was added to the solution and triturated until dissolved. The gold macroelectrodes were then inserted into the solution and a film was electropolymerized using a three-electrode cell consisting of a platinum sheet counter and Ag/AgCl reference using a potentiostat (FAS 1 Femtostat, Gamry Instruments, Warminster PA). Polymerization was carried out at constant 1.2 V until a total charge of 46 mC was reached. Post-polymerization, the coated macroelectrodes were gently rinsed with diH_2O and soaked in a gently stirred 2 L PBS bath overnight at ambient temperature, with the bath solution being refreshed after the first hour. Macroelectrodes were stored in an ambient temperature static PBS bath until release.

Release quantification was conducted using a two electrode cell with a platinum sheet serving as the counter. Coated macroelectrodes (N=6) were individually clamped into glass cuvettes containing a 1 mL PBS bath, which was sampled for non-stimulated passive release every five minutes for 20 minutes. The concentration of dexamethasone within 100 μL samples was quantified using a plate reader (Spectramax M5, Molecular Devices, Sunnyvale CA) at a characteristic wavelength of 242 nm. Sampled solution was returned to the electrode bath after each measurement. Immediately after the passive release assessment, macroelectrodes were subjected to a stimulation routine as follows: cyclic voltammetry (20 cycles from 0.6 V to -0.9 V (vs. Pt) at 1 V/s anode-first) was applied to the electrode, and the bath was sampled and dexamethasone concentration quantified as above. Sampling was repeated once every five minutes until the concentration was found to remain stable. At this time, the 20-cycle CV stimulation pattern was applied twice, with a one minute resting period between individual sets of cycles, and the sampling routine was performed as above. This was repeated a further three times, with the number of CV stimulation patterns increasing by one with each repetition, for a total of 15 CV stimulation patterns spread between five measurement sessions. This progressive assessment routine was performed to ensure that the dexamethasone concentration increase for each session remained within the sensitivity limit of the plate reader. The entire process was repeated with a separate set of electrodes (N=3), but with a more aggressive release stimulation (10 cycles of square wave stimulation, 2.0 V for 5 s, 0.0 V for 5 s. (vs. Pt)).

3.2.3 In Vivo Array Preparation

Floating Microelectrode Arrays (FMAs, Microprobes for Life Science) were removed from their commercial packaging and sterilized using an EtO gas sterilizer (AN 74i, Andersen Products, Inc., Haw River NC) after which they were transferred to a sterile environment within a biosafety cabinet. Initial quality-control impedance testing of all array sites was performed in a sterile PBS bath using a potentiostat (Autolab PGSTAT128N with FRA2 impedance spectroscopy module and Nova 1.8 control software, Metrohm USA, Riverview FL) with a three electrode setup consisting of a platinum wire counter and an Ag/AgCl wire reference (10 Hz-30 kHz, 10 mV RMS). If recorded impedances differed substantially from manufacturer-reported impedances, the array was subjected to an electrochemical cleaning step (constant -2 V for 20s). After cleaning, the array was removed from solution and re-inserted to ensure no bubbles remained, and impedance was retaken. This cleaning process was repeated until the sites reached the impedances reported by the manufacturer. Following performance verification, each array was rinsed with diH2O and then immersed in a sterile polymerization solution prepared in the same manner as that used for the *in vitro* electrode preparation above. Using a three electrode cell, half of the array sites were coated using constant 1.3 V (vs. Ag/AgCl) for 30 seconds, selected using a staggered, alternating arrangement to prevent positional bias in the array. After coating, the array was rinsed using diH2O and impedance measurement was repeated in sterile PBS. Arrays were allowed to continue soaking in PBS for 30 minutes to remove adsorbed drug, given a final rinse using diH2O, and were then stored dry in a sterile enclosure. Immediately before implantation, arrays were exposed to a UV sterilization lamp within a sterile biosafety cabinet for 30 minutes.

Characterization was also carried out on single microwires (Pt/Ir alloy, 12 µm diameter, parylene-C insulated, 30 µm length exposed tip with ~380 μm^2 area, Microprobes for Life Science, Gaithersburg MD) identical to those of the arrays implanted *in vivo* above. Individual electrodes were coated using the same protocol as *in vivo* arrays. Impedance spectroscopy was conducted in PBS using the potentiostat in a three-point configuration (10 Hz-100 kHz, 10 mV RMS). Scanning Electron Microscopy was conducted at The University of Pittsburgh's Center for Biological Imaging on a field emission SEM (6335F, JEOL USA Inc., Peabody MA). Coating adhesion was evaluated by inserting and removing coated electrodes from Long Evans rat cortex *in vivo* or from an agarose gel using a micromanipulator. Coating integrity was evaluated using impedance spectroscopy and SEM. Agarose gel was prepared by heating a stirred 5 mg/mL agarose (Fisher Scientific, Waltham MA) solution to 85° C until clear, at which point it was allowed to cool and set.

3.2.4 Surgical Implantation

Prepared FMAs were implanted unilaterally into the right primary visual cortex, monocular area (V1M) of male Long Evans rats. Each animal was anesthetized under 3% isoflurane, weighed, and mounted onto a stereotaxic frame (Narishige USA, Inc., East Meadow NY). The skull was exposed and a 3x3 mm rectangular craniotomy centered at 6.5 mm post Bregma and 3.5 mm lateral to midline was made over V1 using a high speed drill and fine rongeurs. Saline was applied continuously onto the skull to suppress heat from the high speed drilling. The dura was resected using fine Vannas scissors, and the brain surface was moistened using gelfoam while stereotaxic hardware was put into place. Insertion of the FMA array was accomplished using a vacuum suction tip mounted to a hand-driven manipulator (SM-11, Narishige USA, East Meadow NY). The craniotomy was sealed using a low-viscosity silicone[222] (Dow Corning, Midland MI). Four skull screws were mounted around the craniotomy and a headcap was applied using UV-cured dental cement (Pentron Clinical, Orange CA) to secure the FMA connector and cable. Animal temperature was maintained throughout the procedure using a warm water pad (HTP 1500, Adroit Medical Systems, Loudon TN) and homeostasis was maintained using sterile Ringer's solution. 0.3mg/kg buprenorphine was administered twice daily for three days as a post-operative analgesic. Animals were provided with soft water-based diet gel immediately after surgery, and food and water were provided *ad libidem* for the remainder of the experiment. All animal care and procedures were performed under the approval of the University of Pittsburgh Institutional Animal Care and Use Committee and in accordance with regulations specified by the division of laboratory animal resources.

3.2.5 Treatment Schedule

Immediately after implantation and daily thereafter, animals were lightly anesthetized using 1-3% isoflurane and subjected to a stimulation and recording protocol. All coated and uncoated array sites were subjected to an identical cyclic voltammetric stimulation program each session.

Before and after this stimulation, both spontaneous and evoked neural activity was recorded and complex impedance was measured across the entire array. This protocol allows all metrics to be measured immediately before and immediately after stimulation, and tracked daily for the duration of the experiment. Each component of the session is described in detail below:

3.2.6 Drug Release Stimulation

Electrical stimulation for drug release was performed using a PGSTAT128N potentiostat connected to a 16 channel multiplexer. Sequentially on each channel, cyclic voltammetry was performed using 20 cycles from -0.9 V to 0.6 V (two point vs. Pt. counter electrode) at a 1 V/s scan rate, anode-first. Redox behavior of each site was qualitatively observed in terms of reduction and oxidation peak height and potential shift. Fast-CV cathodic charge storage capacity and charge balance were computed by integrating the area under cathodic and anodic curves. Charge storage capacity was used to compute injected cathodic charge density for each pulse.

3.2.7 Neurophysiological Recording

Recording of spontaneous and visually evoked single units, multi-unit, and LFP response was performed each session, both before and after stimulation. Spontaneous recording was conducted in a dark room. During each recording session, animals were situated on a microwaveable heating pad inside of a darkened faraday cage while lightly anesthetized with isoflurane. An LCD screen was positioned outside of the cage and the animal's head was fixed to provide for optimum viewing angle from the dominant eye. Optimum anesthetized activity levels were typically observed when isoflurane level was set at the very lowest concentration sufficient for the maintenance of animal inactivity (1.5-1.75%). Subjects were carefully observed during recording to ensure the proper plane of anesthesia was maintained. Visual stimuli were presented using the MATLAB-based Psychophysics toolbox on an LCD monitor placed 20 cm from the eye contralateral to the implant. Solid black and white bar gratings were presented drifting in a perpendicular direction and synchronized with the recording system (RX5, Tucker-Davis Technologies, Alachua FL). Each 4 second grating presentation (rotated in 45° increments) was separated by a 4 second dark screen period. Additionally, a spiraling continuous stimulation with 3°/s clockwise rotation was also presented each recording session. The raw data stream was filtered to produce LFP (1-300 Hz) and spike (0.3-3 kHz) data streams. Possible spikes were detected using a fixed negative threshold value of 3.5 SD. Offline spike sorting was carried out using a custom MATLAB script. Average SNR (averaging the amplitudes of single units for each channel), and average amplitude of noise (4 SD) was used to quantify electrode recording performance. Only channels exhibiting detected spikes were included in the SNR computation. All parameters were compared for each group before and after stimulation, as well as at each time point.

3.2.8 Impedance Spectroscopy and Equivalent Circuit Analysis

Electrochemical impedance was measured before and after each stimulation session. While under anesthesia, the implanted array was connected to the Autolab potentiostat using a 16 channel multiplexer. Impedance was measured for each channel using a 10 mV RMS sine wave from 10 Hz to 32 kHz, employing a 15 multisine paradigm to shorten the time required for measurement. MEISP (v3.0, Kumho, Seoul, South Korea) and NOVA (v1.8, Metrohm USA) were used for measurement and analyses.

3.2.9 Histology

At 11 days post-implantation, animals were sacrificed and perfused according to University of Pittsburgh IACUC approved methods. Each animal was deeply anesthetized using 65 mg/kg ketamine, 7 mg/kg xylazine cocktail. Once the proper plane of anesthesia was observed, animals were transcardially perfused using a warm PBS flush followed by ice cold 4% paraformaldehyde. Animals were decapitated, and heads were post-fixed in a 4% paraformaldehyde bath at 20°C overnight. Following post-fix, the skull was dissected and electrode arrays carefully removed to avoid incidental tissue damage. Whole brains were then removed and soaked in a 15% sucrose bath at 20°C overnight followed by a 30% sucrose bath until brains were fully impregnated. Brains were then blocked and carefully frozen using a 20% sucrose/OCT blocking media blend and dry ice. Tissue was horizontally sectioned from the surface of the cortex down, perpendicular to the axis of the probes, using a 10 μm slice thickness. Sectioning continued until approximately 200 μm below the disappearance of the probe tracks to ensure that probe tips were captured.

Tissue sections were hydrated using PBS and exposed to a 0.5 mM $CuSO_4$ solution for 10 minutes to reduce hemosiderin-dependent autofluorescence[164]. Following exposure, sections were washed with PBS (3x5min) and incubated in a blocking solution (10% goat serum, 3% triton X-100) for 1 hour at ambient temperature. Following blocking, sections were incubated in a primary antibody solution consisting of 5% goat serum, 1.5% triton X-100, and antibodies against microglia (1:200 mouse anti-OX42, Abcam) and astroglia (1:500 rabbit anti-GFAP, Dako, Glostrup, Denmark) for 18 hours at 4°C. The next day, sections were washed with PBS (3x5min) and incubated in a secondary solution consisting of 5% goat serum, 1.5% triton X-100, and antibodies (1:1000 goat anti-mouse Alexa 488, Invitrogen, and 1:1000 goat anti-rabbit Alexa

594, Invitrogen) for two hours at ambient temperature. Sections were then rinsed with PBS for 5 minutes, exposed to 1:1000 Hoechst 33342 (Invitrogen) for 10 minutes, and washed in PBS (3x5 minutes) before being coverslipped with Fluoromount-G (Southern Biotech, Birmingham AL). Sections were promptly imaged using confocal microscopy (FluoView 1000, Olympus, Inc.) at 40X magnification with electrode sites centered in the imaging field. Confocal imaging was performed in a single session using identical laser power and detector gain for each channel.

A custom MATLAB script was written to perform intensity-based radial analysis for activity dependent fluorescent markers (OX-42/GFAP). For the analysis, images were compared to control data >250 µm away from any insertion site. In order to prevent holes in the tissue (such as blood vessels and probe tracks) from artificially reducing the average activity-dependent fluorescence, background noise intensity threshold was calculated. To calculate the background noise intensity threshold, pixels with intensity greater than one standard deviation dimmer than mean pixel intensity were considered "signal" and removed from the calculation. The threshold was then determined by calculating the pixel intensity of one standard deviation below the mean of the remaining pixel intensities. After being loaded into MATLAB, the center of the probe track was identified on each image, after which the script generated masks of concentric rings every 20 µm for 240 µm. The average gray scale intensity for all pixels above the background noise intensity threshold in each 20 µm ring was calculated, normalized against the background, and plotted as a function of distance. Data were averaged for coated and uncoated locations.

3.2.10 Explant Imaging

Coating integrity of the explanted probes was evaluated using scanning electron microscopy. Following array extraction, electrodes were soaked in a 5% trypsin solution for twenty minutes at ambient temperature to remove tissue residue and fully reveal the underlying coating surface. Arrays were then rinsed with DI water and dried for high resolution SEM.

3.2.11 Statistics

Comparison between two groups was performed using a student's t-test, with $\alpha<0.01$ considered a significant result. Comparison between multiple time points in the same group was performed using ANOVA with a Tamhane T2 post-hoc test. Tamhane T2 was selected in place of Tukey due to the large difference in variances within absorption spectroscopy and *in vivo* impedance data.

3.3 RESULTS

3.3.1 In Vitro Characterization

Dexamethasone (Dex) and MWCNT-doped PEDOT coatings were characterized with regard to morphology, impedance, and drug release capacity (Fig. 3.1). Representative coated surface morphology is shown in figure 3.1a and b, demonstrating the fine, open, lattice-like morphology of the electrodeposited film. This is in contrast to typical uncoated microwires, which exhibit the coarse and irregular metal surface texture typical of arc-exposed electrode tips (Fig. 3.1c). The contrast demonstrated in the scanning electromicrographs illustrates the greatly increased surface area of the dex/MWCNT/PEDOT-coated surfaces. The impact of this increased surface area was observed using impedance measurement (Fig. 3.1d), which demonstrated that the coating significantly decreased ($p=0.0003$) the 1 kHz impedance modulus of the coated microwire tips (276 kΩ ± 147 kΩ) compared to those left uncoated (446 kΩ ± 153 kΩ) in PBS. Coating adhesion testing demonstrated no apparent changes to electrode impedance or surface morphology following insertion and removal of a coated microwire from *in vivo* rat cortex. Insertion and removal of a coated microwire from agarose gel resulted in a clinging residue of agarose to the surface visible by SEM, but no change in electrode impedance.

The controlled drug release characteristics of the coating were evaluated *in vitro* with coated gold macroelectrodes using a progressive stimulation routine. Peak stable release quantities for passive diffusion and passive diffusion plus 10 sets (20 CV cycles each) of stimulated release (N=6 for each) are shown in figure 3.1e. Passive release during 20 minutes of immersion in PBS produced a dexamethasone concentration significantly greater than PBS control (1.62 ± 0.84 $\mu g/cm^2$ based on coated electrode surface area, $p=0.001$). Total cumulative dexamethasone release following passive diffusion and 10 sets of stimulated release was found to be significantly greater (3.68 ± 1.22 $\mu g/cm^2$, $p=0.009$) than that released through passive release alone. Cumulative release from the second set of electrodes (N=3) subjected to a more aggressive release stimulation yielded a 115% increase in released drug ($p=0.009$).

3.3.2 Electrochemical Impedance

To compare the *in vivo* performance of dexamethasone/MWCNT-doped PEDOT-coated probes against conventional non-coated microwires, Long Evans rats were implanted with 16-channel floating microwire arrays unilaterally into V1 monocular cortex. The layout of the implanted arrays is illustrated (Fig. 3.2a), demonstrating the alternating staggered arrangement of the coated and uncoated probes. Comparisons between chronic *in vivo* impedance and charge storage were quantified (Fig. 3.2b-f). For all impedance and cyclic voltammetry measures, N=24 for days 0-3, but was reduced to N=16 for days 4-11, as a result of animal loss due to pneumonia.

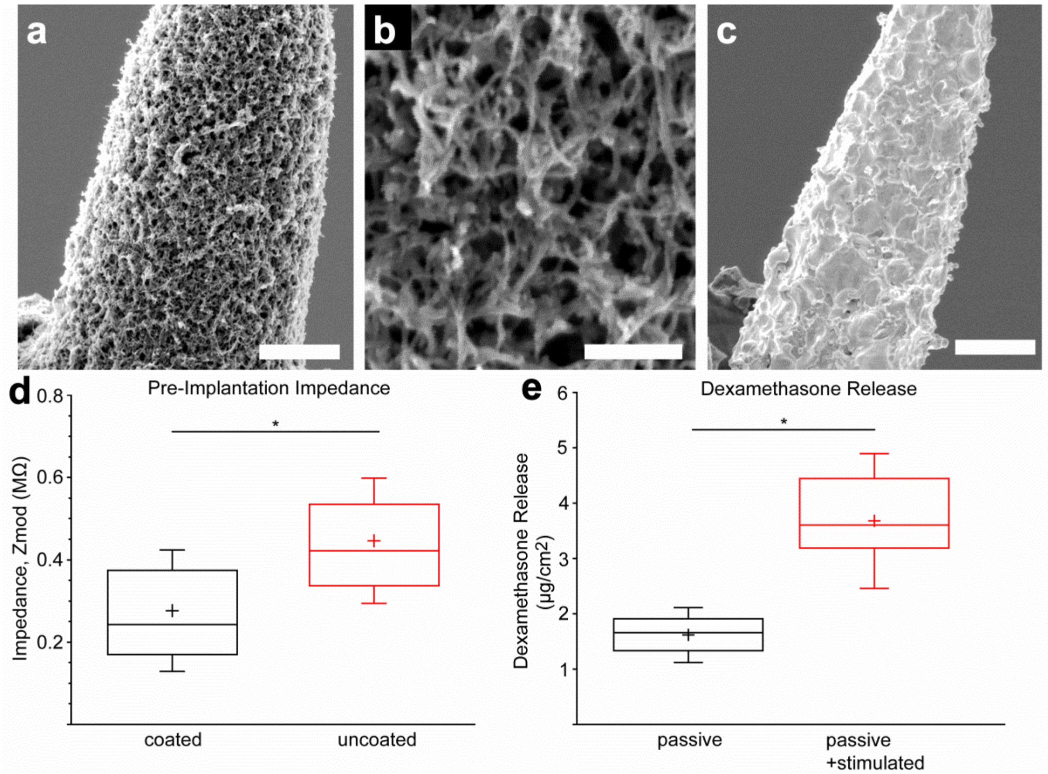

Figure 3.1: Morphology, impedance, and drug release. a-c) SEM images of (a) coated microelectrode (SB = 3 µm), (b) detail of coated microelectrode (SB = 0.5 µm), (c) uncoated microelectrode (SB = 3 µm). d) 1 kHz impedance modulus comparison between coated and uncoated electrodes before implantation. e) Cumulative dexamethasone release following passive and passive plus stimulated release from coated gold macroelectrodes into 100 µL PBS bath. (N=6, box=25-75%, cross=mean, whiskers=SD). *: $p<0.01$.

Day 0 data were collected on the same day as implantation, immediately after the surgical procedure was completed. Data for days 5, 6, and 9 are not displayed, as potentiostat failure during script execution prevented pre-stimulus data collection from at least one animal.

Average daily pre-stimulation 1 kHz impedance modulus values for coated and uncoated probes are shown (Fig. 3.2b). Impedance of the coated probes was found to be significantly lower than values observed from uncoated probes for the first three days post-implantation ($p<0.0001$ for each day). Subsequently, the impedance of coated probes increased rapidly to the point that it became indistinguishable from uncoated values for the remainder of the experiment. Dynamic impedance behavior over the first three days of the experiment is shown in detail (Fig.

3.2c), which highlights that coated probe impedance values remained significantly depressed compared to day 0 values for two days post-implantation (p=0.004 for day 0-1, p=0.007 for days 0-2), while uncoated probes on average exhibited steadily increasing impedance values. Average impedance values of coated probes were significantly lower than uncoated probes in PBS and for the first three after implantation, and also significantly decreased for two days following implantation.

Daily values for the average change in probe 1 kHz impedance measured immediately before drug release stimulation compared to those measured immediately after stimulation are shown (Fig. 3.2d). Average post-stimulation impedance values typically changed by a degree less than 10% of pre-stimulation values, with change usually trending in the negative direction. Additionally, a statistically significant difference between coated and uncoated post-stimulation 1 kHz impedance change was only observed on days 0 and 1 (p=0.002 and 0.0001, respectively).

3.3.3 Cyclic Voltammetry and Charge Storage Capacity

Electrochemical properties of the deposited films were evaluated using daily drug release cyclic voltammetry profiles. 20 cycles between -0.9 V to 0.6 V at 1 V/s were applied to each channel daily and the resulting curves were used to characterize the chronic stability and charge capacity of the films *in vivo*. Typical *in vivo* release CV curves are displayed (Fig. 3.2e) for both coated and uncoated probes, with all channels from each group averaged from one animal and one day (day 1 post-implantation) and plotted within the same figure. Coated probes exhibited a reduction peak at -700 mV, while uncoated probes exhibited no reduction behavior.

Average daily values of CV cathodic charge storage capacity (CSC_C) are shown for both coated and uncoated probes (Fig. 3.2f). As expected from the curves shown in figure 3.2e, average CSC_C of coated probes remained roughly 300% greater than uncoated probes for the duration of the experiment. The difference was found to be statistically significant at each time point ($p<0.01$ for all measurements). Maximum injected cathodic charge was estimated to be 260 $\mu C/cm^2$ for uncoated probes and 600 $\mu C/cm^2$ for coated probes (over ~1.5s) based on approximate geometrical surface area. Comparison between anodic and cathodic charge density of coated electrodes indicated charge balance of between 80% and 90% throughout the experiment, with charge surplus being in the anodic direction.

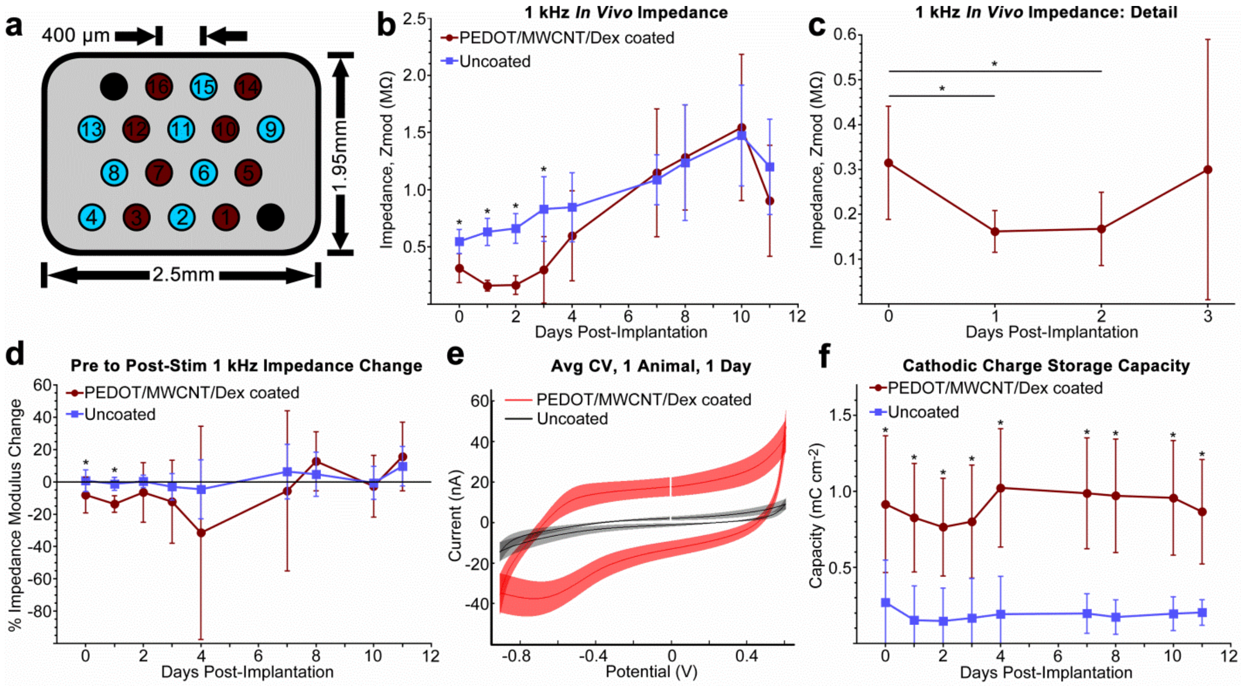

Figure 3.2: In vivo impedance and charge capacity. a) FMA layout. Red = coated, and blue = uncoated. Black sites are 2.5 mm Pt/Ir ground and reference electrodes. b) Average 1 kHz *in vivo* impedance values for uncoated and coated probes, recorded daily immediately before application of release stimulus (N=24 for days 0-3, 16 for days 4-11). c) Detail of impedance values for coated probes during initial three days of implantation (N=24). d) Average % change in post-stimulus impedance compared to pre-stimulus. e) Average CV curves collected from one animal at one day post-implant. Discontinuity indicates starting potential. f) Average cCSC computed from CV. Data presented as mean ± SD. *: $p<0.01$.

3.3.4 Neurophysiological Recording

Contralateral monocular visual stimulation provided using an LCD monitor evoked robust firing rate change during the entire period of experimentation. A representative spike data stream from a coated channel on the last day of implantation, day 11 post-implantation, is shown in figure 3.3a. The waveform, inter-spike interval histogram, and PSTH of a representative sorted single unit on this channel are presented in figure 3.3b-d. Average recording noise amplitude and SNR (signal to noise ratio) between the coated and uncoated electrodes are compared in figure 3.3e and f.

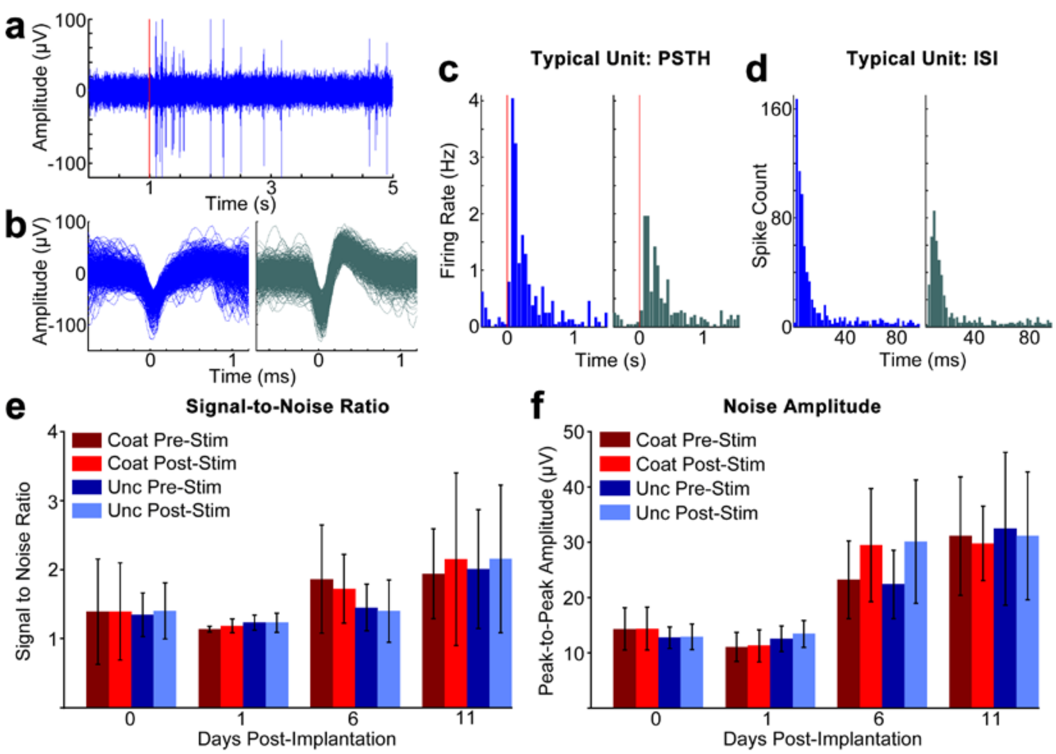

Figure 3.3: Recording performance. a-d) Representative recorded neural activity for a coated electrode at day 11 post-implant, demonstrating typical unit characteristics. a) Filtered data stream (0.3-3 kHz), with red line indicating initiation of visual stimulus. b) Two example units from the same channel. c) Peristimulus time histogram for the example units. d) Interspike intervals for the example units. e) Average SNR values on representative days for coated and uncoated channels before and after CV. f) Average noise amplitude immediately before and after CV. Data presented as mean ± SD. p>0.01 for all.

Same-day unit information is divided into groups before and after CV stimulation to evaluate the influence of stimulation on neural activity. The results suggest that the recording performance and neural activity on each electrode were not altered by the release stimulation to a degree quantifiable by the methods used. Performance was also not observed to be correlated with impedance during the initial week, as uncoated and coated probes exhibited the same noise amplitude and SNR despite having significantly different 1 kHz impedance. In general, the coated channels performed similarly in comparison with non-coated channels.

3.3.5 Histology

Representative confocal images of GFAP and OX42 expression around coated and uncoated probe tips at 11 days post-implantation are shown (Fig. 3.4a and b). Highly variable but comparable degrees of astroglial and microglial response were observed around each probe type. Average fluorescent intensity analysis performed in one animal revealed no significant difference in the expression of either GFAP or OX42 between coated and uncoated probes (Fig. 3.4c and d, coated N=8, uncoated N=6), though a large degree of variance was observed within each group. In general, microglial expression was found to be condensed and strongly activated immediately next to each probe tip, while activated astroglia were observed occupying a sparse, broad field around each probe.

Significant amounts of tissue were observed clinging to the array following pull out from the fixed brain despite thorough post-fixation and careful removal, particularly at the upper shank of the electrodes near the array substrate. In one of the two study animals that survived to experiment completion, the tissue pull-out was limited to the upper length of the electrode shanks, and the tissue at the electrode tips was left intact for preparation and imaging. However, in the second animal tissue was pulled out over the entire length of a majority of the array electrodes, making the application of our histology procedure impossible.

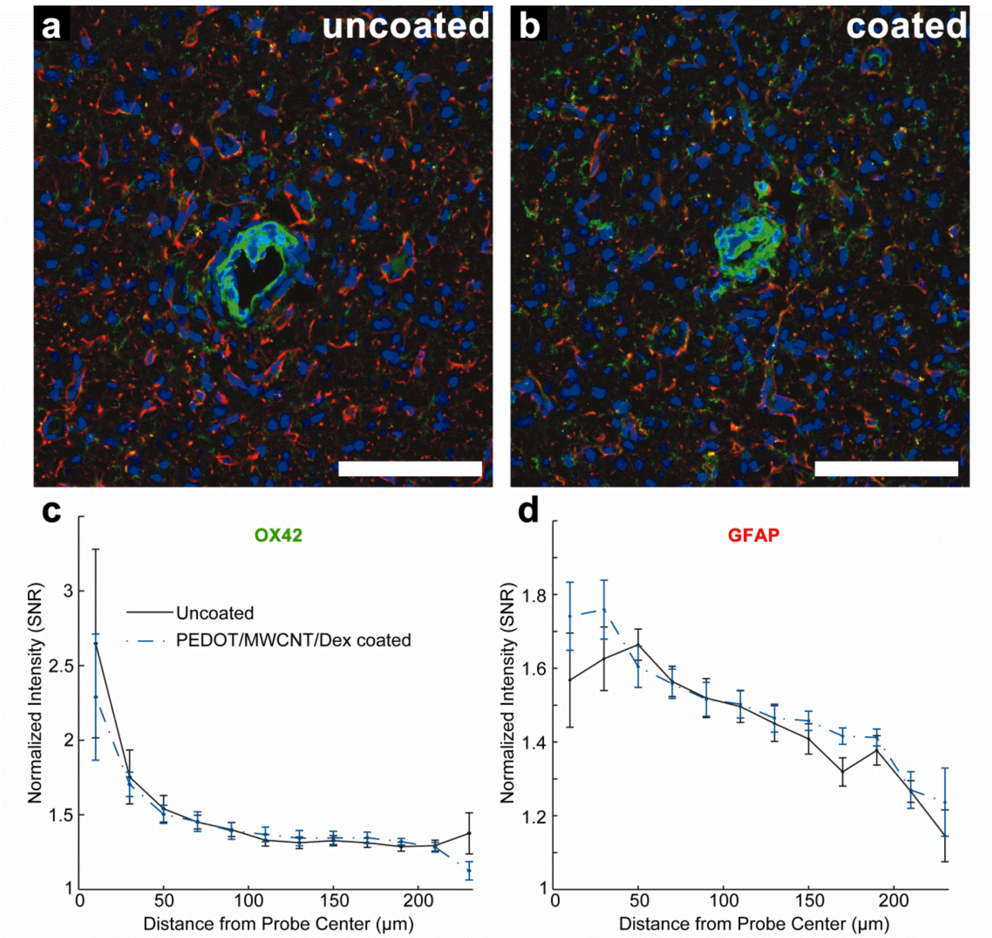

Figure 3.4: Histology. a-b) 40X confocal microscopy of tissue reaction at representative probe tips for coated and uncoated sites, at 11 days post-implant. Green = OX42 (activated microglia), red = GFAP (activated astroglia), blue = Hoechst 33342 (nuclei). SB = 100 µm. c-d) Average normalized intensity vs. distance from probe centroid for one animal. No significant differences were found between uncoated and coated probes (N=6 for uncoated, 8 for coated. Data presented as mean ± SE. $p>0.01$ for all).

3.3.6 Explant Imaging

Scanning electron microscopic images of representative explanted electrodes are shown in figure 3.5, including uncoated (Fig. 3.5a) and coated (Fig. 3.5b) examples. Uncoated explanted electrodes demonstrated dimensions and surface texture visually consistent with pre-implant micrographs. Coated explanted electrodes exhibited intact coatings with no visible cracks, spallation, or removal in over 85% of the electrodes examined. Fibrous ingrowth was also observed on the surface of the intact coated explanted electrodes, penetrating and occluding the open lattice structure of the coating. We were unable to determine the composition of this residue due to the preparatory steps performed for high resolution SEM.

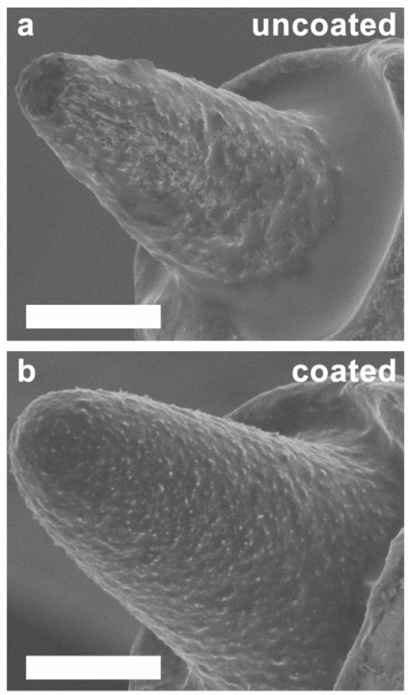

Figure 3.5: Explant imaging. SEM imaging of representative explanted uncoated (a) and coated (b) electrode tips. Tips were cleaned using trypsinization and dried before imaging. SB = 3 µm.

3.4 DISCUSSION

The goal of this study was to evaluate the *in vivo* stimulation safety and tissue reactivity of drug-releasing MWCNT-doped PEDOT coating on platinum/iridium microwire electrodes and to compare the recording performance of these electrodes against those that are uncoated. Uncoated platinum/iridium microwire electrodes served as controls for comparison of *in vivo* performance. Uncoated electrodes were employed in place of variations of coated electrodes for several reasons: 1) While it is possible to produce MWCNT-doped PEDOT coatings either without any drug co-dopant or with an alternative bioactively-inert co-dopant, such a change would substantially alter the morphological and electrochemical nature of the resultant coating. This may be observed by comparing the morphology of MWCNT and dexamethasone-doped PEDOT coatings produced here and MWCNT-doped coatings produced by Luo et al.[223] which each possess very different surface textures and feature dimensions. Such a coating would be unacceptable for use as an appropriate control, as it would introduce many confounding characteristics. 2) While uncoated platinum/iridium microelectrodes also exhibit very different electrochemical properties, their properties have been very well characterized. They also serve to represent the current state-of-the-art microwire electrode.

We demonstrated the release of dexamethasone from the coating *in vitro* using a selected stimulation method that was not observed to generate an atypical degree of tissue inflammation and was not observed to affect neural activity or recording performance. Both coated and uncoated probes exhibited a comparable degree of tissue inflammation after 11 days post-implantation. However, no evidence of dexamethasone activity was observed *in vivo*, suggesting that either the released quantities were too small or too brief to elicit a significant effect, or that the effect of release was too subtle to discern using the selected methods. While impedances of the coated probes were observed to remain within a range comparable to pre-implanted PBS measurements during the initial days post-implantation, values increased rapidly after three or four days *in vivo* and exhibited distinctive high-frequency reactance behavior in Nyquist plots, suggesting some form of probe encapsulation. Nevertheless, the recording performance of the coated electrodes was not compromised upon coating or stimulation, suggesting the safety of the technology.

3.4.1 Deposition, Morphology, and In Vitro Electrochemical Properties

Preliminary deposition testing was performed using a variety of potentiostatic and galvanostatic electropolymerization methods with final parameters being selected to maximize coating uniformity, robustness, and impedance reduction. We found that electrodeposition using constant potential produced the most consistent coatings in terms of uniformity and surface morphology on both gold macroelectrodes and Pt/Ir microelectrodes. This is in contrast with observations by Zhou et al.[205] who found that constant current polymerization resulted in better PEDOT/MWCNT films. Interestingly, our method produced the open nanofibrous lattice-like morphology exhibited in figures 3.1a and b, which is similar to the PEDOT/CNT films without Dex that we previously reported[223], while films produced by Zhou et al. exhibited a more cauliflower-like morphology[205]. A possible explanation is that our CNT size range and functionalization method may have resulted in a greater fraction of entrapped nanotubes, or a different rate of PEDOT deposition. Parameters were individually optimized for each type of electrode to provide the most similar impedance performance and morphology. A relatively high 1.3 V (vs. Ag/AgCl) was employed to coat Pt/Ir microelectrodes as lower potentials resulted in poor and inconsistent impedance reduction. Coating deposition on Pt/Ir was carried out to a charge density of approximately 0.29 C/cm^2. It was observed that careful and precise MWCNT functionalization and suspension preparation were critical to achieving consistent and robust coating deposition between samples.

SEM imaging of the dex/MWCNT/PEDOT coating revealed an open and extremely porous lattice morphology (Fig. 3.1a-b) comparable to that observed by Gerwig et al.[208] who prepared similar PSS/SWCNT/PEDOT coatings on gold MEAs. High resolution imaging at various stages of the film synthesis suggests that this morphology was achieved through the partial entrapment of CNTs within the growing PEDOT, after which the exposed lengths of the tubes were overgrown and encapsulated to form long interconnected fibrils. Progressive CNT entrapment and encapsulation continued until the coating attained the thick "bird nest" appearance visible in the SEM images. Typical fibrils possessed diameters over 70nm greater than that of the MWCNTs supporting them, suggesting the presence of a uniform and continuous encapsulating film of PEDOT. Despite the fragile appearance of the coating, preliminary qualitative testing revealed that coated electrodes were able to be inserted and removed from pia and cortical tissue with no visible change to the coating surface appearance or dimensions, indicating adequate mechanical resilience of the coating lattice and adhesion to the metal substrate. Despite the lack of covalent bonding between the PEDOT and metal, coating adherence was observed to be excellent. The high surface roughness of the substrate apparent in figure 3.1c, which resulted from the plasma arc method used by the manufacturer to expose the electrode tips, may have had a positive effect on adhesion. Adhesion may have also been enhanced by the added structural benefits provided by the MWCNT component. Comparative SEM imaging between the coating on gold macroelectrodes and on Pt/Ir microelectrode tips demonstrated no apparent difference in surface morphology or feature size.

Coated microelectrodes exhibited a significant decrease in 1 kHz impedance and an increase in cathodic charge capacity, which were observed by other studies using similar compositions[208,220]. This impedance decrease and charge capacity increase is a hallmark of conducting polymer coatings on electrodes[191,224] and is the product of multiple factors including the high conductivity of the oxidized PEDOT and MWCNT components, the large double layer capacitance produced by the greatly enhanced electrode/electrolyte interface surface area, and the charge transfer mechanisms available at the PEDOT interface due to redox activity and ion diffusion. Our coatings demonstrated a 1 kHz impedance decrease of ~40%, which was significant but was substantially less than that observed by Gerwig et al.[208] who reported reductions of over 95% following PSS/SWCNT/PEDOT coating on gold MEA sites. This contrast in performance is likely a consequence of both the poor doping capability of dexamethasone compared to PSS which led to reduced PEDOT conductivity, as well as the heightened initial uncoated impedance per unit surface area of gold planar electrode sites compared the rough Pt/Ir microwire tips.

3.4.2 Stimulated Release

A challenge faced within this study was the development of a release stimulus that would generate effective local concentrations of drug without leading to tissue damage, hydrolysis, or electrode corrosion[65,68]. The release of anionic dopant from a conducting polymer requires a negative voltage with magnitude large enough to surpass the polymer's reduction potential, with the release quantity increasing as more negative potentials and greater stimulus durations are applied[186]. While constant DC or square wave stimulus may yield good release performance, they also produce a condition of charge imbalance which may lead to both tissue injury as well as electrode instability[65]. Alternatively, sinusoidal or triangular AC waveforms limit dwell time at potentials below the reduction potential. Despite their safety advantage, the AC waveforms also increase the complexity of release dynamics due to electrostatic attraction and polymer redoping with released drug, thus reducing the effective yield. While waveforms intended for functional stimulation are typically balanced to prevent charge buildup, such balancing is difficult to achieve in waveforms intended for drug release, which are usually potential-controlled to ensure consistent reduction, and of a lower frequency to both increase dwell time below the reduction potential as well as to increase the extent of drug diffusion into tissue before the subsequent cathodic pulse.

Within this study we used a conservative stimulation paradigm, cyclic voltammetry (CV), which approximates charge balanced conditions while providing information on both redox behavior and charge storage capacity. CV has been successfully employed as a release stimulation *in vitro* in several prior studies[184,187,189] though with much slower scan rates of 20-100 mV/s compared to the 1 V/s rate used here. We considered these slow scan rates to be unfeasible *in vivo* due to the increased anesthesia time required, as well as increased unbalanced charge buildup. It is understood that despite the 80%-90% charge balance observed, significant surplus charge will still be generated, particularly if a slow scan rate is used. Also, the requirement that the stimulus pass below the -0.7 V (vs. Pt/Ir) PEDOT reduction potential for release leads to a violation of the water window[68] and the possible evolution of hydrogen gas through hydrolysis, though the maximum voltage that may be applied without creating an unsafe interfacial potential drop is difficult to predict, due to the *in vivo* environment and the potential-controlled nature of the stimulation. A fast CV scan minimizes the time spent at potentials that may result in permanent damage of the electrode tissue interface. PEDOT reduction and ion transfer were verified by way of the observation of a reduction peak during release stimulation in all coated channels daily throughout the experiment. This peak confirms that dexamethasone was released, though the duration of release could not be determined as the coating likely re-doped itself with local ionic species as the dexamethasone content was depleted. Material stability following stimulation was verified using SEM imaging of electrode surfaces, and it was found that the morphology remained visually unchanged after 200 cycles. Tissue integrity was monitored using both post-stimulation impedance measurement as well as histology, which did not reveal obvious evidence of stimulation-induced lesion or a harmful degree of gas evolution. CV scans also revealed consistent redox behavior and charge storage characteristics throughout the experiment duration. These evidences suggest that the majority of charge was transduced by way of safe, reversible mechanisms, and that the stimulus did not generate an observable degree of hydrolysis.

Despite the surface area enhancement provided by the MWCNT dopant, dexamethasone release trials using coated gold macroelectrodes revealed that stimulated-release quantities remained barely detectable using absorption spectroscopy, resulting in a significant increase only being detectable after ten cumulative stimulation sets of 20 CV cycles each (-0.9 V to 0.6 V, 1 V/s). Our observed 2.06 μg/cm^2 stimulated release quantity only represented a 31% increase over passive release. A comparable dexamethasone release study by Wadhwa et al.[184] using polypyrrole demonstrated a stimulated release of ~10 μg/cm^2 after a single set of 20 CV cycles (-0.8 V to 1.4 V, 100 mV/s). This illustrates that even with MWCNT enhancement the much lower dopant capacity of PEDOT requires a more aggressive stimulation protocol to release a drug quantity comparable to polypyrrole films. Both our coating and the coating studied by Wadhwa et al. were shown to passively release roughly equivalent amounts of dexamethasone during the same amount of time. The difference in release capacity between our earlier polypyrrole studies and the current PEDOT-based coating study may be the result of a number of factors, including the differences in film electrochemical properties and the more aggressive stimulation protocols used within earlier studies. A preliminary trial using a more aggressive release protocol (-2.0 V to 0 V 10 s square wave) yielded over double the quantity of released drug compared to the CV stimulation method used *in vivo*. However, this more aggressive method is both highly charge imbalanced and also subjects the environment to unsafe potentials for extended time periods, which would likely generate irreversible damage to both tissue and electrode. It is also worth pointing out that this study was focused on neural recording applications, which excluded stimulation parameters that may cause changes in neural activity patterns.

As our coating method produced visually identical film morphologies on both gold macroelectrodes and Pt/Ir microwire tips, we employed release quantities from macroelectrodes to estimate release from coated microwires *in vivo*. Scaling the macroelectrode release quantity by the microwire coating surface area and dividing by ten to determine release for a single set of cycles yields a daily release quantity of 0.21 µg/cm^2, which equates to an estimated average tissue dexamethasone concentration of 0.42 µM within a 500 µm radius from the implanted microwire tip. In comparison, Zhong et al.[127] observed 0.18 µg/cm^2 dexamethasone release from slow release coatings in 24 h, yielding a local concentration of 0.36 µM. As an effect on glial inflammation has been observed[225] following an introduction of dexamethasone concentrations as low as 0.2 µM *in vivo*, evidence suggests that our release method produced physiologically relevant dexamethasone concentrations in local tissue.

3.4.3 In Vivo Electrochemical Properties

The dex/MWCNT/PEDOT-coated probes demonstrated dynamic multimodal changes in *in vivo* broad-spectrum impedance over the eleven day period of implantation, which suggests a progression of changes to physiological or material factors at the tissue/coating interface. This is contrasted against the behavior of uncoated probes, which exhibited a gradual increase in 1 kHz impedance typical of chronically implanted uncoated microelectrodes during the first week post-implantation in rat cortex[10,21,203]. This distinction between the chronic impedance behavior of PEDOT-coated and uncoated implanted electrodes was first noted by Abidian et al.[203] who observed complex changes to Nyquist representations of PEDOT nanotube-coated electrode sites which were not evident in uncoated controls, and coincided with a sharp increase in 1 kHz impedance during the initial 2-week period post-implantation. This increase in 1 kHz impedance has since been observed by others studying the *in vivo* performance of PEDOT-coated electrodes[204,206]. We observed similar phenomena in our Nyquist plots, suggesting that these progressive changes to impedance behavior may be common to PEDOT-coated electrodes *in vivo*. However, while the 1 kHz impedance of PEDOT-coated sites within Abidian et al.'s work remained significantly lower than uncoated sites over the duration of the experiment, the average impedance of coated electrodes in our work increased to the point where it became statistically indistinguishable from that of uncoated electrodes within five days of implantation. This is possibly due to the contrast in initial impedances, as Abidian et al. observed a 90% reduction between day 0 PEDOT-coated and uncoated site impedances, compared to the 40% reduction seen in our own.

3.4.4 Neurophysiological Recording

For this study we elected to use the visual cortex model due to the simplicity of stimulation as well as the surgical accessibility of the cortical region, which was attractive due to the large profile of the FMA implant. The visual cortex lacks the curvature and dense surface vascularization of barrel cortex, and the comparative lack of columnar structures in rat V1[226] should conceptually lead to more uniform and homogenous neural activity across all array sites with proper stimulation. The Long Evans rat was selected as our model strain due to their excellent visual acuity[227].

Both spontaneous and evoked neural activity was recorded before and after daily release stimulation and impedance measurement. A variety of different visual stimulation programs were applied to the subject each session, though for the purposes of this study all measures were averaged together across spontaneous and evoked blocks. In order to provide an assessment of raw recording performance, metrics of signal-to-noise ratio, noise amplitude, and LFP amplitude were quantified. In general, only sparse unit activity was observed across both coated and uncoated probes over the initial week of implantation, though both coated and uncoated probes exhibited well-defined units. Activity in both coated and uncoated probes increased substantially within recordings taken during the final days of implantation, with recording quality being essentially equivalent. As probe impedance was also observed to be equivalent between coated and uncoated probes at those time periods, this result was expected. The inconsistent probe performance during the initial week post-implantation as well as the subsequent increase in performance has been observed previously[38] and is thought to correspond with the progression of acute inflammation and edema local to the implanted electrodes and the eventual stabilization of the interface tissue as it enters the chronic inflammatory stage.

3.4.5 Histology

Subjects were perfused for tissue histology at day 11 post implantation. This implantation duration was selected to allow for the observation of the transition of the interfacial inflammation as it progressed from the acute to the chronic state. While a longer experimental duration would have been preferred for the assessment of recording performance, we decided that the 11 day time point would provide a compromise between recording assessment and the potential to observe the effects of released dexamethasone within the tissue, which we expected to be most pronounced during the initial acute inflammatory response. Systemic[221] and local[127] dexamethasone introduction to chronically implanted probes has been observed to elicit a subtle effect on observed tissue inflammation, with effects diminishing for most markers after the administration of dexamethasone is ceased. Both studies reported significantly reduced astrocytic activation following dexamethasone administration, quantified using the marker GFAP. However, microglial response was observed to be less consistent, with systemic dexamethasone administration yielding either no effect or enhanced microglial activation, and local administration yielding a decrease in microglial activation that did not persist to a more chronic time point. As the quantity of introduced dexamethasone from the stimulated release of our coating was expected to be comparable to that introduced through a slow-release coating, it was thought that evidence of release may only be apparent within the initial acute time period. However, our histology revealed no significant difference between either astroglial or microglial response in the vicinity of the coated and uncoated electrode tips, suggesting that either the actual release quantity was substantially lower than that estimated from macroelectrode release, that the dexamethasone yield of the film was expended at a time point too early to produce a visible effect at day 11, or that the effect of the released drug on local tissue response was too subtle to be quantified using our methods. The similarity of the observed tissue response around coated and uncoated electrodes also suggests that the release stimulation method did not generate tissue damage, considering that the coated electrodes injected over three times the amount of charge as uncoated electrodes daily throughout the experiment. It is thus assumed that the additional charge delivered through the coated electrodes was transduced via safe mechanisms such as coating reduction and dopant release. It should be noted that this conclusion is drawn from a limited sample size, as the tissue from only one animal was available for quantification due to extensive tissue pullout in the second animal. Also limiting our histology was the fact that only a few sections were available for examination from each probe due to the very small size of the coated microwire tips, each being approximately 30 μm long.

3.4.6 Potential Applications

The observations collected here suggest that variations to this type of drug-release coating could provide the platform for the development of a variety of release systems incorporating a large assortment of bioactive agents. The coatings are simple to synthesize and can be electrochemically applied to most commercial bioelectrode designs for recording or stimulation, including both cortical and peripheral electrodes as well as cardiac pacemakers. The technology offers the ability to release discrete amounts of drug at a very fine temporal resolution on command using a safe electrical stimulus, allowing for the release of anti-inflammatory and/or neuroprotective agents upon detection of a biochemical trigger within the local tissue, or the simultaneous release of neuromodulatory agents while recording neural activity *in vivo*. These capabilities could allow this technology to substantially inform future biopotential electrode design, as they provide a simple, inexpensive, minimal-profile tool for modulating the tissue environment to a precisely controllable degree. Such designs could be used to neurochemically probe discrete neural pathways *in vivo*, or to develop the next generation of minimally-invasive cortical interface, bringing the technology closer to widespread clinical use.

3.5 CONCLUSION

We demonstrate that the dexamethasone and MWCNT-doped PEDOT coating is capable of release of drug *in vivo*, confirmed by way of the observation of coating reduction behavior during cyclic voltammetry. We further demonstrate that daily CV stimulation with parameters selected for drug release and applied to uncoated and PEDOT-coated intracortical electrodes do not generate substantial acute changes to 1 kHz impedance or local neural activity, and do not incite inflammatory tissue response at 11 days post-implantation atypical from that observed around similar unstimulated electrodes elsewhere[207]. Moreover, the acute impedance, recording performance, and degree of tissue reactivity between uncoated and coated probes was observed to be statistically indistinguishable despite the fact that release stimulus applied to coated electrodes injected approximately three to four times the quantity of charge injected by way of uncoated electrodes. However, quantities of drug released during the stimulation of PEDOT was observed to be substantially lower than that released from comparable polypyrrole coatings, even when the PEDOT effective surface area was enhanced using a MWCNT co-dopant. It is theorized that the low release is largely due to the more conservative stimulation protocol employed to limit potential tissue damage. We conclude that the PEDOT/MWCNT/dexamethasone coating remained morphologically stable for the duration of implantation and daily stimulation, as evidenced by a consistent level of charge storage capacity as well as a lack of observed physical damage in explant imaging. The release stimulation was determined to be safe on the basis of observed inflammatory tissue response as well as the lack of immediate changes to impedance and neural activity following stimulation. The coating was not observed to hinder neural recording, and performed comparably with uncoated electrodes.

3.6 ACKNOWLEDGMENTS

This work was greatly contributed to by Kasey Catt, who performed preliminary coating optimization as well as *in vitro* drug release quantification and probe electrochemical coating. Contributions were also made by Zhanhong Du and Takashi "TK" Kozai, who greatly assisted with neurophysiology recording methodology and analysis, as well as surgical guidance. Special thanks also to Takashi Kozai for his work in the development of the histology assessment script. Funding for this work was provided by the National Institute of Health R01NS062019 and by the Defense Advanced Research Projects Agency (DARPA) MTO under the auspices of Dr. Jack Judy through the Space and Naval Warfare Systems Center, Pacific Grant/Contract No. N66001-11-1-4014.

4.0 CIRCUIT MODELING OF IN VIVO DEXAMETHASONE/MWCNT/PEDOT-COATED ELECTRODES

4.1 INTRODUCTION

Electrical impedance is a measure of the restriction to the passage of current within a circuit upon the application of a voltage, and is analogous to electrical resistance applied to an alternating current. Unlike direct current resistance, impedance is represented by both a magnitude as well as a phase angle, representing the phase shift of capacitive or inductive elements within the circuit that are reactive to changing frequency. Electrical impedance spectroscopy (EIS) is a technique which allows for the measurement of changes to impedance magnitude and phase across a range of frequencies, and can be used to evaluate the electrical characteristics of an electrode/electrolyte interface. Within a properly designed electrochemical cell it is possible to isolate the impedance characteristics of a working interface from the rest of the measurement circuit, allowing for the detailed analysis of specific components within the interface such as electrode and coating capacitances, charge transfer resistances, diffusion characteristics, and others[228]. The frequency range employed is dependent on the interface features of interest (Fig. 4.1), with typical ranges being between 1 Hz and 100 kHz. For each measurement, a sinusoidal voltage or current is applied at a select frequency with magnitude small enough that a linear current-voltage response is maintained[68]. Potentiostatic EIS is typically preferred as it allows for the fine control of the current flowing through the circuit during measurement[21]. EIS has been found to be quite useful in assessing the electrochemical properties of microelectrodes, and may be safely applied *in vivo* due to the small voltage excursion magnitudes[68].

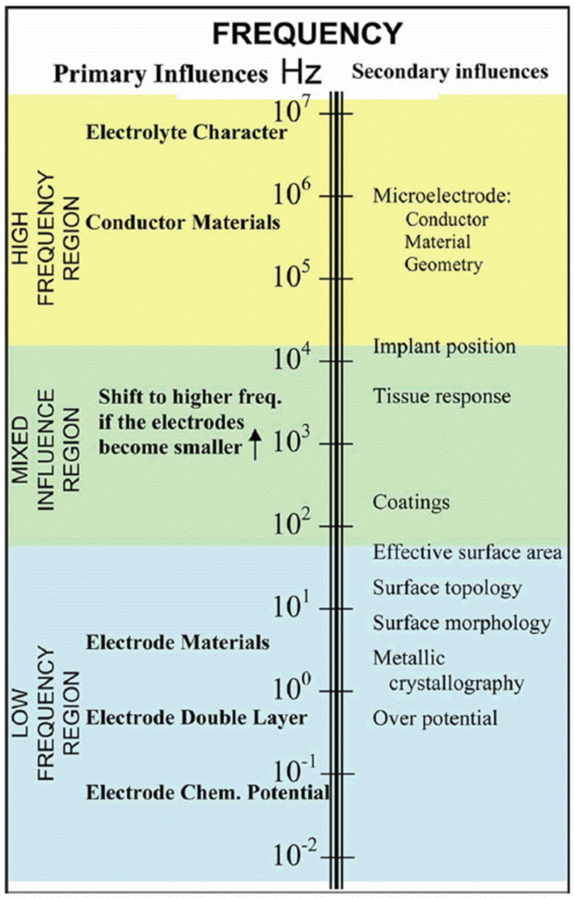

Figure 4.1: Dominant effects on bioelectrode impedance by frequency range (From Karp et al,[229] ©2007 IEEE. Reprinted with permission).

EIS has been applied to a broad range of biological tissues[230] and has been used to characterize neural recording electrode properties for over forty years[69]. In particular, impedance measurement has been used to study and quantify tissue response around chronically implanted electrodes, initially in the loins of cats[231] and later within the cortices of rats[15,21,38,41,232,233].

Williams et al. demonstrated that implanted electrode impedance is somewhat correlated with inflammatory reaction intensity[41], and Prasad et al. employed chronic impedance data to develop a predictive model for electrode failure likelihood[21]. However, the particular cellular and extracellular elements that contribute to these impedance changes are thought to be multifaceted and complex[76,234].

Early work concentrated on the increased *tortuosity* λ of astrogliotic scar, defined as $\lambda \equiv (D/D^*)^{1/2}$ where D is the diffusion coefficient of water and D^* is the diffusion coefficient of the barrier material, as determined by the diffusion of tetramethylammonium through cortical stab scar tissue[65,93]. Subsequent studies attempted to isolate the impedance contributions of various elements of the inflammatory tissue response, cellular and proteinaceous, both *in vitro*[183,229,235,236] and *in vivo*[76,234]. A principal tool of many of these studies is the *equivalent circuit model*, or a mathematical representation of the electrode/environment interface as a circuit composed of various elements selected to approximate the behavior of the known components of the interface (Fig. 4.2). Such elements may include capacitors to represent double-layer interfaces and resistors to represent charge-transfer resistances or bulk electrolyte conductivity.

A large assortment of equivalent circuit models have been developed with varying degrees of sophistication, intended to represent electrode interfaces of complexity ranging from simple bare metal electrodes in saline, to coated electrodes surrounded by reactive tissue *in vivo* (A review by L. A. Geddes discusses the historical development of equivalent circuits as far back as the late 1800s[237]). A sampling of different interfacial equivalent circuits employed by microelectrode implantation and coating studies is shown in figure 4.3. Circuits are typically selected to balance fit quality against parameter ambiguity, as simple circuits may not be able to fit complex spectra effectively, while overly sophisticated circuits may not fit individual elements with confidence due to overlap. Another important consideration during model selection is the frequency range available for fitting, as many interfacial impedance mechanisms will only dominate within specific domains.

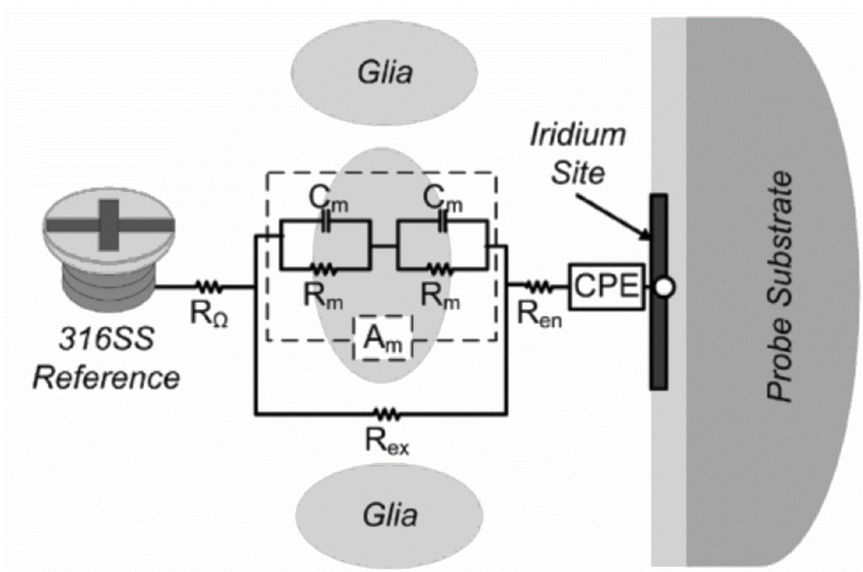

Figure 4.2: An example equivalent circuit, the "lumped element" model. Note representations of electrode surface, glial membrane, and extracellular space. A_m is a scaling factor for glial density. CPE is a constant phase element. (From Johnson et al,[232] ©2005 IEEE. Reprinted with permission).

Figure 4.2 and many models within figure 4.3 incorporate an element known as the constant phase element (CPE)[238,239]. The CPE is a mathematical entity defined as:

$$Z_{CPE} = \frac{1}{(j\omega)^{\alpha} Q} \tag{4.1}$$

where ω is angular frequency in rad/s, α is a dimensionless CPE exponential term from 0 to 1, and Q is the CPE coefficient with units $s^{\alpha}/\Omega cm^2$. The CPE was developed to model data with behavior suggesting a non-ideal capacitor, with α representing the deviation of phase angle (with $\alpha = 1$ representing a phase angle of 90° and thus ideal capacitive behavior, and $\alpha = 0.5$

representing phase angle 45° and thus 50% resistive character. As many real systems exhibit peak phase angles well below 90°, the CPE is able to fit this data much more effectively than an ideal capacitor[240]. While the physical and electrochemical factors that cause this non-idea behavior are not well understood, evidence suggests them to be a combination of surface roughness and inhomogeneity, porosity, and non-uniform current distribution over the electrode surface, as reviewed by Jorcin et al. in 2006[240].

The simplest circuit representation of the interface between a metal electrode and electrolyte is that of a capacitor in series with a resistor. This capacitor is typically known as the double layer capacitance, as discussed in chapter 1.2, and is a consequence of charge buildup within the electrolyte local to the electrode surface. This simple series circuit model is generally only appropriate for representing a theoretical "perfectly blocking" interface, and offers no leakage current route bypassing the capacitor. As no faradaic current mechanism is included, the model will act as an open circuit in DC conditions. Substituting a CPE for the capacitor within this model (Fig. 4.3a) provides more flexibility, and may be applied to systems demonstrating linear and constant phase behavior, such as blocking metal electrode systems in electrolyte at intermediate (100 Hz to 10 kHz) frequency ranges where diffusion limitations to ionic motion do not play a role[241]. This model was originally developed by Warburg in 1899[237], who limited α to 0.5 (Subsequently, a CPE with phase angle 45° is commonly known as a *Warburg impedance element*). In 1932, Fricke adapted this model by recognizing that α can be observed to vary substantially from 0.5 depending on the metal employed[237].

Placing a resistor in parallel with the CPE of the Fricke model provides a leakage current pathway bypassing the double-layer capacitance (Fig. 4.3b), and represents the resistance to charge transfer across the interface in DC conditions. This resistance is a summation of three different mechanisms (Fig. 4.3c) as discussed by Dymond in 1976[242], where R_T is the resistance to faradaic charge transfer, Z_D is the impedance to ionic diffusion at the interface (which can play a role in faradaic reaction mechanisms with rapid kinetics), and Z_R is the reaction impedance, which represents the contribution of slow rate-limiting steps of the faradaic reaction. Note that Z_D and Z_R are frequency dependent. This parallel capacitance/resistance element is commonly known as a Randles element, and it serves as the conceptual foundation for many more sophisticated models[237].

Both the Fricke and Randles elements are commonly modified through the incorporation of a diffusion impedance element to account for mass transport (Fig. 4.3d and e, respectively). This is often represented by a Warburg element, though the Warburg element is occasionally modified to allow deviation from 45° constant phase behavior at certain frequency ranges, as discussed by Bobacka et al.[243] and Gerwig et al.[208]. This diffusion impedance typically only dominates at very low frequencies where capacitive transduction is not available, and thus may be ignored at the more intermediate ranges (>1 Hz) typically employed in *in vivo* measurement[244].

Figure 4.3f demonstrates a more sophisticated model featuring two independent capacitive interfaces, represented by two Randles elements in serial (with one incorporating a diffusion impedance element). Models such as this are typically used in the case of encapsulating barriers surrounding an inner electrode, where current must cross one interface and then the other[245]. Models shown in figures 4.3g and h take a different approach and feature nested Randles elements, often used in evaluation of thin film coatings where current is not forced to traverse both capacitive boundaries, with charge instead building up on either the coating surface or the inner electrode surface following the traversal of a pore resistance (R_l or R_{Pore} within the figures). Another alternative is the "lumped element" model shown in figure 4.2, which attempts to model the interface based on known electrophysiological parameters such as cell membrane capacitance, amplified using a scaling factor to represent cellular density[41]. Note that each model incorporates a serial resistive element, typically R_S, which represents the bulk resistance of the electrolyte. Measurements have shown that bulk cortical tissue acts as a pure ohmic medium and does not exhibit frequency-filtering characteristics, allowing it to be modeled as a single resistor[246].

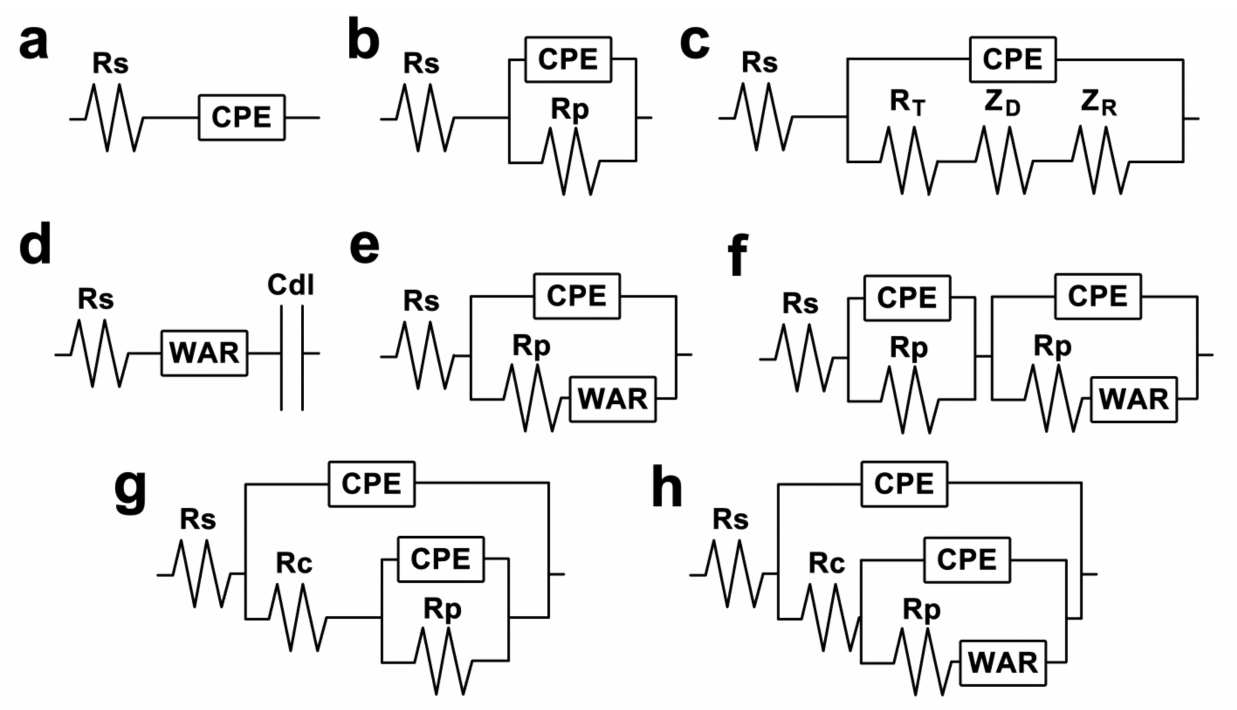

Figure 4.3: Example equivalent circuits used in microelectrode characterization. a) Fricke model[241]. b) Randles model[241]. c) Randles model demonstrating faradaic impedance components. R_T = charge transfer resistance, Z_D = diffusion impedance, Z_R = reaction impedance[242]. d) Fricke model with diffusion impedance[243]. e) Randles element with diffusion impedance[208]. f) Double serial Randles model with diffusion impedance element on the inner interface[245]. g) Nested Randles element for thin film coatings[247]. h) Nested Randles element with diffusion impedance element within inner interface[202].

Impedance data shown in this chapter will be presented in Nyquist plots. Nyquist plots, also known as Cole-Cole plots, are used to exhibit data on a complex impedance plane, with the abscissa representing the real component of impedance, or the resistance, and the ordinate representing the imaginary component of impedance, or the reactance. Each point in the plot is representative of a single frequency of measured data, with the resistance and reactance at that point indicative of the degree the impedance modulus is dominated by the resistive or the capacitive elements of the interface. An example Nyquist plot is shown in figure 4.4, and demonstrates the anticipated plot shapes of various interfacial components, including tissue and electrode as well as a combined plot similar to what would be observed in typical *in vivo* measurement from 100 Hz to 10 kHz (high frequency points being at the lower left within the plot). Note the linear appearance of the electrode plot, indicating simple CPE behavior. Tissue response typically exhibits itself as a bump of increased reactance at high frequencies, representing a second capacitive interface with its own associated time constant[41].

This dissertation chapter describes the adaptation of an equivalent circuit model to better interpret the chronic *in vivo* impedance data collected from bare Pt/Ir and dexamethasone/MWCNT/PEDOT-coated electrodes in chapter 3 of this dissertation. A number of simple models were initially evaluated and found to result in poor fitting performance. Instead, we looked to an alternative model, henceforth referred to as the *Bisquert* model. The Bisquert model was first described by Bisquert et al. in 2000[248] as an improvement over existing dual-channel transmission line interface models, and incorporated the means to evaluate microscopic dispersive processes across porous surfaces. The use of transmission line theory in place of discrete circuit elements allows the model to evaluate distributed properties across defined diffusion lengths. The model was initially employed to study TiO_2 nanoporous film electrodes[249] and later thiophene-based conducting polymers[248]. It has since been adopted within several microelectrode studies, including the evaluation of impedance changes of implanted cochlear electrodes[250], and the impedance properties of SWCNT-doped polypyrrole[220] and MWCNT-doped PEDOT *in vitro*[205].

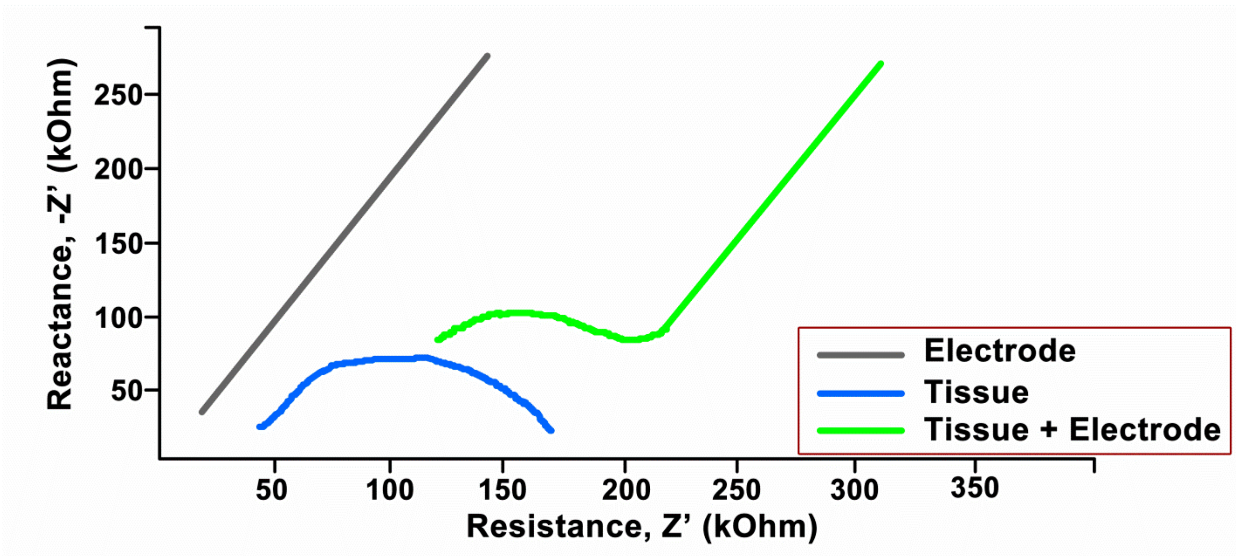

Figure 4.4: Illustration of Nyquist plots of electrode and tissue behavior.

4.2 METHODS

4.2.1 Model Derivation

An in-depth treatment of the derivation of the Bisquert model can be found in Bisquert et al. (2000)[248], and is summarized here. As stated above, this model is a dual-channel transmission line model which simplifies the complex interfacial characteristics into a superposition of "conducting solid" and "electrolyte" continua. Through this simplification, the current flux between the solid and solution phases are explored. Similar to the Randles model above, the two principle mechanisms which enable this flux coupling are electrochemical charge-transfer processes and conducting solid polarization due to interfacial charge buildup. However, due to the electrochemical complexity of the conducting polymer, it is theorized that a model incorporating spatially distributed processes will provide more realistic information than a model featuring a simple macroscopic non-distributed resistance such as the Randles circuit. A general expression of the impedance of a dual-channel transmission line is given by:

$$Z = \frac{\chi_L \chi_S}{\chi_L + \chi_S}\left(L + \frac{2\lambda}{\sinh\left({}^{L}/_{\lambda}\right)}\right) + \lambda \frac{\chi_L^2 + \chi_S^2}{\chi_L + \chi_S}\coth\left({}^{L}/_{\lambda}\right) \tag{4.2}$$

where L is the layer thickness and $\lambda = [\zeta/(\chi_L + \chi_S)]$. The elements χ_L and χ_S represent the impedance per unit length (Ω m^{-1}) of the solid and liquid phases respectively, and are typically dominated by either conductivity or mass transport properties within the medium. The element ζ represents the impedance per unit length of the exchange of charge at the solid/liquid interface, and in effect is a summation of capacitive and faradaic mechanisms at that interface.

Bisquert et al.[248] optimized this general transmission line model for conducting polymer coating applications through a number of key simplifications and assumptions. In theory, the general model may be adapted to a wide variety of interfacial conditions through modifications to the element ζ. For example, in the case of a perfectly polarizing interface between the solid and liquid phases, ζ would be represented as the impedance of an ideal capacitor, or:

$$\zeta = \frac{1}{jC\omega} \tag{4.3}$$

where C is interfacial capacitance and ω is angular frequency. In place of this, Bisquert modeled the interface as a non-ideal capacitor (represented as a CPE) and a charge transfer resistance:

$$\zeta = \frac{r_0}{1 + r_0 q_0 (j\omega)^{\beta}} \tag{4.4}$$

where r_0 is the charge transfer resistance per unit length, q_0 is the CPE capacitance coefficient, and β is the CPE exponential factor. This adaptation allows for the evaluation of a number of key charge exchange mechanisms[248].

To greatly simplify the mathematics of the model, Bisquert et al.[248] assumed the resistivity of the solid phase to be minimal compared to the contributions of the other interfacial components and set χ_S to be 0, essentially eliminating the first half of the general model. This assumption requires both that the conducting polymer remain in a highly conductive oxidized state, and that this conductivity be uniform throughout the thickness of the coating. While this assumption is justifiable in the case of conducting polymer coatings, it may not carry over to other types of conducting solids as effectively, such as glial scar tissue. In addition, Bisquert et al.[248] simplified the expression of ionic transport resistance within the fluid phase to be uniform and ohmic, represented as $\chi_L = r_L$. For fitting purposes, L is set equal to 1.

With these assumptions and the new definition of ζ taken into account, the general expression (4.2) is transformed into a more specific expression of interfacial impedance, or:

$$Z = \left[\frac{R_L R_0}{1 + \left({}^{j\omega}/_{\omega_0}\right)^{\beta}}\right]^{1/2} \coth\left(\left({}^{\omega_0}/_{\omega_L}\right)^{1/2}\left[1 + \left({}^{j\omega}/_{\omega_0}\right)^{\beta}\right]^{1/2}\right) \tag{4.5}$$

where ω is angular frequency, R_L and R_0 are the total liquid phase and charge transfer resistance values across the coating thickness ($R_L = r_L L$ and $R_0 = r_0/L$), and ω_0 and ω_L are the characteristic frequencies of the charge transfer process and of the ionic diffusion through the layer, defined as:

$$\omega_0 = \frac{1}{(r_0 q_0)^{1/\beta}} = \frac{1}{(R_0 Q_0)^{1/\beta}} \tag{4.6}$$

$$\omega_L = \frac{1}{(r_L q_0 L^2)^{1/\beta}} = \frac{1}{(R_L Q_0)^{1/\beta}} \tag{4.7}$$

where Q_0 is the total CPE coefficient across the coating thickness ($Q_0 = q_0 L$) with units F $s^{\beta-1}$. While (4.5) is a simplified expression intended purely to explore the charge exchange dynamics of the interface, most of the weaknesses of the model, including the simplification of faradaic processes and DC behavior at the metal interface as well as the assumption of fluid phase resistive uniformity, may be neglected at intermediate frequency ranges[248]. A diagram of the Bisquert model and representative complex plots are shown in figure 4.5.

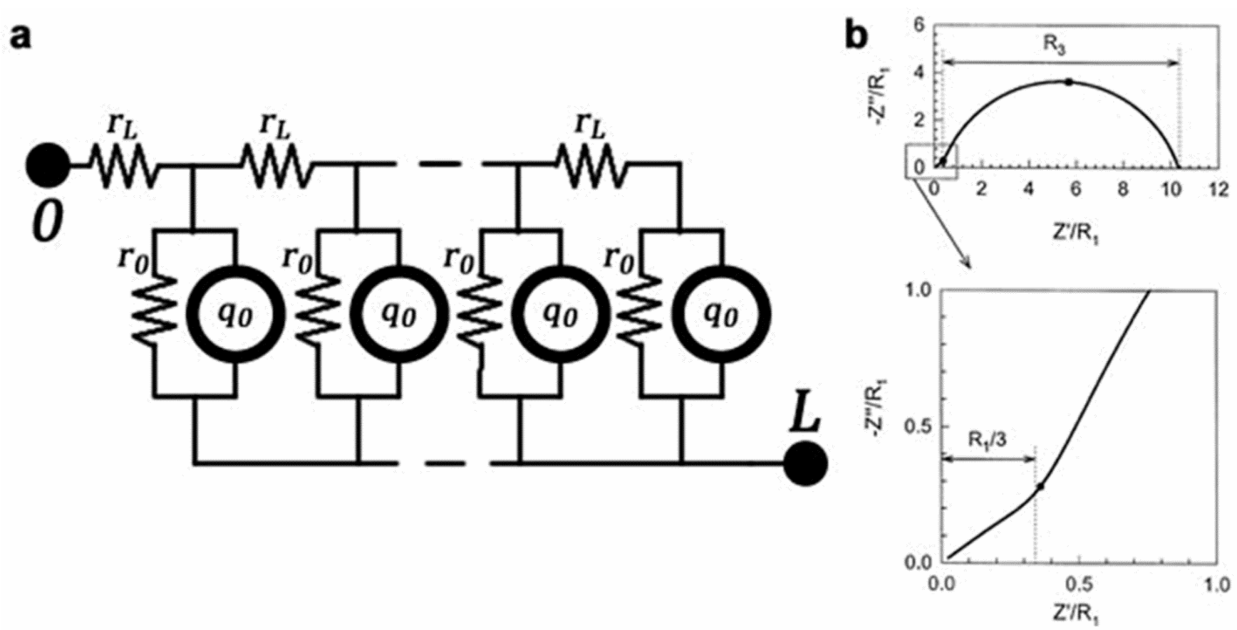

Figure 4.5: The Bisquert diffusion impedance model. a) Diagram of the transmission line representation. b) Example complex plots demonstrating model behavior in Nyquist space. R_3 curve represents charge transfer resistance. (Plots from Bisquert et al.[248] © Elsevier, Reprinted with permission).

4.2.2 Data Fitting

The Bisquert model was selected to serve as a combination representation of the dex/MWCNT/PEDOT conducting polymer coating as well as the surrounding tissue response, as a component of a wider model including metal electrode and electrolyte parameters. This model (Model A) is shown in figure 4.6a, with Z_D representing the Bisquert impedance, C_{CPE} representing the metal surface CPE coefficient, α representing the exponential term of C_{CPE}, R_{CT} representing the charge transfer resistance of the metal interface, and R_{SER} representing the serial resistance of the bulk electrolyte/brain. A second model, Model B (fig. 4.6b), is identical to Model A only lacking the Bisquert impedance, and is intended for uncoated electrodes in PBS or at early time points *in vivo* when a diffusion barrier is not observed within the data.

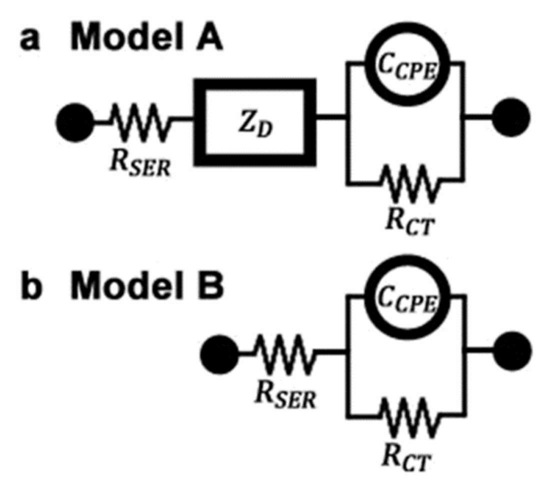

Figure 4.6: Equivalent circuit models used within this study.

Each model was mathematically expressed within a complex non-linear least-squares fitting program (MEISP v3.0, Kumho, Seoul, South Korea). Impedance data from daily *in vivo* measurement (as described in chapter 3.2.8) was loaded into the program. Before fitting, the thirteen lowest frequency impedance measurements from each impedance spectrum were removed to eliminate scatter due to low-frequency noise, which was found to be a consequence of the multisine measurement method. Also, impedance spectra that were found to contain enough broadband noise or measurement artifact to interfere with consistent fitting were removed. Fitting was typically performed in stages, with an initial fit performed across all data sets to observe general trends and identify outliers, and subsequent fits performed employing optimized seed values to increase consistency between points.

4.2.3 In Vitro Array Impedance Fitting

To compare and contrast against the *in vivo* data collected in the previous chapter, impedance measurement was performed from identical electrodes immersed continuously in a PBS bath and then fit to the model described in section 4.2.2 above. Ten parylene-C insulated Pt/Ir microelectrodes (Microprobes for Life Science) identical in nature and impedance range to those within the *in vivo*-implanted FMAs were coated with MWCNT and dexamethasone-doped PEDOT in an identical manner to that employed in section 3.2.3. Impedance was measured before and after the coating process using the method described in section 3.2.3. Following coating, electrodes were soaked in PBS overnight to wash off residual monomer, and then mounted within a sealed chamber which continuously immersed the electrode tips in an ambient temperature PBS bath while simultaneously allowing their connection to a potentiostat. Once daily, 5 of the 10 electrodes were subjected to the same impedance measurement-CV stimulation-impedance measurement protocol that was applied to the *in vivo* FMAs described in section 3.2.8. The other 5 electrodes only received daily impedance measurement with no CV stimulation. Measurement continued for 11 days, mimicking the *in vivo* experimental protocol.

Collected data were fit using model A described in 4.2.2 above, using the Bisquert diffusion impedance element.

4.3 RESULTS AND DISCUSSION

4.3.1 Complex Impedance Characteristics

Representative Nyquist plots of recorded impedance data from both uncoated and dex/MWCNT/PEDOT-coated electrodes at various time points are shown in figure 4.7. Very different features are exhibited by each, in particular on days 7 and 10 when 1 kHz impedance was statistically identical. The contrast between uncoated and coated probes on day 1 post-implantation is evident, with coated probes exhibiting reactance values over an order of magnitude lower than uncoated probes, suggesting a greatly increased CPE coefficient and thus greatly increased electrode surface area. Also evident in the day 1 Nyquist plot of the coated probe is a small high-frequency encapsulation element, likely due to the presence of the coating. Uncoated probes exhibit subtle changes to plot slope, curvature, and high-frequency diffusion behavior, suggesting that the impedance changes are the result of small changes to the electrode surface area, roughness, current uniformity, and ionic diffusion due to the surrounding tissue response. In contrast, coated probes exhibit the development of a large high-frequency encapsulation element that soon dominates impedance behavior over the majority of frequency points. Equivalent circuit analysis was applied to this data, in an attempt to tease out the specific physical and physiological correlates to best determine the root of these changes in electrical behavior.

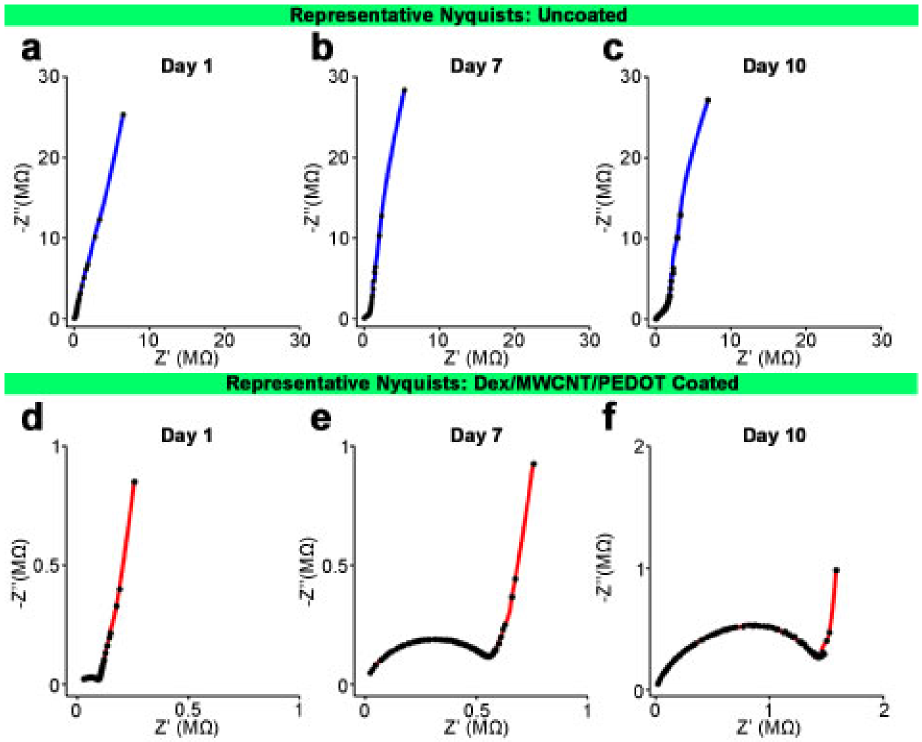

Figure 4.7: Nyquist plots of in vivo data. Representative uncoated (a-c) and coated (d-f) electrode impedance behavior. Black points are individual measured frequencies, with colored lines added for visibility.

4.3.2 Equivalent Circuit Fitting

Multiple trends were observed in the fitted model parameters, as shown in figure 4.8. Confidence in the modeled values is to a large part determined by the range of frequencies available for fitting, which in this study was limited to minimize the time required for measurement due to animal safety concerns. Parameters that are not well represented within the measured frequency range may vary substantially without changing the quality of the overall fit. The model parameter representing platinum charge transfer resistance, R_{CT}, is an example, as it is most relevant to frequencies much lower than those measured here (f < 1 Hz). Parameters demonstrating the most dynamic and consistent behavior in coated electrodes were found to be C_{CPE} and Q_0, representing the core electrode and coating or tissue encapsulation surface capacitance coefficients respectively. Their behavior compared to the same parameters modeled from uncoated electrode data is shown in figures 4.8a and b. The CPE phase angle parameter of C_{CPE} (β) also demonstrated dynamic change in the coated electrodes but remained at consistent elevated values in uncoated electrodes, as shown in figure 4.8c, while the CPE parameter of Q_0 (α) maintained a high value of between 0.85 and 1 for the duration of the experiment for both coated and uncoated electrodes. Pore fluid transport resistance R_L and conducting polymer charge transfer resistance R_0 of coated electrodes demonstrated a small degree of variation over time that did not correlate with electrode impedance modulus. The solution resistance R_{SER} was found to be inconsequentially small compared to other elements and did not contribute substantially to quality of fits when varied manually.

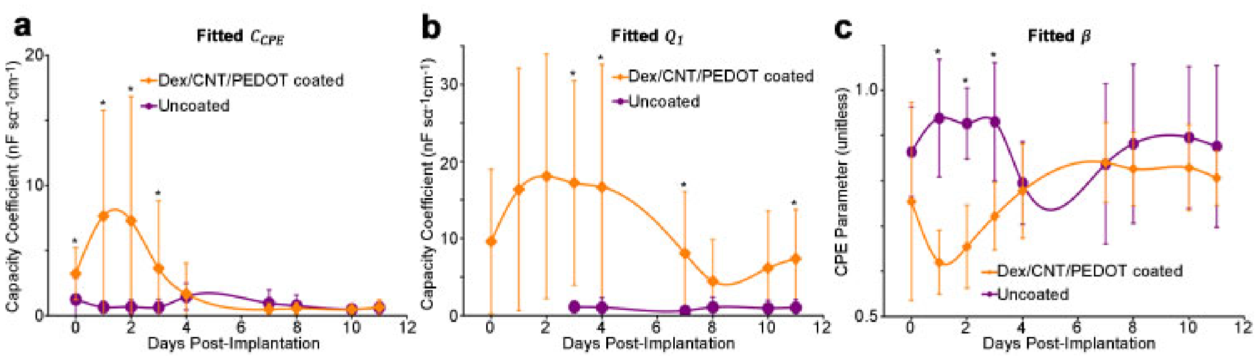

Figure 4.8: Fitted model parameters. Average fitted values of modeling parameters C_{CPE} (a), Q_L (b), and β (c). Q_L was not fitted for days 0-2 for uncoated probes due to use of model B. N varied between sessions due to measurement exclusion due to noise or artifact. Data presented as mean ± SD. *: p<0.01.

Nyquist plots collected from dex/MWCNT/PEDOT electrodes in PBS before implantation reveal the characteristic bimodal frequency response typically observed in conducting-polymer-coated electrodes, with low frequency behavior dominated by metal interface parameters C_{CPE}, R_{CT}, and β, and high frequency behavior characterized by an encapsulation element modeled using Z_D. This is contrasted against Nyquist plots of uncoated electrodes in PBS, which in the measured frequency range (10 Hz to 32 kHz) demonstrate nearly linear constant-phase behavior characterized by C_{CPE}, R_{CT}, and β. The reduction in 1 kHz impedance between coated and uncoated probes *in vitro* most strongly correlates with C_{CPE}, suggesting that the principal benefit of the coating is that of greatly increasing the effective surface area of the interfacial double-layer capacitance. However, the physical presence of the coating also seems to contribute a diffusion barrier to the interface which is most apparent in the high frequency regime. It should be noted that within the frequency range measured, the ability of fitting techniques to distinguish between R_{CT} and β is limited, particularly *in vivo* where substantial low frequency noise is often encountered during impedance measurement. This is particularly true when R_{CT} is very large, as within the arc of visible data points the data will appear essentially linear.

The gradual increase of average *in vivo* 1 kHz impedance of uncoated electrodes is typically characterized by subtle changes in metal interface parameters R_{CT} and β which dominate low-frequency behavior, as well as with a gradually emerging high-frequency diffusion barrier and encapsulation element modeled using the diffusion element Z_D. These changes coincide with known physiological events thought to play a role in evolving electrode *in vivo* impedance, with R_{CT} and β representing changes to electrode surface properties due to protein adsorption, which takes place immediately upon implantation, and Z_D representing the growing boundary effect of local tissue changes including inflammation, microglial encapsulation, and edema[13,40,97]. Chronic *in vivo* studies using uncoated microelectrodes have shown that during chronic implant durations the 1 kHz impedance tends to peak at 9-15 days and then reduces to an intermediate magnitude where it typically remains at a fluctuating plateau for the experiment duration. This is thought to correspond with the reduction of initial acute inflammation and tissue swelling, and the transformation of the interface to a stable chronic inflammatory state[21,203]. Extended chronic impedance behavior was not observable in our data, as we elected to end the experiment after 11 days of implantation in order to best observe the impact of the release stimulation on acute inflammation using tissue histology.

In contrast to the behavior of uncoated electrodes, the dex/MWCNT/PEDOT electrodes typically demonstrated an initial low-impedance period followed several days later by a rapid increase consistent between all coated electrodes. During the initial 3-4 day period post-implantation the coated electrodes exhibited 1 kHz impedances comparable with pre-implantation values, with day 1 and 2 values being additionally depressed from values measured on day 0. Fitted model parameters C_{CPE} and Q_L correlate with this depression when averaged, suggesting that the coating required a one day “maturation” period to achieve its full surface area capacitance benefit. This is possibly due to the time required for electrolyte to fully penetrate the pores of the coating, or for the fluid and tissue around the probes to stabilize post-implantation. Between day 3 and day 5 post-implantation, the average 1 kHz impedance of coated probes increased substantially to the point of equivalence with that of uncoated probes. Nyquist plots reveal that this increase is distinctive from the increase observed in uncoated probes, and appears principally due to large decreases in parameters C_{CPE} and Q_L which allowed the encapsulation element Z_D to dominate greater and greater portions of the measured frequency range. These modeling results suggest that beginning at day 3-5, the surface area enhancing benefit of the coating was sharply reduced and that a barrier composed of some combination of the coating and inflammatory tissue elements began to dominate electrode impedance behavior by way of reducing the exposed surface area and thus the capacitance of the conducting polymer. This hypothesis is supported by explant SEM imaging which revealed the presence of a dense membranous substance enveloping and interpenetrating the coating pores of all coated electrodes. Due to explant preparation for imaging, this substance was compromised before identification could be performed, but it is speculated to be a combination of fibroblasts, dense ECM, and glia. Despite this chronic impedance behavior, the recording performance of the coated electrodes did not appear to be detrimentally affected and histology did not reveal an atypical degree of tissue inflammation, suggesting that the encapsulation element is limited to the area immediately surrounding and within the coating. Another possible mechanism behind the observed behavior is the possible partial delamination of the coating from the electrode metal, which would detract from the coating surface area benefit to the electrode while generating a large ionic barrier in the form of the detached coating.

It should be noted that we employed the transmission-line linear diffusion element Z_D to model both the encapsulation component of the conducting polymer coating as well as the ionic diffusion barrier of tissue inflammatory response. Z_D has been used to model each of these elements separately in other studies[205,220,250]. We speculate that in most circumstances it is unlikely that the impedance contribution of each can be confidently differentiated using measurement and circuit modeling alone, particularly if both coating and tissue encapsulation exhibit similar time constants.

4.3.3 In Vitro Electrode Impedance Fitting

To better understand the impedance behavior observed *in vivo*, identically coated electrodes were situated within a sealed chamber and chronically immersed in PBS while being subjected to the same stimulation protocol applied to the implanted FMAs. This setup serves to remove the contribution of inflammatory tissue response and isolate the impact of release stimulation on the impedance characteristics of the coating. Half of the electrodes were subjected to the daily impedance measurement-CV stimulation-impedance measurement applied to the *in vivo* arrays, while half of the electrodes were only subjected to daily impedance measurement without stimulation. Average measured 1 kHz impedances for each group are shown in figure 4.9a, which bears a striking resemblance to the chronic behavior observed from coated electrodes *in vivo* in figure 3.2b. Upon closer examination of the data, the dynamic impedance changes were mostly due to the contribution of three of the five stimulated electrodes in particular, while the remaining two exhibited very consistent impedances over the duration of the experiment. To better evaluate the difference between these consistent ("good") and inconsistent ("poor")-performing stimulated electrodes, for the remainder of the evaluation all electrodes were grouped by performance: Non-stimulated (N=5), Stimulated "Good" (N=2), and Stimulated "Poor" (N=3). The average 1 kHz impedances for each of these three groups are shown in figure 4.9b.

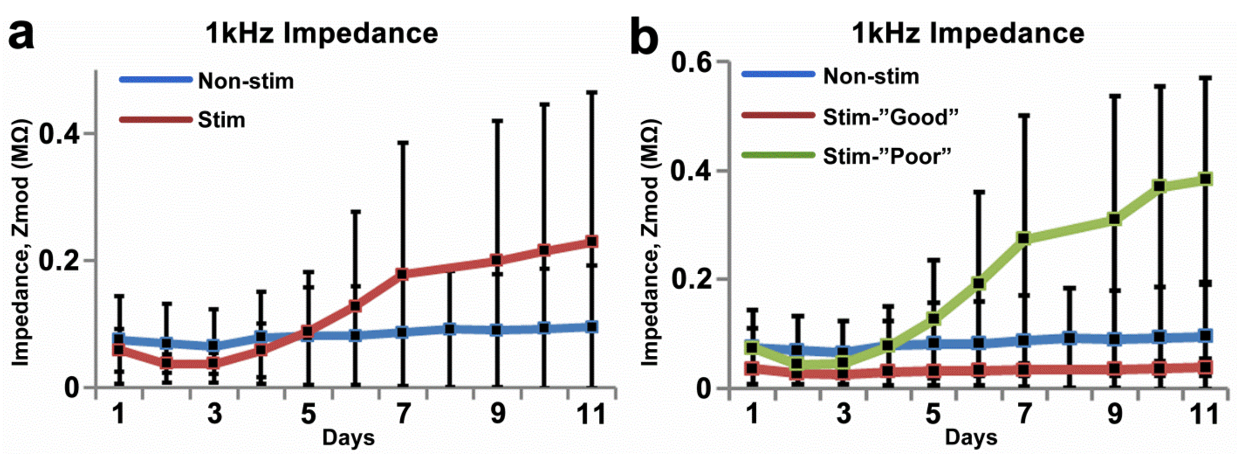

Figure 4.9: Electrode impedances during in vitro measurement. a) Average values of all non-stimulated and stimulated electrodes. b) Average values with stimulated electrodes split into two groups: consistent "good" and inconsistent "poor" impedance performance. Data presented as mean ± SD.

Figure 4.9a and b reveal that a number of the stimulated coated electrodes exhibit a trend of increasing 1 kHz impedance after four days of stimulation, while all of the non-stimulated and the remaining stimulated electrodes exhibited very consistent impedance values over the entire course of the experiment. By day 11, average 1 kHz impedance of the "poorly performing" electrodes approaches the average impedance value of the electrodes before coating (475±162 kΩ), suggesting that the electrochemical benefits of the coating were being steadily extinguished. It should be noted that impedance data from day 8 for the stimulated electrodes were lost due to potentiostat technicalities.

While the chronic 1 kHz impedance performance of the stimulated electrodes in PBS trended in a manner similar to the performance of those implanted *in vivo*, a more in-depth evaluation revealed that the mechanisms behind these performance changes may possess important differences. Figure 4.10 presents a number of representative Nyquist plots from non-stimulated and "poorly" performing stimulated electrodes at different days of PBS immersion. These plots may be compared against those in figure 4.7 above. In particular, figures 4.7f and 4.10f, which represent points of elevated impedance of coated, daily-stimulated electrodes *in vivo* and in PBS *in vitro* respectively reveal very different patterns of frequency response. While the *in vivo* coated stimulated interface is characterized by a high-frequency encapsulation element that increases in magnitude as evident in figures 4.7d-f, the interface in PBS is characterized by a *diminishment* of the high frequency encapsulation element and a gradual straightening and lengthening of the plotted response curve. This behavior suggests that while the impedance increase of the coated stimulated electrodes *in vivo* is driven by the development of some type of resistive encapsulation around the electrode, the impedance increase in PBS is instead a consequence of the gradual loss of electrochemical benefits of the coating as the probe approaches the performance of an uncoated electrode. It is quite possible that this coating loss is also occurring *in vivo* but is being masked from observation by the encapsulation element having a dominating influence on electrode frequency response.

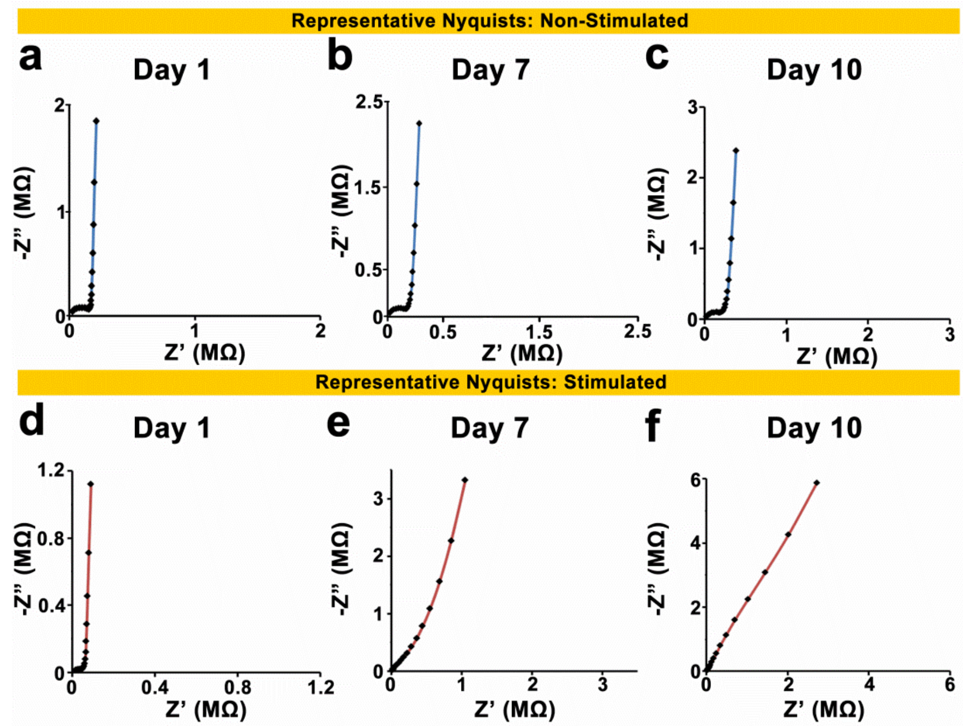

Figure 4.10: Nyquist plots of in vitro data. a-c) Plots collected from a single coated, non-stimulated electrode at three representative days. d-f) Plots collected from a single "poorly performing" coated, daily stimulated electrode on the same days.

To better evaluate the interfacial characteristics of the electrodes at different time points *in vitro*, each set of data was examined using equivalent circuit analysis. Data were fit to the same model used for *in vivo* data fitting, model A (Fig. 4.6a). Average values for key fitted parameters are shown in figure 4.11, including C_{CPE} (the capacity coefficient of the metal interface), and α (the CPE parameter of C_{CPE}, which represents the "idealness" of the capacitor). For the purposes of this fitting procedure, the metal interface charge transfer resistance R_{CT} was assumed to be infinite, while the encapsulation element parameters Q_1, β, R_0, and R_1 were not considered as the encapsulation element was not observed to exist within data recorded from "poorly performing" stimulated electrodes beyond the first few days of stimulation. When evaluating fitted parameters, one of the electrodes from the non-stimulated group was removed from consideration as it exhibited behavior which deviated from the other four by over an order of magnitude. This electrode also exhibited 1 kHz impedance modulus over an order of magnitude under the average of the others, possibly indicating an insulation failure.

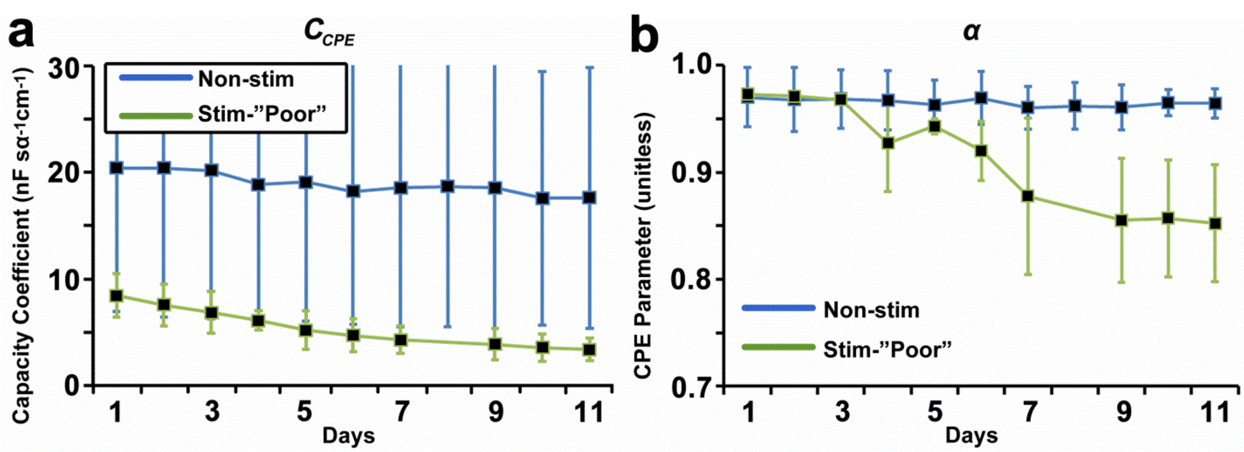

Figure 4.11: Model parameters from fitted in vitro data. a) C_{CPE}, The capacity coefficient of the metal interface. b) β, the CPE parameter of C_{CPE}. Data presented as mean ± SD.

In addition to the rapid disappearance of the encapsulation element, fitted parameters of the "poorly performing" stimulated electrodes reveal that their capacitance exhibited a steadily decreasing trend on average compared to that of the non-stimulated electrodes (though the variances were large, reflecting the range of initial impedances of the electrodes pre-coating). Additionally, the interfacial CPE parameter α of the "poorly performing" electrodes was seen to steadily decrease from a near-ideal value of ~0.98 down to a value of ~0.85, which approaches the average α of the bare pre-coated electrodes, 0.83±0.10. Together, the fitted parameters suggest that the "poorly performing" stimulated electrodes suffered a gradual coating failure, possibly through a delamination mechanism which steadily removed a portion of the impedance benefit of the coating with each passing day of stimulation. As the phenomenon was only observed in three out of the five stimulated electrodes, it may be that the failed electrodes suffered initial coating defects that made them particularly vulnerable to the mechanical stress produced by coating actuation during the CV stimulation process.

4.4 CONCLUSION

We demonstrated the utility of the Bisquert equivalent circuit model in evaluating the core mechanisms behind the impedance changes exhibited by coated and uncoated electrodes *in vitro* and *in vivo*. The fitting results were consistent between probes and animals, and suggest the occurrence of a coating failure between 3 and 5 days post-implantation, due either to partial coating delamination from the metal surface, some loss in coating conductivity, or the development of a dense sheath of reactive tissue that acted to reduce the effective surface area of the coating. *In vitro* trials revealed that the coated electrodes may be vulnerable to some type of coating failure following daily chronic stimulation. However, the nature of this failure appears distinctive between *in vivo* and *in vitro* conditions. Further work will need to be performed to determine more of the true nature of this coating failure, and to evaluate possible solutions.

5.0 CONCLUSION

5.1 SUMMARY OF RESULTS

This dissertation describes the biological consequences of chronic cortical probe implantation, and the emerging technological approaches to countering these consequences with the goal of accelerating progress toward clinical translation. Each study takes a multi-disciplinary approach toward the better understanding of the device/tissue interface, and together combine biochemistry, electrochemistry, materials science, and neural engineering to develop new tools and insights into the problem of long term recording failure. These insights will contribute to the scientific understanding of probe interfacial stability, and inform future engineering approaches and designs.

In chapter 2, we discussed the development of a model for studying the impact and benefit of chondroitinase ABC treatment to intracortical recording electrodes to observe whether the beneficial outcomes observed within spinal injury studies could be translated to indwelling cortical probes. Microinjector design, implantation and injection techniques, and tissue preparation and histology methods were studied and optimized to achieve the most consistent performance and clear perspective of inflammatory response. Chondroitinase ABC microinjection was found to eliminate CSPG around the implant immediately after injection as well as significantly attenuate serum proteins, likely due to release of those serum proteins from ECM entrapment. However, a pilot study performed featuring the implantation of electrode/cannula hybrid implants indicated no clear chronic impedance-changing effects of chondroitinase injection. In summary, the work demonstrated the feasibility of the method and the efficacy of microinjected chondroitinase in eliminating CSPG around an implanted probe. However, the study also revealed a number of challenges to technique translation, including the disturbance of local tissue due to the pressures of obdurator placement and removal, and the abundance of exuded serum protein which can bind to anti-mouse Ig secondary antibodies and complicate imaging. If these challenges are surmounted, this treatment method will serve as a powerful means to better understand the role of CSPGs in chronic neural degeneration and electrode performance loss, and could substantially inform future electrode development.

Chapter 3 discusses the development and evaluation of a novel conducting polymer-based drug release coating composition *in vitro* and *in vivo*, and provides one of the first accounts of the *in vivo* release of a drug dopant from a conducting polymer coating. PEDOT was co-doped with dexamethasone and MWCNTs, which were added to increase the structural resilience, adhesion, and effective surface area of the coating to improve stability and drug release yield. A stimulus protocol was designed with parameters optimized to achieve a degree of release while minimizing tissue and electrode damage, and the protocol was tested *in vitro* to quantify release and observe coating stability. In general, coated and uncoated probes performed similarly with statistically identical recording performance and inflammatory response, with the inflammatory response was observed to be comparable to that evoked by similar probes over similar time periods in other studies. These observations confirmed the safety of the release stimulus, the biocompatibility of the coating, and the ability of the coated probes to record neural activity. With further optimization and chronic testing, this technology could provide a powerful tool for neurophysiological research and next-generation electrode design.

In chapter 4, we discussed the use of equivalent circuit modeling to investigate the physical and physiological basis of the loss of impedance benefit exhibited by the coated probes. A variety of simple interfacial circuit models were adapted and applied to the data, yielding ambiguous results. In the end, we adopted a more sophisticated impedance model described by Bisquert et al.[248] which demonstrated good fitting and consistent parameter dynamics. Fitting indicated that impedance behavior of uncoated probes was dominated by changes to electrode surface characteristics as well as the development of a tissue encapsulation element at later time points, while coated probes exhibited a large surface area benefit at early time points which subsequently diminished, at which point impedance was dominated by a large encapsulating barrier. The model thus suggests that this loss is due to some interference of coating function, either through the obstruction of the coating surface or the delamination of the coating from the metal surface, or some combination of both. From a broader perspective, the study demonstrated the application of sophisticated modeling techniques in extracting more profound insights from impedance data. Despite impedance measurement being a common element of performance evaluation, most studies do not venture beyond simple 1 kHz impedance reporting. However, as this study demonstrates, probes may exhibit identical 1 kHz impedance but substantially different phase features and interfacial characteristics. Circuit modeling provides a more comprehensive method of observing subtle changes to electrode performance.

5.2 FUTURE DIRECTIONS

5.2.1 Chondroitinase ABC

The use of chondroitinase ABC in the treatment of spinal injury has shown substantial promise[125], both through direct application of the enzyme to scar tissue as well as the injection of enzyme within brain stem nuclei and spinal tissue upstream from the lesion. While the removal of CSPGs and their neuro-inhibitory influence from glial encapsulation around an implanted probe may promote neuron survival and sprouting, a number of challenges remain to be overcome for the method to become chronically feasible and practical. Physiologically, glial scar CSPGs likely serve as only a small component of the neuro-inhibitory environment of the tissue inflammatory response, which includes many other factors that would not be affected by the enzyme such as myelin inhibition, oxidative stress, probe micromotion, pro-inflammatory cytokines, and others. As the prevalence of each of these factors would depend largely on the design, implantation method, and inflammatory response of each individual probe, the effectiveness of chondroitinase therapy may not translate universally to all implants. This is particularly relevant in light of the observation that CSPG expression in scar tissue peaks relatively soon after implantation, and diminishes to baseline by the early stages of the chronic inflammatory response[127,141], and well before the 8-16 week time point when chronic neuronal degeneration is generally observed to accelerate[9].

To study the prevalence of CSPG-mediated inhibitory signaling around probes at these later time periods, an important next step would be to evaluate the effects of CSPG digestion at those time points around actual implanted electrodes, which would allow a combination of impedance monitoring, neurophysiological recording, and histological examination. Such work could be carried out using a combined electrode array/cannula hybrid, such as that pictured in figure 5.1. Effective chronic delivery of chondroitinase ABC is another challenge. Current integrated microfluidics systems do not feature the chronic reliability necessary for consistent results, due to crushing and clogging of pores. Large cannulae such as the type used in this work are more mechanically reliable but much more invasive, complicating implantation and long term tissue stability. The adoption of a lentiviral vector for chondroitinase production within target tissue could be an intriguing alternative approach[251].

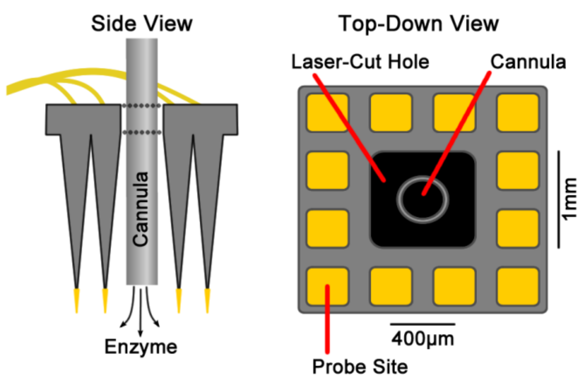

Figure 5.1: Illustration of a proposed cannula/multielectrode array implant.

5.2.2 MWCNT/PEDOT Drug Release Coatings

The concept of the electrically-stimulated drug release coating is advantageous in that it allows for the release of agent at precisely controlled time points without requiring a bulky and unreliable fluidics system. The coatings are easily incorporated onto the recording surfaces of most conventional electrode varieties using simple electrochemistry. This on-demand drug release mechanism could potentially benefit many applications including closed-loop systems designed to release targeted drugs on detecting specific conditions or biomolecules, or the monitoring of neural activity at a very fine temporal resolution after neuromodulatory drug release. While this study demonstrated the safety and short-term biocompatibility of a model release coating, substantial optimization may still be performed in terms of stimulus design, coating morphology and composition, and drug selection. Also, the tissue reactivity and neurotoxicity of the coating at much longer implant durations will need to be assessed.

The dynamic impedance changes observed in coated electrodes during this study and published reports of other similar coatings[203,204,206] are theorized to be the result of either physiological or physical changes to the metal, coating, and tissue interfaces resulting in a large reduction of effective interface surface area. As discussed, these changes could be the result of combinations of several phenomena, such as probe encapsulation by a restrictive barrier of inflammatory tissue and membranous extracellular material, or physical changes to the coating such as swelling or detachment from the metal substrate. To better understand the root of these early *in vivo* impedance changes, *in vitro* experiments may be designed which isolate specific conditions, including electrolyte ionic and protein composition, coating composition and deposition method, release stimulus, and substrate metal preparation. While the impedance change observed in this study did not coincide with a degradation of the charge storage capacity of the electrodes nor a decrease in their recording performance compared to uncoated electrodes, at least within the implantation duration studied, further study should be performed to evaluate its root cause, as an improved understanding of the changes to conducting polymer coating impedance *in vivo* could lead to improved methodology and design in the future.

5.3 CONCLUDING REMARKS

Despite the progress achieved in all aspects of neural prostheses over the past fifty years, widespread clinical and commercial translation has been limited beyond a handful of key devices. Particularly in the field of brain-computer interface, nearly every element has seen profound technical and scientific advancement, from improved neural decoding methods to increasingly sophisticated robotic devices and communication systems. Despite this progress, a key obstacle to clinical translation remains the chronic unreliability of the cortical prostheses that serve as the principal point of contact between tissue and hardware. Unless means are found to effectively and reliably expand the functional lifetime of these devices to decades instead of months and years, their clinical and commercial application will remain untenable. Equally important is that these solutions be practical, mass producible, and not subject to excessive regulatory hurdles. As brain-computer interface technology has the potential to drastically improve the lifestyle, independence, and occupational wellbeing of millions of disabled individuals worldwide, the need for working solutions to this problem remains very relevant.

The past two decades of electrode development and research have revealed much of the mechanisms behind chronic implant failure, and with this understanding has come an evolution in perspective. It is now understood that the tissue-electrode interface is mediated by a profoundly dynamic and multi-faceted interplay between many diverse elements, signaling pathways, inflammatory processes, and biological, chemical, and mechanical stressors that combine to dictate the survival of local neurons. In many ways the interface may be represented as a delicate balance of pro-inflammatory and anti-inflammatory factors, overseen by reactive and regulatory cellular players. In light of this complexity, it is unlikely that a single "magic bullet" approach to electrode development will yield the multiple-decade degree of reliability necessary for widespread clinical translation. Eventual practical solutions will likely require a combination of multi-disciplinary scientific inquiry, advancement in fabrication techniques, materials development, and even regulatory reform.

BIBLIOGRAPHY

1. Schwartz, A. B. Cortical Neural Prosthetics. *Annual Review of Neuroscience* **27,** 487–507 (2004).

2. Friehs, G. M., Zerris, V., Ojakangas, C., Fellows, M. R. & Donoghue, J. P. Brain-Machine and Brain-Computer Interfaces. *Stroke* **35,** 2702–2705 (2004).

3. Lebedev, M. A. & Nicolelis, M. A. L. Brain–machine interfaces: past, present and future. *Trends in Neurosciences* **29,** 536–546 (2006).

4. Hochberg, L. R. *et al.* Neuronal ensemble control of prosthetic devices by a human with tetraplegia. *Nature* **442,** 164–171 (2006).

5. Schwartz, A., Cui, X., Weber, D. & Moran, D. Brain-Controlled Interfaces: Movement Restoration with Neural Prosthetics. *Neuron* **52,** 205–220 (2006).

6. Schultz, A. E. & Kuiken, T. A. Neural Interfaces for Control of Upper Limb Prostheses: The State of the Art and Future Possibilities. *PM&R* **3,** 55–67 (2011).

7. Biran, R., Martin, D. C. & Tresco, P. A. Neuronal cell loss accompanies the brain tissue response to chronically implanted silicon microelectrode arrays. *Experimental Neurology* **195,** 115–126 (2005).

8. McConnell, G. C. *et al.* Implanted neural electrodes cause chronic, local inflammation that is correlated with local neurodegeneration. *Journal of neural engineering* **6,** 056003 (2009).

9. Potter, K. A., Buck, A. C., Self, W. K. & Capadona, J. R. Stab injury and device implantation within the brain results in inversely multiphasic neuroinflammatory and neurodegenerative responses. *Journal of Neural Engineering* **9,** 046020 (2012).

10. Williams, J. Long-term neural recording characteristics of wire microelectrode arrays implanted in cerebral cortex. *Brain Research Protocols* **4,** 303–313 (1999).

11. Liu, X. *et al.* Stability of the interface between neural tissue and chronically implanted intracortical microelectrodes. *IEEE Trans Rehabil Eng* **7,** 315–326 (1999).

12. Kipke, D. R. *et al.* Advanced Neurotechnologies for Chronic Neural Interfaces: New Horizons and Clinical Opportunities. *Journal of Neuroscience* **28,** 11830–11838 (2008).

13. Polikov, V. S., Tresco, P. A. & Reichert, W. M. Response of brain tissue to chronically implanted neural electrodes. *Journal of neuroscience methods* **148,** 1–18 (2005).

14. Suner, S., Fellows, M. R., Vargas-Irwin, C., Nakata, G. K. & Donoghue, J. P. Reliability of Signals From a Chronically Implanted, Silicon-Based Electrode Array in Non-Human Primate Primary Motor Cortex. *IEEE Transactions on Neural Systems and Rehabilitation Engineering* **13,** 524–541 (2005).

15. Vetter, R. J., Williams, J. C., Hetke, J. F., Nunamaker, E. A. & Kipke, D. R. Chronic Neural Recording Using Silicon-Substrate Microelectrode Arrays Implanted in Cerebral Cortex. *IEEE Transactions on Biomedical Engineering* **51,** 896–904 (2004).

16. Nicolelis, M. A. L. *et al.* Chronic, multisite, multielectrode recordings in macaque monkeys. *Proceedings of the National Academy of Sciences* **100,** 11041 (2003).

17. Bartels, J. *et al.* Neurotrophic electrode: method of assembly and implantation into human motor speech cortex. *Journal of neuroscience methods* **174,** 168–176 (2008).

18. Krüger, J., Caruana, F., Dalla Volta, R. & Rizzolatti, G. Seven years of recording from monkey cortex with a chronically implanted multiple microelectrode. *Frontiers in Neuroengineering* (2010). doi:10.3389/fneng.2010.00006

19. Chestek, C. A. *et al.* Long-term stability of neural prosthetic control signals from silicon cortical arrays in rhesus macaque motor cortex. *Journal of Neural Engineering* **8,** 045005 (2011).

20. Simeral, J. D., Kim, S.-P., Black, M. J., Donoghue, J. P. & Hochberg, L. R. Neural control of cursor trajectory and click by a human with tetraplegia 1000 days after implant of an intracortical microelectrode array. *Journal of Neural Engineering* **8,** 025027 (2011).

21. Prasad, A. & Sanchez, J. C. Quantifying long-term microelectrode array functionality using chronic in vivo impedance testing. *Journal of Neural Engineering* **9,** 026028 (2012).

22. Shils, J. L., Mokeem, A. A. & Arle, J. E. in *Monitoring the Nervous System for Anesthesiologists and Other Health Care Professionals* (Koht, A., Sloan, T. B. & Toleikis, J. R.) 95–113 (Springer New York, 2012). at http://www.springerlink.com/index/10.1007/978-1-4614-0308-1_5

23. Wilson, B. S. & Dorman, M. F. Cochlear implants: A remarkable past and a brilliant future. *Hearing Research* **242,** 3–21 (2008).

24. Medtronic DBS Therapy Informational Web Site. at http://www.medtronic.com/patients/parkinsons-disease/therapy/

25. NIH NIDCD Fact Page on Cochlear Implants. at http://www.nidcd.nih.gov/health/hearing/pages/coch.aspx

26. Schalk, G., McFarland, D. J., Hinterberger, T., Birbaumer, N. & Wolpaw, J. R. BCI2000: A General-Purpose Brain-Computer Interface (BCI) System. *IEEE Transactions on Biomedical Engineering* **51,** 1034–1043 (2004).

27. Wolpaw, J. R., McFarland, D. J., Neat, G. W. & Forneris, C. A. An EEG-based brain-computer interface for cursor control. *Electroencephalography and Clinical Neurophysiology* **78,** 252–259 (1991).

28. Wolpaw, J. R., Birbaumer, N., McFarland, D. J., Pfurtscheller, G. & Vaughan, T. M. Brain-computer interfaces for communication and control. *Clin Neurophysiol* **113,** 767–791 (2002).

29. Sheikh, H., McFarland, D. J., Sarnacki, W. A. & Wolpaw, J. R. Electroencephalographic(EEG)-based communication: EEG control versus system performance in humans. *Neuroscience Letters* **345,** 89–92 (2003).

30. McFarland, D. J., Sarnacki, W. A. & Wolpaw, J. R. Electroencephalographic (EEG) control of three-dimensional movement. *Journal of Neural Engineering* **7,** 036007 (2010).

31. Hinterberger, T. *et al.* Voluntary brain regulation and communication with electrocorticogram signals. *Epilepsy & Behavior* **13,** 300–306 (2008).

32. Pei, X., Hill, J. & Schalk, G. Silent Communication: Toward Using Brain Signals. *IEEE Pulse* **3,** 43–46 (2012).

33. Yanagisawa, T. *et al.* Neural decoding using gyral and intrasulcal electrocorticograms. *NeuroImage* **45,** 1099–1106 (2009).

34. Georgopoulos, A. P., Schwartz, A. B. & Kettner, R. E. Neuronal population coding of movement direction. *Science* **233,** 1416–1419 (1986).

35. Velliste, M., Perel, S., Spalding, M. C., Whitford, A. S. & Schwartz, A. B. Cortical control of a prosthetic arm for self-feeding. *Nature* **453,** 1098–1101 (2008).

36. Gibson, C. *One Degree of Separation: Paralysis and Spinal Cord Injury in the United States*. (Christopher & Dana Reeve Foundation, 2009).

37. Liu, X., McCreery, D. B., Bullara, L. A. & Agnew, W. F. Evaluation of the Stability of Intracortical Microelectrode Arrays. *IEEE Transactions on Neural Systems and Rehabilitation Engineering* **14,** 91–100 (2006).

38. Kozai, T. D. *et al.* Ultrasmall implantable composite microelectrodes with bioactive surfaces for chronic neural interfaces. *Nature Materials* **11,** 1065–1073 (2012).

39. Rousche, P. J. & Normann, R. A. Chronic recording capability of the Utah Intracortical Electrode Array in cat sensory cortex. *Journal of neuroscience methods* **82,** 1–15 (1998).

40. Szarowski, D. H. *et al.* Brain responses to micro-machined silicon devices. *Brain Research* **983,** 23–35 (2003).

41. Williams, J. C., Hippensteel, J. A., Dilgen, J., Shain, W. & Kipke, D. R. Complex impedance spectroscopy for monitoring tissue responses to inserted neural implants. *Journal of neural engineering* **4,** 410 (2007).

42. Ward, M. P., Rajdev, P., Ellison, C. & Irazoqui, P. P. Toward a comparison of microelectrodes for acute and chronic recordings. *Brain Research* **1282,** 183–200 (2009).

43. Russell, G. S., Jeffrey Eriksen, K., Poolman, P., Luu, P. & Tucker, D. M. Geodesic photogrammetry for localizing sensor positions in dense-array EEG. *Clinical Neurophysiology* **116,** 1130–1140 (2005).

44. Schalk, G. & Leuthardt, E. C. Brain-Computer Interfaces Using Electrocorticographic Signals. *IEEE Reviews in Biomedical Engineering* **4,** 140–154 (2011).

45. Ludwig, K. A. Neuroprosthetic Devices: Inputs and Outputs. Doctoral Dissertation. University of Michigan (2009).

46. Strumwasser, F. Long-term recording from single neurons in brain of unrestrained mammals. *Science* **127,** 469–470 (1958).

47. Olds, J., Disterhoft, J. F., Segal, M., Kornblith, C. L. & Hirsh, R. Learning centers of rat brain mapped by measuring latencies of conditioned unit responses. *J. Neurophysiol.* **35,** 202–219 (1972).

48. Marg, E. & Adams, J. E. Indwelling multiple micro-electrodes in the brain. *Electroencephalogr Clin Neurophysiol* **23,** 277–280 (1967).

49. Burns, B. D., Stean, J. P. & Webb, A. C. Recording for several days from single cortical neurons in completely unrestrained cats. *Electroencephalogr Clin Neurophysiol* **36,** 314–318 (1974).

50. Salcman, M. & Bak, M. J. A new chronic recording intracortical microelectrode. *Medical & Biological Engineering* **14,** 42–50 (1976).

51. Salcman, M. & Bak, M. J. Design, Fabrication, and In Vivo Behavior of Chronic Recording Intracortical Microelectrodes. *IEEE Transactions on Biomedical Engineering* **BME-20,** 253–260 (1973).

52. Schmidt, E. M., Mcintosh, J. S. & Bak, M. J. Long-term implants of Parylene-C coated microelectrodes. *Medical & Biological Engineering & Computing* **26,** 96–101 (1988).

53. Humphrey, D. R., Schmidt, E. M. & Thompson, W. D. Predicting measures of motor performance from multiple cortical spike trains. *Science* **170,** 758–762 (1970).

54. Schmidt, E. M. Single neuron recording from motor cortex as a possible source of signals for control of external devices. *Annals of Biomedical Engineering* **8,** 339–349 (1980).

55. Wise, K. D., Angell, J. B. & Starr, A. An Integrated-Circuit Approach to Extracellular Microelectrodes. *IEEE Transactions on Biomedical Engineering* **BME-17,** 238–247 (1970).

56. Kewley, D. T. *et al.* Plasma-etched neural probes. *Sensors and Actuators A: Physical* **58,** 27–35 (1997).

57. Bragin, A. *et al.* Multiple site silicon-based probes for chronic recordings in freely moving rats: implantation, recording and histological verification. *Journal of Neuroscience Methods* **98,** 77–82 (2000).

58. Kipke, D. R., Vetter, R. J., Williams, J. C. & Hetke, J. F. Silicon-substrate intracortical microelectrode arrays for long-term recording of neuronal spike activity in cerebral cortex. *IEEE Transactions on Neural Systems and Rehabilitation Engineering* **11,** 151–155 (2003).

59. Jones, K. E., Campbell, P. K. & Normann, R. A. A glass/silicon composite intracortical electrode array. *Annals of Biomedical Engineering* **20,** 423–437 (1992).

60. Nordhausen, C. T., Rousche, P. J. & Normann, R. A. Optimizing recording capabilities of the Utah Intracortical Electrode Array. *Brain Research* **637,** 27–36 (1994).

61. Nordhausen, C. T., Maynard, E. M. & Normann, R. A. Single unit recording capabilities of a 100 microelectrode array. *Brain Research* **726,** 129–140 (1996).

62. Maynard, E. M., Nordhausen, C. T. & Normann, R. A. The Utah intracortical electrode array: A recording structure for potential brain-computer interfaces. *Electroencephalography and clinical Neurophysiology* **102,** 228–239 (1997).

63. Musallam, S., Bak, M. J., Troyk, P. R. & Andersen, R. A. A floating metal microelectrode array for chronic implantation. *Journal of Neuroscience Methods* **160,** 122–127 (2007).

64. Gualtierotti, T. & Bailey, P. A neutral buoyancy micro-electrode for prolonged recording from single nerve units. *Electroencephalogr Clin Neurophysiol* **25,** 77–81 (1968).

65. Merrill, D. R., Bikson, M. & Jefferys, J. G. R. Electrical stimulation of excitable tissue: design of efficacious and safe protocols. *J. Neurosci. Methods* **141,** 171–198 (2005).

66. Bareket-Keren, L. & Hanein, Y. Carbon nanotube-based multi electrode arrays for neuronal interfacing: progress and prospects. *Frontiers in Neural Circuits* **6,** (2013).

67. Daiguji, H. Ion transport in nanofluidic channels. *Chemical Society Reviews* **39,** 901 (2010).

68. Cogan, S. F. Neural Stimulation and Recording Electrodes. *Annual Review of Biomedical Engineering* **10,** 275–309 (2008).

69. Robinson, D. A. The electrical properties of metal microelectrodes. *Proceedings of the IEEE* **56,** 1065–1071 (1968).

70. Grill, W. M., Norman, S. E. & Bellamkonda, R. V. Implanted Neural Interfaces: Biochallenges and Engineered Solutions. *Annual Review of Biomedical Engineering* **11,** 1–24 (2009).

71. Winslow, B. D. & Tresco, P. A. Quantitative analysis of the tissue response to chronically implanted microwire electrodes in rat cortex. *Biomaterials* **31,** 1558–1567 (2010).

72. Kozai, T. D. Y. *et al.* Reduction of neurovascular damage resulting from microelectrode insertion into the cerebral cortex using in vivo two-photon mapping. *Journal of Neural Engineering* **7,** 046011 (2010).

73. Kozai, T. D. Y., Vazquez, A. L., Weaver, C. L., Kim, S.-G. & Cui, X. T. In vivo two-photon microscopy reveals immediate microglial reaction to implantation of microelectrode through extension of processes. *Journal of Neural Engineering* **9,** 066001 (2012).

74. Sanchez, J. C., Alba, N., Nishida, T., Batich, C. & Carney, P. R. Structural Modifications in Chronic Microwire Electrodes for Cortical Neuroprosthetics: A Case Study. *IEEE Transactions on Neural Systems and Rehabilitation Engineering* **14,** 217–221 (2006).

75. Purcell, E. K., Thompson, D. E., Ludwig, K. A. & Kipke, D. R. Flavopiridol reduces the impedance of neural prostheses in vivo without affecting recording quality. *Journal of neuroscience methods* **183,** 149–157 (2009).

76. McConnell, G. C., Butera, R. J. & Bellamkonda, R. V. Bioimpedance modeling to monitor astrocytic response to chronically implanted electrodes. *Journal of Neural Engineering* **6,** 055005 (2009).

77. O'Kusky, J. & Colonnier, M. A laminar analysis of the number of neurons, glia, and synapses in the visual cortex (area 17) of adult macaque monkeys. *The Journal of Comparative Neurology* **210,** 278–290 (1982).

78. Sofroniew, M. V. & Vinters, H. V. Astrocytes: biology and pathology. *Acta Neuropathologica* **119,** 7–35 (2009).

79. Kimelberg, H. K. & Nedergaard, M. Functions of astrocytes and their potential as therapeutic targets. *Neurotherapeutics* **7,** 338–353 (2010).

80. McCaslin, A. F. H., Chen, B. R., Radosevich, A. J., Cauli, B. & Hillman, E. M. C. In vivo 3D morphology of astrocyte–vasculature interactions in the somatosensory cortex: implications for neurovascular coupling. *Journal of Cerebral Blood Flow & Metabolism* **31,** 795–806 (2010).

81. Nimmerjahn, A. Resting Microglial Cells Are Highly Dynamic Surveillants of Brain Parenchyma in Vivo. *Science* **308,** 1314–1318 (2005).

82. Graeber, M. B. & Streit, W. J. Microglia: Immune Network in the CNS. *Brain Pathology* **1,** 2–5 (1990).

83. Graeber, M. B., Li, W. & Rodriguez, M. L. Role of microglia in CNS inflammation. *FEBS Letters* **585,** 3798–3805 (2011).

84. Kettenmann, H., Hanisch, U.-K., Noda, M. & Verkhratsky, A. Physiology of Microglia. *Physiological Reviews* **91,** 461–553 (2011).

85. Hanisch, U.-K. & Kettenmann, H. Microglia: active sensor and versatile effector cells in the normal and pathologic brain. *Nature Neuroscience* **10,** 1387–1394 (2007).

86. Napoli, I. & Neumann, H. Microglial clearance function in health and disease. *Neuroscience* **158,** 1030–1038 (2009).

87. Fitch, M. T. & Silver, J. CNS injury, glial scars, and inflammation: Inhibitory extracellular matrices and regeneration failure. *Experimental Neurology* **209,** 294–301 (2008).

88. Wang, J. Preclinical and clinical research on inflammation after intracerebral hemorrhage. *Progress in Neurobiology* **92,** 463–477 (2010).

89. Henze, D. A. *et al.* Intracellular features predicted by extracellular recordings in the hippocampus in vivo. *J. Neurophysiol.* **84,** 390–400 (2000).

90. Eaton, K. P. & Henriquez, C. S. Confounded spikes generated by synchrony within neural tissue models. *Neurocomputing* **65-66,** 851–857 (2005).

91. Bjornsson, C. S. *et al.* Effects of insertion conditions on tissue strain and vascular damage during neuroprosthetic device insertion. *Journal of Neural Engineering* **3,** 196–207 (2006).

92. Turner, J. *et al.* Cerebral astrocyte response to micromachined silicon implants. *Experimental neurology* **156,** 33–49 (1999).

93. Roitbak, T. & Sykova, E. Diffusion barriers evoked in the rat cortex by reactive astrogliosis. *Glia* **28,** 40–48 (1999).

94. Cui, X., Wiler, J., Dzaman, M., Altschuler, R. A. & Martin, D. C. In vivo studies of polypyrrole/peptide coated neural probes. *Biomaterials* **24,** 777–787 (2003).

95. Kim, Y.-T., Hitchcock, R. W., Bridge, M. J. & Tresco, P. A. Chronic response of adult rat brain tissue to implants anchored to the skull. *Biomaterials* **25,** 2229–2237 (2004).

96. Markwardt, N. T., Stokol, J. & Rennaker II, R. L. Sub-meninges implantation reduces immune response to neural implants. *Journal of Neuroscience Methods* **214,** 119–125 (2013).

97. Edell, D. J., Toi, V. V., McNeil, V. M. & Clark, L. D. Factors influencing the biocompatibility of insertable silicon microshafts in cerebral cortex. *IEEE Transactions on Biomedical Engineering* **39,** 635–643 (1992).

98. Johnson, M. D., Kao, O. E. & Kipke, D. R. Spatiotemporal pH dynamics following insertion of neural microelectrode arrays. *Journal of Neuroscience Methods* **160,** 276–287 (2007).

99. House, P. A., Macdonald, J. D., Tresco, P. A. & Normann, R. A. Acute microelectrode array implantation into human neocortex: preliminary technique and histological considerations. *Neurosurgical Focus* **20,** 1–4 (2006).

100. Khan, A. S. & Michael, A. C. Invasive consequences of using micro-electrodes and microdialysis probes in the brain. *TrAC Trends in Analytical Chemistry* **22,** 503–508 (2003).

101. Groothuis, D. R. *et al.* Changes in blood-brain barrier permeability associated with insertion of brain cannulas and microdialysis probes. *Brain Research* **803,** 218–230 (1998).

102. Yuen, T. G. H. & Agnew, W. F. Histological evaluation of polyesterimide-insulated gold wires in brain. *Biomaterials* **16,** 951–956 (1995).

103. Anderson, J. M., Rodriguez, A. & Chang, D. T. Foreign body reaction to biomaterials. *Seminars in Immunology* **20,** 86–100 (2008).

104. Hu, W.-J. Molecular basis of biomaterial-mediated foreign body reactions. *Blood* **98,** 1231–1238 (2001).

105. Nishimura, N., Schaffer, C. B., Friedman, B., Lyden, P. D. & Kleinfeld, D. Penetrating arterioles are a bottleneck in the perfusion of neocortex. *Proceedings of the National Academy of Sciences* **104,** 365–370 (2007).

106. Chang, E. F., Claus, C. P., Vreman, H. J., Wong, R. J. & Noble-Haeusslein, L. J. Heme regulation in traumatic brain injury: relevance to the adult and developing brain. *Journal of Cerebral Blood Flow; Metabolism* **25,** 1401–1417 (2005).

107. Rosidi, N. L. *et al.* Cortical Microhemorrhages Cause Local Inflammation but Do Not Trigger Widespread Dendrite Degeneration. *PLoS ONE* **6,** e26612 (2011).

108. Raivich, G. *et al.* Neuroglial activation repertoire in the injured brain: graded response, molecular mechanisms and cues to physiological function. *Brain Research Reviews* **30,** 77–105 (1999).

109. Wang, J. & Dore, S. Heme oxygenase-1 exacerbates early brain injury after intracerebral haemorrhage. *Brain* **130,** 1643–1652 (2007).

110. Silva, M. T. Macrophage phagocytosis of neutrophils at inflammatory/infectious foci: a cooperative mechanism in the control of infection and infectious inflammation. *Journal of Leukocyte Biology* **89,** 675–683 (2010).

111. Wang, J. & Tsirka, S. E. Contribution of Extracellular Proteolysis and Microglia to Intracerebral Hemorrhage. *Neurocritical Care* **3,** 077–085 (2005).

112. Purcell, E. K., Seymour, J. P., Yandamuri, S. & Kipke, D. R. In vivo evaluation of a neural stem cell-seeded prosthesis. *Journal of Neural Engineering* **6,** 026005 (2009).

113. Kigerl, K. A. *et al.* Identification of Two Distinct Macrophage Subsets with Divergent Effects Causing either Neurotoxicity or Regeneration in the Injured Mouse Spinal Cord. *Journal of Neuroscience* **29,** 13435–13444 (2009).

114. Kobayashi, K. *et al.* Minocycline selectively inhibits M1 polarization of microglia. *Cell Death and Disease* **4,** e525 (2013).

115. Shefler, I., Salamon, P., Reshef, T., Mor, A. & Mekori, Y. A. T cell-induced mast cell activation: a role for microparticles released from activated T cells. *J. Immunol.* **185,** 4206–4212 (2010).

116. Melzer, N., Meuth, S. G. & Wiendl, H. CD8+ T cells and neuronal damage: direct and collateral mechanisms of cytotoxicity and impaired electrical excitability. *The FASEB Journal* **23,** 3659–3673 (2009).

117. Neumann, H., Medana, I. M., Bauer, J. & Lassmann, H. Cytotoxic T lymphocytes in autoimmune and degenerative CNS diseases. *Trends in neurosciences* **25,** 313–319 (2002).

118. Gee, J. M., Kalil, A., Shea, C. & Becker, K. J. Lymphocytes: Potential Mediators of Postischemic Injury and Neuroprotection. *Stroke* **38,** 783–788 (2007).

119. Melchior, B., Puntambekar, S. & Carson, M. Microglia and the control of autoreactive T cell responses. *Neurochemistry International* **49,** 145–153 (2006).

120. Jones, T. B. *et al.* Pathological CNS autoimmune disease triggered by traumatic spinal cord injury: implications for autoimmune vaccine therapy. *J. Neurosci.* **22,** 2690–2700 (2002).

121. Aloisi, F. Regulation of T-cell responses by CNS antigen-presenting cells: different roles for microglia and astrocytes. *Immunology Today* **21,** 141–147 (2000).

122. Aloisi, F., Serafini, B. & Adorini, L. Glia-T cell dialogue. *Journal of Neuroimmunology* **107,** 111–117 (2000).

123. Neumann, H. Control of glial immune function by neurons. *Glia* **36,** 191–199 (2001).

124. Winslow, B. D., Christensen, M. B., Yang, W.-K., Solzbacher, F. & Tresco, P. A. A comparison of the tissue response to chronically implanted Parylene-C-coated and uncoated planar silicon microelectrode arrays in rat cortex. *Biomaterials* **31,** 9163–9172 (2010).

125. Bradbury, E. J. & Carter, L. M. Manipulating the glial scar: Chondroitinase ABC as a therapy for spinal cord injury. *Brain Research Bulletin* **84,** 306–316 (2011).

126. Harris, N. G., Mironova, Y. A., Hovda, D. A. & Sutton, R. L. Chondroitinase ABC Enhances Pericontusion Axonal Sprouting But Does Not Confer Robust Improvements in Behavioral Recovery. *Journal of Neurotrauma* **27,** 1971–1982 (2010).

127. Zhong, Y. & Bellamkonda, R. V. Dexamethasone-coated neural probes elicit attenuated inflammatory response and neuronal loss compared to uncoated neural probes. *Brain Research* **1148,** 15–27 (2007).

128. Windle, W. F. & Chambers, W. W. Regeneration in the spinal cord of the cat and dog. *The Journal of Comparative Neurology* **93,** 241–257 (1950).

129. Guth, L., Barrett, C. & Donati, E. Histological factors influencing the growth of axons into lesions of the mammalian spinal cord. *Exp. Brain. Res. Suppl.* **13,** 271–282 (1986).

130. Mokarram, N. & Bellamkonda, R. V. Overcoming Endogenous Constraints on Neuronal Regeneration. *IEEE Transactions on Biomedical Engineering* **58,** 1900–1906 (2011).

131. Yiu, G. & He, Z. Glial inhibition of CNS axon regeneration. *Nature Reviews Neuroscience* **7,** 617–627 (2006).

132. McKeon, R. J., Schreiber, R. C., Rudge, J. S. & Silver, J. Reduction of neurite outgrowth in a model of glial scarring following CNS injury is correlated with the expression of inhibitory molecules on reactive astrocytes. *J. Neurosci.* **11,** 3398–3411 (1991).

133. McKeon, R., Hoke, A. & Silver, J. Injury-Induced Proteoglycans Inhibit the Potential for Laminin-Mediated Axon Growth on Astrocytic Scars. *Experimental Neurology* **136,** 32–43 (1995).

134. Bradbury, E. J. *et al.* Chondroitinase ABC promotes functional recovery after spinal cord injury. *Nature* **416,** 636–640 (2002).

135. Tom, V. J. & Houlé, J. D. Intraspinal microinjection of chondroitinase ABC following injury promotes axonal regeneration out of a peripheral nerve graft bridge. *Experimental Neurology* **211,** 315–319 (2008).

136. Lee, H., Leamey, C. A. & Sawatari, A. Rapid Reversal of Chondroitin Sulfate Proteoglycan Associated Staining in Subcompartments of Mouse Neostriatum during the Emergence of Behaviour. *PLoS ONE* **3,** e3020 (2008).

137. Karumbaiah, L. *et al.* Targeted downregulation of N-acetylgalactosamine 4-sulfate 6-O-sulfotransferase significantly mitigates chondroitin sulfate proteoglycan-mediated inhibition. *Glia* **59,** 981–996 (2011).

138. Sugahara, K. & Mikami, T. Chondroitin/dermatan sulfate in the central nervous system. *Current Opinion in Structural Biology* **17,** 536–545 (2007).

139. Deepa, S. S. *et al.* Composition of Perineuronal Net Extracellular Matrix in Rat Brain: A Different Disaccharide Composition For The Net-Associated Proteoglycans. *Journal of Biological Chemistry* **281,** 17789–17800 (2006).

140. Purushothaman, A., Sugahara, K. & Faissner, A. Chondroitin Sulfate 'Wobble Motifs' Modulate Maintenance and Differentiation of Neural Stem Cells and Their Progeny. *Journal of Biological Chemistry* **287,** 2935–2942 (2011).

141. Jones, L. L., Margolis, R. U. & Tuszynski, M. H. The chondroitin sulfate proteoglycans neurocan, brevican, phosphacan, and versican are differentially regulated following spinal cord injury. *Experimental Neurology* **182,** 399–411 (2003).

142. Galtrey, C. M. & Fawcett, J. W. The role of chondroitin sulfate proteoglycans in regeneration and plasticity in the central nervous system. *Brain Research Reviews* **54,** 1–18 (2007).

143. Corvetti, L. & Rossi, F. Degradation of chondroitin sulfate proteoglycans induces sprouting of intact purkinje axons in the cerebellum of the adult rat. *The Journal of neuroscience* **25,** 7150–7158 (2005).

144. Bukalo, O. Modification of extracellular matrix by enzymatic removal of chondroitin sulfate and by lack of tenascin-R differentially affects several forms of synaptic plasticity in the hippocampus. *Neuroscience* **104,** 359–369 (2001).

145. Massey, J. M. Chondroitinase ABC Digestion of the Perineuronal Net Promotes Functional Collateral Sprouting in the Cuneate Nucleus after Cervical Spinal Cord Injury. *Journal of Neuroscience* **26,** 4406–4414 (2006).

146. Galtrey, C. M., Asher, R. A., Nothias, F. & Fawcett, J. W. Promoting plasticity in the spinal cord with chondroitinase improves functional recovery after peripheral nerve repair. *Brain* **130,** 926 (2007).

147. Oohira, A., Matsui, F. & Katoh-Semba, R. Inhibitory effects of brain chondroitin sulfate proteoglycans on neurite outgrowth from PC12D cells. *J. Neurosci.* **11,** 822–827 (1991).

148. Prabhakar, V. *et al*. Biochemical characterization of the chondroitinase ABC I active site. *Biochemical Journal* **390,** 395 (2005).

149. Koprivica, V. EGFR Activation Mediates Inhibition of Axon Regeneration by Myelin and Chondroitin Sulfate Proteoglycans. *Science* **310,** 106–110 (2005).

150. Borisoff, J. F. *et al.* Suppression of Rho-kinase activity promotes axonal growth on inhibitory CNS substrates. *Molecular and Cellular Neuroscience* **22,** 405–416 (2003).

151. Dergham, P. *et al.* Rho signaling pathway targeted to promote spinal cord repair. *J. Neurosci.* **22,** 6570–6577 (2002).

152. Rolls, A. *et al.* A disaccharide derived from chondroitin sulphate proteoglycan promotes central nervous system repair in rats and mice. *European Journal of Neuroscience* **20,** 1973–1983 (2004).

153. Fouad, K. *et al.* Combining Schwann cell bridges and olfactory-ensheathing glia grafts with chondroitinase promotes locomotor recovery after complete transection of the spinal cord. *The Journal of Neuroscience* **25,** 1169–1178 (2005).

154. Lemons, M. L., Howland, D. R. & Anderson, D. K. Chondroitin Sulfate Proteoglycan Immunoreactivity Increases Following Spinal Cord Injury and Transplantation. *Experimental Neurology* **160,** 51–65 (1999).

155. Moon, L. D., Asher, R. A., Rhodes, K. E. & Fawcett, J. W. Regeneration of CNS axons back to their target following treatment of adult rat brain with chondroitinase ABC. *Nat. Neurosci.* **4,** 465–466 (2001).

156. Lin, R., Kwok, J. C. F., Crespo, D. & Fawcett, J. W. Chondroitinase ABC has a long-lasting effect on chondroitin sulphate glycosaminoglycan content in the injured rat brain. *Journal of neurochemistry* **104,** 400–408 (2008).

157. Caggiano, A. O., Zimber, M. P., Ganguly, A., Blight, A. R. & Gruskin, E. A. Chondroitinase ABCI improves locomotion and bladder function following contusion injury of the rat spinal cord. *Journal of neurotrauma* **22,** 226–239 (2005).

158. Iseda, T. *et al.* Single, High-Dose Intraspinal Injection of Chondroitinase Reduces Glycosaminoglycans in Injured Spinal Cord and Promotes Corticospinal Axonal Regrowth after Hemisection but Not Contusion. *Journal of Neurotrauma* **25,** 334–349 (2008).

159. Tester, N. J., Plaas, A. H. & Howland, D. R. Effect of body temperature on chondroitinase ABC's ability to cleave chondroitin sulfate glycosaminoglycans. *Journal of Neuroscience Research* **85,** 1110–1118 (2007).

160. García-Alías, G. *et al.* Therapeutic time window for the application of chondroitinase ABC after spinal cord injury. *Experimental Neurology* **210,** 331–338 (2008).

161. Rohatgi, P., Langhals, N., Kipke, D. R. & Patil, P. G. In Vivo Performance of a Microelectrode Neural Probe with Integrated Drug Delivery. (2009).

162. Du Hoffmann, J., Kim, J. J. & Nicola, S. M. An inexpensive drivable cannulated microelectrode array for simultaneous unit recording and drug infusion in the same brain nucleus of behaving rats. *Journal of Neurophysiology* **106,** 1054–1064 (2011).

163. Glabinski, A. R. *et al.* TNF-α Microinjection Upregulates Chemokines and Chemokine Receptors in the Central Nervous System Without Inducing Leukocyte Infiltration. *Journal of Interferon & Cytokine Research* **23,** 457–466 (2003).

164. Potter, K. A., Simon, J. S., Velagapudi, B. & Capadona, J. R. Reduction of autofluorescence at the microelectrode–cortical tissue interface improves antibody detection. *Journal of Neuroscience Methods* **203,** 96–105 (2012).

165. Chen, M. Y., Lonser, R. R., Morrison, P. F., Governale, L. S. & Oldfield, E. H. Variables affecting convection-enhanced delivery to the striatum: a systematic examination of rate of infusion, cannula size, infusate concentration, and tissue-cannula sealing time. *J. Neurosurg.* **90,** 315–320 (1999).

166. Morrison, P. F., Chen, M. Y., Chadwick, R. S., Lonser, R. R. & Oldfield, E. H. Focal delivery during direct infusion to brain: role of flow rate, catheter diameter, and tissue mechanics. *Am. J. Physiol.* **277,** R1218–1229 (1999).

167. Neeves, K. B., Lo, C. T., Foley, C. P., Saltzman, W. M. & Olbricht, W. L. Fabrication and characterization of microfluidic probes for convection enhanced drug delivery. *Journal of Controlled Release* **111,** 252–262 (2006).

168. Vazquez, L. C. *et al.* Polymer-coated cannulas for the reduction of backflow during intraparenchymal infusions. *Journal of Materials Science: Materials in Medicine* **23,** 2037–2046 (2012).

169. Tresco, P. A. & Gerhardt, G. A. in *Brain-Computer Interfaces* 31–45 (Springer Netherlands, 2008). at http://www.springerlink.com/index/10.1007/978-1-4020-8705-9_3

170. Lempka, S. F. *et al.* Optimization of Microelectrode Design for Cortical Recording Based on Thermal Noise Considerations. in 3361–3364 (IEEE, 2006). doi:10.1109/IEMBS.2006.259432

171. Stice, P., Gilletti, A., Panitch, A. & Muthuswamy, J. Thin microelectrodes reduce GFAP expression in the implant site in rodent somatosensory cortex. *Journal of Neural Engineering* **4,** 42–53 (2007).

172. Seymour, J. P. & Kipke, D. R. Neural probe design for reduced tissue encapsulation in CNS. *Biomaterials* **28,** 3594–3607 (2007).

173. Skousen, J. L. *et al.* in *Progress in Brain Research* **194,** 167–180 (Elsevier, 2011).

174. Rousche, P. J. *et al.* Flexible polyimide-based intracortical electrode arrays with bioactive capability. *Biomedical Engineering, IEEE Transactions on* **48,** 361–371 (2001).

175. Kim, J. *et al.* Flexible thin film electrode arrays for minimally-invasive neurological monitoring. in 5506–5509 (IEEE, 2009). doi:10.1109/IEMBS.2009.5333177

176. Patrick, E., Ordonez, M., Alba, N., Sanchez, J. C. & Nishida, T. Design and Fabrication of a Flexible Substrate Microelectrode Array for Brain Machine Interfaces. in 2966–2969 (IEEE, 2006). doi:10.1109/IEMBS.2006.260581

177. Kozai, T. D. Y. & Kipke, D. R. Insertion shuttle with carboxyl terminated self-assembled monolayer coatings for implanting flexible polymer neural probes in the brain. *Journal of Neuroscience Methods* **184,** 199–205 (2009).

178. He, W. & Bellamkonda, R. V. Nanoscale neuro-integrative coatings for neural implants. *Biomaterials* **26,** 2983–2990 (2005).

179. Williams, J. C., Holecko, M. M., Massia, S. P., Rousche, P. & Kipke, D. R. Multi-site incorporation of bioactive matrices into MEMS-based neural probes. *Journal of Neural Engineering* **2,** L23–L28 (2005).

180. Azemi, E., Stauffer, W. R., Gostock, M. S., Lagenaur, C. F. & Cui, X. T. Surface immobilization of neural adhesion molecule L1 for improving the biocompatibility of chronic neural probes: In vitro characterization. *Acta Biomaterialia* **4,** 1208–1217 (2008).

181. Azemi, E., Lagenaur, C. F. & Cui, X. T. The surface immobilization of the neural adhesion molecule L1 on neural probes and its effect on neuronal density and gliosis at the probe/tissue interface. *Biomaterials* **32,** 681–692 (2011).

182. Pierce, A. L., Sommakia, S., Rickus, J. L. & Otto, K. J. Thin-film silica sol–gel coatings for neural microelectrodes. *Journal of Neuroscience Methods* **180,** 106–110 (2009).

183. Sommakia, S., Rickus, J. L. & Otto, K. J. Effects of adsorbed proteins, an antifouling agent and long-duration DC voltage pulses on the impedance of silicon-based neural microelectrodes. in 7139–7142 (IEEE, 2009). doi:10.1109/IEMBS.2009.5332456

184. Wadhwa, R., Lagenaur, C. F. & Cui, X. T. Electrochemically controlled release of dexamethasone from conducting polymer polypyrrole coated electrode. *Journal of controlled release* **110,** 531–541 (2006).

185. Abidian, M. R., Kim, D.-H. & Martin, D. C. Conducting-Polymer Nanotubes for Controlled Drug Release. *Advanced Materials* **18,** 405–409 (2006).

186. Svirskis, D., Travas-Sejdic, J., Rodgers, A. & Garg, S. Electrochemically controlled drug delivery based on intrinsically conducting polymers. *Journal of Controlled Release* **146,** 6–15 (2010).

187. Thompson, B. C. *et al.* Optimising the incorporation and release of a neurotrophic factor using conducting polypyrrole. *Journal of Controlled Release* **116,** 285–294 (2006).

188. Svirskis, D., Wright, B. E., Travas-Sejdic, J., Rodgers, A. & Garg, S. Development of a Controlled Release System for Risperidone Using Polypyrrole: Mechanistic Studies. *Electroanalysis* **22,** 439–444 (2010).

189. Bidan, G., Lopez, C., Mendes-Viegas, F., Vieil, E. & Gadelle, A. Incorporation of sulphonated cyclodextrins into polypyrrole: an approach for the electro-controlled delivering of neutral drugs. *Biosensors and Bioelectronics* **10,** 219–229 (1995).

190. Thompson, B. C., Moulton, S. E., Richardson, R. T. & Wallace, G. G. Effect of the dopant anion in polypyrrole on nerve growth and release of a neurotrophic protein. *Biomaterials* **32,** 3822–3831 (2011).

191. Cui, X. & Martin, D. C. Electrochemical deposition and characterization of poly (3, 4-ethylenedioxythiophene) on neural microelectrode arrays. *Sensors and Actuators B: Chemical* **89,** 92–102 (2003).

192. Sabouraud, G., Sadki, S. & Brodie, N. The mechanisms of pyrrole electropolymerization. *Chemical Society Reviews* **29,** 283–293 (2000).

193. Thomas, C. A., Zong, K., Schottland, P. & Reynolds, J. R. Poly(3,4-alkylenedioxypyrrole)s as Highly Stable Aqueous-Compatible Conducting Polymers with Biomedical Implications. *Advanced Materials* **12,** 222–225 (2000).

194. Yamato, H., Ohwa, M. & Wernet, W. Stability of polypyrrole and poly(3,4-ethylenedioxythiophene) for biosensor application. *Journal of Electroanalytical Chemistry* **397,** 163–170 (1995).

195. Boretius, T., Schuettler, M. & Stieglitz, T. On the Stability of Poly-Ethylenedioxythiopene as Coating Material for Active Neural Implants. *Artificial Organs* **35,** 245–248 (2011).

196. Morvant, M. C. & Reynolds, J. R. In situ conductivity studies of poly(3,4-ethylenedioxythiophene). *Synthetic Metals* **92,** 57–61 (1998).

197. Yang, J. & Martin, D. C. Microporous conducting polymers on neural microelectrode arrays. *Sensors and Actuators A: Physical* **113,** 204–211 (2004).

198. Yang, J. & Martin, D. C. Microporous conducting polymers on neural microelectrode arrays. *Sensors and Actuators B: Chemical* **101,** 133–142 (2004).

199. Yang, J. *et al.* Ordered surfactant-templated poly(3,4-ethylenedioxythiophene) (PEDOT) conducting polymer on microfabricated neural probes. *Acta Biomaterialia* **1,** 125–136 (2005).

200. Ludwig, K. A., Uram, J. D., Yang, J., Martin, D. C. & Kipke, D. R. Chronic neural recordings using silicon microelectrode arrays electrochemically deposited with a poly(3,4-ethylenedioxythiophene) (PEDOT) film. *Journal of Neural Engineering* **3,** 59–70 (2006).

201. Ludwig, K. A. *et al.* Poly (3, 4-ethylenedioxythiophene)(PEDOT) polymer coatings facilitate smaller neural recording electrodes. *Journal of Neural Engineering* **8,** 014001 (2011).

202. Abidian, M. R. & Martin, D. C. Experimental and theoretical characterization of implantable neural microelectrodes modified with conducting polymer nanotubes. *Biomaterials* **29,** 1273–1283 (2008).

203. Abidian, M. R., Ludwig, K. A., Marzullo, T. C., Martin, D. C. & Kipke, D. R. Interfacing Conducting Polymer Nanotubes with the Central Nervous System: Chronic Neural Recording using Poly(3,4-ethylenedioxythiophene) Nanotubes. *Advanced Materials* **21,** 3764–3770 (2009).

204. Venkatraman, S. *et al.* In Vitro and In Vivo Evaluation of PEDOT Microelectrodes for Neural Stimulation and Recording. *IEEE Transactions on Neural Systems and Rehabilitation Engineering* **19,** 307–316 (2011).

205. Zhou, H., Cheng, X., Rao, L., Li, T. & Duan, Y. Y. Poly(3,4-ethylenedioxythiophene)/multiwall carbon nanotube composite coatings for improving the stability of microelectrodes in neural prostheses applications. *Acta Biomaterialia* (2013). doi:10.1016/j.actbio.2013.01.042

206. Frost, C. M., Wei, B., Baghmanli, Z., Cederna, P. S. & Urbanchek, M. G. PEDOT Electrochemical Polymerization Improves Electrode Fidelity and Sensitivity. *Plastic and Reconstructive Surgery* **129,** 933–942 (2012).

207. Forcelli, P. A. *et al.* Histocompatibility and in vivo signal throughput for PEDOT, PEDOP, P3MT, and polycarbazole electrodes. *Journal of Biomedical Materials Research Part A* **100A,** 3455–3462 (2012).

208. Gerwig, R. *et al.* PEDOT–CNT Composite Microelectrodes for Recording and Electrostimulation Applications: Fabrication, Morphology, and Electrical Properties. *Frontiers in Neuroengineering* **5,** (2012).

209. Cui, X. T. & Zhou, D. D. Poly (3,4-Ethylenedioxythiophene) for Chronic Neural Stimulation. *IEEE Transactions on Neural Systems and Rehabilitation Engineering* **15,** 502–508 (2007).

210. Nyberg, T., Shimada, A. & Torimitsu, K. Ion conducting polymer microelectrodes for interfacing with neural networks. *Journal of Neuroscience Methods* **160,** 16–25 (2007).

211. Wilks, S., Richardson-Burns, S. M., Hendricks, J. L., Martin, D. C. & Otto, K. J. Poly(3,4-ethylene dioxythiophene) (PEDOT) as a micro-neural interface material for electrostimulation. *Frontiers in Neuroengineering* **2,** (2009).

212. Green, R. A., Lovell, N. H., Wallace, G. G. & Poole-Warren, L. A. Conducting polymers for neural interfaces: Challenges in developing an effective long-term implant. *Biomaterials* **29,** 3393–3399 (2008).

213. Thaning, E. M., Asplund, M. L. M., Nyberg, T. A., Inganäs, O. W. & von Holst, H. Stability of poly(3,4-ethylene dioxythiophene) materials intended for implants. *Journal of Biomedical Materials Research Part B: Applied Biomaterials* **9999B,** NA–NA (2010).

214. Luo, X. & Cui, X. T. Electrochemically controlled release based on nanoporous conducting polymers. *Electrochemistry Communications* **11,** 402–404 (2009).

215. Luo, X. & Cui, X. T. Sponge-like nanostructured conducting polymers for electrically controlled drug release. *Electrochemistry Communications* **11,** 1956–1959 (2009).

216. Coleman, J. N. *et al.* Physical Doping of a Conjugated Polymer with Carbon Nanotubes. *Synthetic Metals* **102,** 1174–1175 (1999).

217. Chen, G. Z. *et al.* Carbon Nanotube and Polypyrrole Composites: Coating and Doping. *Advanced Materials* **12,** 522–526 (2000).

218. Luo, X., Matranga, C., Tan, S., Alba, N. & Cui, X. T. Carbon nanotube nanoreservior for controlled release of anti-inflammatory dexamethasone. *Biomaterials* (2011). doi:10.1016/j.biomaterials.2011.05.020

219. Keefer, E. W., Botterman, B. R., Romero, M. I., Rossi, A. F. & Gross, G. W. Carbon nanotube coating improves neuronal recordings. *Nature Nanotechnology* **3,** 434–439 (2008).

220. Lu, Y. *et al.* Electrodeposited polypyrrole/carbon nanotubes composite films electrodes for neural interfaces. *Biomaterials* **31,** 5169–5181 (2010).

221. Spataro, L. *et al.* Dexamethasone treatment reduces astroglia responses to inserted neuroprosthetic devices in rat neocortex. *Experimental neurology* **194,** 289–300 (2005).

222. Jackson, N. & Muthuswamy, J. Artificial dural sealant that allows multiple penetrations of implantable brain probes. *Journal of Neuroscience Methods* **171,** 147–152 (2008).

223. Luo, X., Weaver, C. L., Zhou, D. D., Greenberg, R. & Cui, X. T. Highly stable carbon nanotube doped poly(3,4-ethylenedioxythiophene) for chronic neural stimulation. *Biomaterials* **32,** 5551–5557 (2011).

224. Cui, X., Hetke, J. F., Wiler, J. A., Anderson, D. J. & Martin, D. C. Electrochemical deposition and characterization of conducting polymer polypyrrole/PSS on multichannel neural probes. *Sensors and Actuators A: Physical* **93,** 8–18 (2001).

225. Shain, W. *et al.* Controlling cellular reactive responses around neural prosthetic devices using peripheral and local intervention strategies. *IEEE Transactions on Neural Systems and Rehabilitation Engineering* **11,** 186–188 (2003).

226. Horton, J. C. & Adams, D. L. The cortical column: a structure without a function. *Philosophical Transactions of the Royal Society B: Biological Sciences* **360,** 837–862 (2005).

227. Prusky, G. T., West, P. W. . & Douglas, R. M. Behavioral assessment of visual acuity in mice and rats. *Vision Research* **40,** 2201–2209 (2000).

228. Orazem, M. E. & Tribollet, B. *Electrochemical Impedance Spectroscopy*. (John Wiley and Sons, 2008).

229. Karp, F. B., Bernotski, N. A., Valdes, T. I., Bohringer, K. F. & Ratner, B. D. Foreign Body Response Investigated With an Implanted Biosensor by *In Situ* Electrical Impedance Spectroscopy. *IEEE Sensors Journal* **8,** 104–112 (2008).

230. McAdams, E. T. & Jossinet, J. Tissue impedance: a historical overview. *Physiological Measurement* **16,** A1–A13 (1995).

231. Grill, W. M. & Thomas Mortimer, J. Electrical properties of implant encapsulation tissue. *Annals of Biomedical Engineering* **22,** 23–33 (1994).

232. Johnson, M. D., Otto, K. J. & Kipke, D. R. Repeated Voltage Biasing Improves Unit Recordings by Reducing Resistive Tissue Impedances. *IEEE Transactions on Neural Systems and Rehabilitation Engineering* **13,** 160–165 (2005).

233. Otto, K. J., Johnson, M. D. & Kipke, D. R. Voltage Pulses Change Neural Interface Properties and Improve Unit Recordings With Chronically Implanted Microelectrodes. *IEEE Transactions on Biomedical Engineering* **53,** 333–340 (2006).

234. Mercanzini, A., Colin, P., Bensadoun, J.-C., Bertsch, A. & Renaud, P. In Vivo Electrical Impedance Spectroscopy of Tissue Reaction to Microelectrode Arrays. *IEEE Transactions on Biomedical Engineering* **56,** 1909–1918 (2009).

235. Merrill, D. R. & Tresco, P. A. Impedance Characterization of Microarray Recording Electrodes in Vitro. *IEEE Transactions on Biomedical Engineering* **52,** 1960–1965 (2005).

236. Frampton, J. P., Hynd, M. R., Shuler, M. L. & Shain, W. Effects of Glial Cells on Electrode Impedance Recorded from Neural Prosthetic Devices In Vitro. *Annals of Biomedical Engineering* **38,** 1031–1047 (2010).

237. Geddes, L. A. Historical evolution of circuit models for the electrode-electrolyte interface. *Annals of Biomedical Engineering* **25,** 1–14 (1997).

238. Brug, G. J., van den Eeden, A. L. G., Sluyters-Rehbach, M. & Sluyters, J. H. The analysis of electrode impedances complicated by the presence of a constant phase element. *Journal of Electroanalytical Chemistry and Interfacial Electrochemistry* **176,** 275–295 (1984).

239. Huang, V. M.-W., Vivier, V., Orazem, M. E., Pébère, N. & Tribollet, B. The Apparent Constant-Phase-Element Behavior of a Disk Electrode with Faradaic Reactions. *Journal of The Electrochemical Society* **154,** C99 (2007).

240. Jorcin, J.-B., Orazem, M. E., Pébère, N. & Tribollet, B. CPE analysis by local electrochemical impedance spectroscopy. *Electrochimica Acta* **51,** 1473–1479 (2006).

241. Patrick, E., Orazem, M. E., Sanchez, J. C. & Nishida, T. Corrosion of tungsten microelectrodes used in neural recording applications. *Journal of Neuroscience Methods* **198,** 158–171 (2011).

242. Dymond, A. M. Characteristics of the Metal-Tissue Interface of Stimulation Electrodes. *IEEE Transactions on Biomedical Engineering* **BME-23,** 274–280 (1976).

243. Bobacka, J., Lewenstam, A. & Ivaska, A. Electrochemical impedance spectroscopy of oxidized poly (3, 4-ethylenedioxythiophene) film electrodes in aqueous solutions. *Journal of Electroanalytical Chemistry* **489,** 17–27 (2000).

244. Franks, W., Schenker, I., Schmutz, P. & Hierlemann, A. Impedance Characterization and Modeling of Electrodes for Biomedical Applications. *IEEE Transactions on Biomedical Engineering* **52,** 1295–1302 (2005).

245. Hernández-Ferrer, J., Ansón-Casaos, A. & Martínez, M. T. Electrochemical synthesis and characterization of single-walled carbon nanotubes/polypyrrole films on transparent substrates. *Electrochimica Acta* **64,** 1–9 (2012).

246. Logothetis, N. K., Kayser, C. & Oeltermann, A. In Vivo Measurement of Cortical Impedance Spectrum in Monkeys: Implications for Signal Propagation. *Neuron* **55,** 809–823 (2007).

247. Kocherginsky, N. M. & Wang, Z. The role of ionic conductivity and interface in electrical resistance, ion transport and transmembrane redox reactions through polyaniline membranes. *Synthetic Metals* **156,** 1065–1072 (2006).

248. Bisquert, J. *et al.* Application of a distributed impedance model in the analysis of conducting polymer films. *Electrochemistry Communications* **2,** 601–605 (2000).

249. Bisquert, J. *et al.* Doubling Exponent Models for the Analysis of Porous Film Electrodes by Impedance. Relaxation of TiO2 Nanoporous in Aqueous Solution. *The Journal of Physical Chemistry B* **104,** 2287–2298 (2000).

250. Duan, Y. Y., Clark, G. M. & Cowan, R. S. C. A study of intra-cochlear electrodes and tissue interface by electrochemical impedance methods in vivo. *Biomaterials* **25,** 3813–3828 (2004).

251. Zhao, R.-R. *et al.* Lentiviral vectors express chondroitinase ABC in cortical projections and promote sprouting of injured corticospinal axons. *Journal of Neuroscience Methods* **201,** 228–238 (2011).